Comparing thallium isotopes to paleosalinity and Mo-U isotope paleoredox proxies: A case study of the Upper Devonian Kettle Point Formation, Ontario

by

Natasha Celine Bell

A thesis
presented to the University of Waterloo
in fulfilment of the
thesis requirement for the degree of
Master of Science
in
Earth Sciences

Waterloo, Ontario, Canada, 2023

Author's Declaration

I hereby declare that I am the sole author of this thesis. This is a true copy of the thesis, including any required final revisions, as accepted by my examiners.

I understand that my thesis may be made electronically available to the public.

Abstract

Black shale formations are utilised to reconstruct ancient global ocean redox conditions by analyzing and inferring their geochemical and isotopic compositions. However, the accuracy of these reconstructions can decrease if regional and local influences overprint global signals. This study utilizes the novel thallium (Tl) isotope paleoredox proxy, in conjunction with the well-studied molybdenum (Mo) and uranium (U) isotope redox proxies, to reconstruct the depositional environment of black shales from the Famennian Kettle Point Formation of southern Ontario. The Mo-U isotope ratios of these black shales have been previously inferred by Kendall et al. (2020) to reflect a local redox change from strongly to weakly euxinic conditions within the bottom-waters of the Chatham Sag sub-basin. Paleosalinity proxies were also interpreted by Kendall et al. (2020) as an increase in the Chatham Sag's basin restriction during the Late Famennian.

Authigenic Tl concentrations were obtained through leaching of black shale rock powder using 2 M nitric acid and have a range of 0.72 - 14 µg/g. Units 1 to 3 contained low Tl concentrations (0.72 - 4.3 µg/g) and Unit 4 had relatively high Tl concentrations (3.2 - 14 µg/g). Authigenic Tl isotope ratios were measured against NIST SRM 3158 (0 ε units; statistically identical to NIST SRM 997) and range between –7.1 and –2.0 ± 0.4 ε units (2SD). Authigenic Tl concentrations have a strong negative correlation ($r = –0.79$; $p < 0.001$) with authigenic Tl isotope ratios, which indicate low concentrations contain heavier Tl isotope compositions and high concentrations contain lighter Tl isotope compositions. Thallium isotopes have a very strong negative correlation with U isotope ratios ($r = –0.89$; $p < 0.001$) and a strong positive correlation with Mo isotopes ($r = 0.71$; $p < 0.001$). The positive correlation with Mo isotopes suggests that the Fe-Mn oxyhydroxide particulate shuttle did not influence Tl and Mo isotope expression.

Three distinct groups of samples are apparent in the cross plots of Tl - U and Tl - Mo isotopes. In stratigraphically ascending order, these groups are described as the high Tl - low U - high Mo group of Unit 1 to lower Unit 3 ($\varepsilon^{205}Tl_{mean} = –2.7 \pm 0.4$, 2SD, $n = 13$), the transitional group of upper Unit 3 to lower Unit 4 ($\varepsilon^{205}Tl_{mean} = –4.1 \pm 0.5$, 2SD, $n = 5$), and the low Tl - high U - low Mo group of upper Unit 4 ($\varepsilon^{205}Tl_{mean} = –6.1 \pm 0.6$, 2SD, $n = 17$). Together with the paleosalinity proxies, these groups represent redox and salinity changes within the Chatham Sag throughout the Famennian. Unit 1 to lower Unit 3 experienced increased basin restriction that promoted strong euxinia in the deep basin and the predominance of river inputs as the main source of Tl to the Chatham Sag, which is reflected by average

ε^{205}Tl values comparable to modern rivers. Low trace metal (TM) accumulation and marine paleosalinity during this time suggests that the Chatham Sag was still somewhat connected to the open ocean, and received infrequent inputs of oceanic water to replenish the TM reservoir and maintain marine salinity at the sediment-water interface. During upper Unit 4 deposition, the Chatham Sag's source of TMs shifted to mainly oceanic inputs, indicated by average ε^{205}Tl values comparable to the modern ocean, and suggests a relative decrease in basin restriction. Increased hydrographic connectivity to the open ocean during Unit 4 deposition also increased sedimentary TM accumulation. Additionally, decreased basin restriction and increased freshwater inputs, which is indicated by brackish paleosalinity, diluted aqueous hydrogen sulfide concentrations of the bottom-waters to weakly euxinic conditions. The transitional period between these two environmental regimes occurred during upper Unit 3 to lower Unit 4 deposition, which was coincident with the Late Famennian eustatic transgression of Algeo et al. (2007). The decrease in paleosalinity during the transitional period may have been caused by glacial meltwater outwash from the Acadian highlands to the paleo-south, but an increase in regional precipitation frequency and intensity caused by a shift in regional climate is also considered a potential mechanism. Overall, the application of the Tl isotope paleoredox proxy to the Kettle Point Formation black shales reveals that local and regional environmental factors have a strong influence on Tl isotope expression, and global-scale redox reconstructions using this proxy can be widely inaccurate if smaller scale factors are not considered.

Acknowledgments

This study was funded by the NSERC Discovery Grant, Ontario Early Researcher Award, and the Canada Research Chairs Program (Tier 2 Canada Research Chair in Redox-Sensitive Metal Isotope Geochemistry). Conference expenses for the GAC-MAC Joint Annual Meeting 2023 were partially funded by the Graduate Studies Endowment Fund of the University of Waterloo in the form of the Graduate Student Research Dissemination Award. Access to the Gore of Chatham core was facilitated by the Ontario Oil, Gas, and Salt Resources Library in London, Ontario.

Thanks to my committee members, Dr. John Johnston and Dr. Jenine McCutcheon, for their guidance and constructive critiques. Your perspectives and advice were greatly appreciated during the writing of this thesis. Thanks to Chadlin Ostrander for measuring the primary standards SRM 3158 and 997 and for the insightful conversation at the AGU Fall 2022 Meeting. Thanks to Jen Parks for her mentorship and leadership during my terms as a teaching assistant, and for giving me a space to further develop my teaching and communication skills.

Thanks to my advisor, Dr. Brian Kendall, for his guidance and mentorship, both in the lab and in the classroom. I am grateful for the opportunities to attend several academic conferences and to become more confident and independent in the lab, which are opportunities not all graduate students are able to experience. Thank you for the stories and wisdom of academia that will help guide my future career decisions. Your patience and support throughout the writing of this thesis are immensely appreciated.

Thanks to all my fellow graduate students who made my grad experience more enjoyable, and for all the weird and wonderful conversations and experiences. I wish the best to all of you and your future endeavours. Thanks to my family for supporting me throughout my studies, and for nurturing my love for nature with family trips of hiking and camping. Thank you to my work-from-home officemates, Jeremy (human), Fresca and Ray (budgies), for the encouragement and support, especially when my doubts were louder than my self-assurance.

Table of Contents

List of Figures

List of Tables

List of Abbreviations

auth	authigenic
Al	aluminum
aq	aqueous
B	boron
Ba	barium
BCR-2	Columbia River Basalt
C	carbon
cm	centimetre
EF(s)	enrichment factor(s)
Fe	iron
Ga	gallium
GSP-2	Silver Plume Granodiorite
GoC	Gore of Chatham
HF	hydrofluoric acid
H_2S	hydrogen sulfide
ICZ(s)	intercalated zone(s)
K	potassium
M	molarity
m	meter
Mg	magnesium
mL	milliliter
mm	millimeter
Mn	manganese
Mo	molybdenum
Mya	million years ago
µg/g	micrograms per gram
µM	micromolarity
Na	sodium
NAS	North American Seaway
NIST	National Institute of Standards and Technology

ng	nanograms
ng/g	nanograms per gram
OM	organic matter
OMZ(s)	oxygen minimum zone(s)
P	phosphorous
Pb	lead
ppb	parts per billion
ppm	parts per million
Re	rhenium
S	sulfur
Sr	strontium
SRM	Standard Reference Material
Tl	thallium
TM(s)	trace metal(s)
TOC	total organic carbon
TS	total sulfur
U	uranium
UCC	upper continental crust
USGS	United States Geological Survey
V	vanadium
wt.%	weight percent
XRD	X-ray diffraction
2SD	2 standard deviations

1.0.0 Introduction

The geochemistry of black shales can record the marine conditions at the time of their deposition, prior to lithification. Modern epeiric sea basins and coastlines are used as analogues of ancient basins where black shales accumulated (Morford et al., 2005; Morford, Martin, François, et al., 2009). Trace metal (TM) concentrations and isotope compositions of modern basins' water and sediments are utilised as proxies of ancient marine conditions such as water redox (Bennett & Canfield, 2020) and salinity (Wei & Algeo, 2020). Trace elements molybdenum (Mo), uranium (U), and thallium (Tl) are used to evaluate paleoredox because they are geochemically and isotopically sensitive to changes in dissolved oxygen and sulfide contents (Hlohowskyj et al., 2021; Lau et al., 2019; Owens, 2019). Some interpretations of isotope data attempt to infer conditions on a global scale, however, the global redox signature can be overprinted by local and regional depositional factors, such as bottom-water redox changes (Algeo & Tribovillard, 2009), variable basin restriction to the open ocean (Algeo et al., 2007), and the presence of a Fe-Mn particulate shuttle within the water column that enhances delivery of some trace metals to sediments (Scholz et al., 2013). In early studies, each element was interpreted individually, which created inconsistencies and ambiguity due to the variability of each elements' sedimentary enrichment mechanisms (Herrmann et al., 2012). More recently, the Mo and U isotope systems are analysed together and provide better interpretations of ancient global redox, although this dual proxy system can only provide partial information, such as the presence and extent of sulfidic and anoxic (i.e. euxinic) waters (Brüske et al., 2020; Noordmann et al., 2015). The novel Tl isotope redox proxy is sensitive to well-oxygenated waters, and in combination with Mo and U, the extent of both oxic and reducing conditions at a global scale can be deciphered. The oceanic residence time of Tl is also shorter than Mo and U (Owens et al., 2017; Miller et al., 2011; Dunk et al., 2002), which means Tl captures redox changes at a finer temporal resolution. In addition, Tl isotopes are expected to be sensitive to local depositional processes, like the Fe-Mn shuttle (Ostrander et al., 2020).

While many studies have utilized sedimentary Tl isotopes to interpret ancient global ocean redox conditions (e.g. Bowman et al., 2019; Newby et al., 2021; Ostrander et al., 2017, 2019; Them et al., 2018), very few studies (e.g. Fan et al., 2020 and Z. Li et al., 2021) have applied the Tl - Mo - U proxy system in tandem. Therefore, utilizing the novel triple isotope paleoredox proxies enables a holistic interpretation of the global and local redox controls on the preservation of isotopic signatures in black shales. Using the Upper Devonian Kettle Point Formation of southern Ontario as a case study, the objectives of this study are to:

1) Determine if the local Fe-Mn particulate shuttle influenced Tl abundance and isotope compositions
2) Determine local and/or regional influences on Tl abundances and isotope compositions, such as sea-level fluctuations and changes to the extent of basin restriction
3) Synthesize previous interpretations for the Mo-U isotope proxies and paleosalinity proxies with Tl isotope interpretations to constrain paleoenvironmental conditions.

2.0.0 Geological Background

2.1.0 Tectonic Setting of the Kettle Point Formation

The Kettle Point Formation was one of many black shale formations deposited into the broad epicontinental North American Seaway (NAS) that covered the paleo-southeastern region of the Laurentian Craton (Figure 1a). During the Famennian, the Laurentian Craton was located within the equatorial region, and surrounded by the Rheic Ocean to the paleo-south and the Panthalassic Ocean to the paleo-west (Scotese, 2021). The NAS, sometimes referred to as the Kaskaskia Sea in reference to the Kaskasia I-II stratigraphic sequences of Sloss (1963), was a series of intracratonic and foreland basins that were flooded and separated by shallow, submerged sills and topographic highs, such as structural arches and domes (Algeo et al., 2007). The Kettle Point Formation was deposited into the Chatham Sag sub-basin, a structural yoke between the larger foreland Appalachian Basin to the southeast and the smaller, intracratonic Michigan Basin to the northwest (Béland-Otis, 2013; Ettensohn et al., 2019) (Figure 1b). The topographic highs of the Findlay and Algonquin Arches surrounded the southwestern and northeastern margins of Chatham Sag, respectively. Deposition occurred throughout the Famennian,

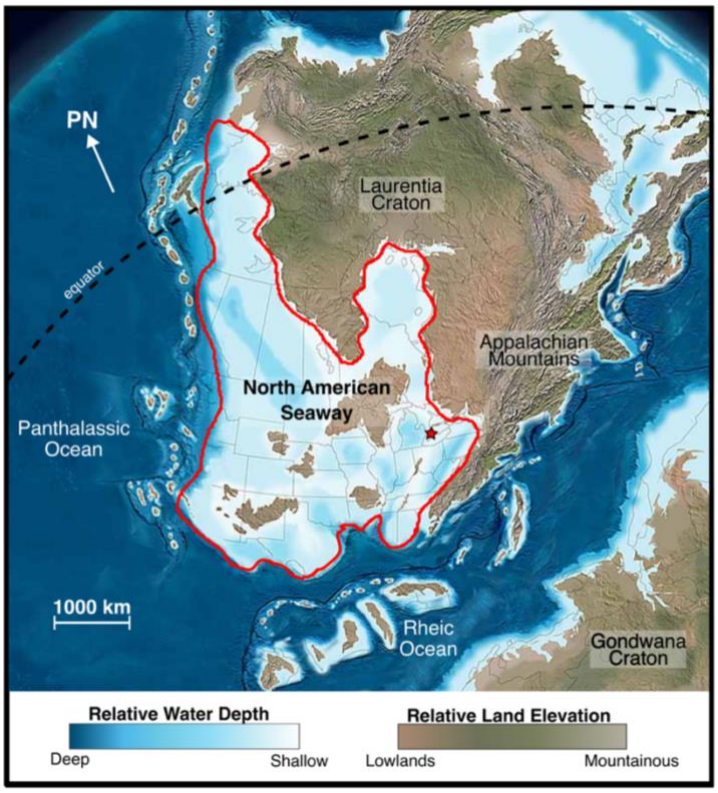

Figure 1a Paleogeography of the Laurentia Craton during the Late Devonian, around 360 Ma. North American Seaway (NAS) outlined in red. Red star = Chatham Sag; PN = paleo-north. Base map from Blakey (2013).

and was concomitant with the accretion of the Carolina Terrane to the eastern margin of the Laurentian Craton during the Acadian Orogeny (Ettensohn et al., 2019).

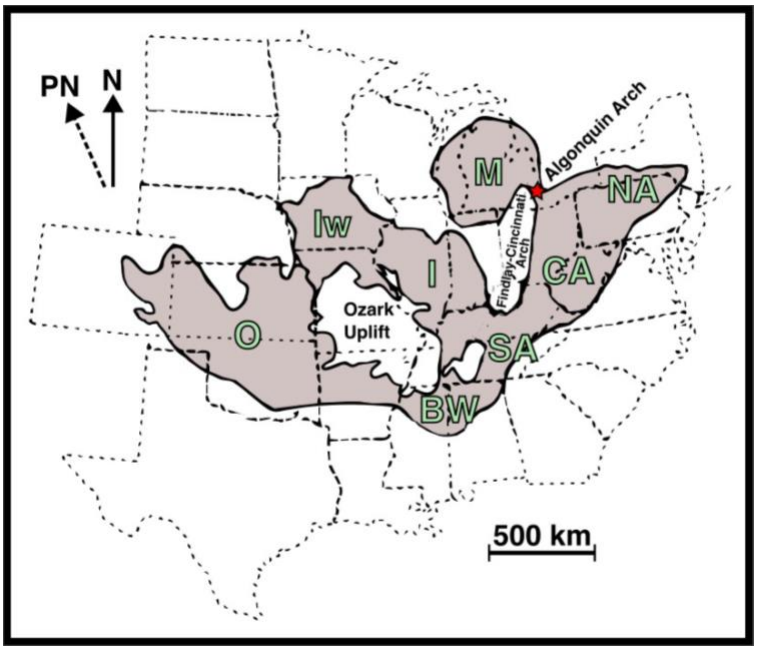

Figure 1b Modern locations of eastern NAS paleobasins. Red star = Chatham Sag; BW = Black Warrior Basin; CA = Central Appalachian Basin; I = Illinois Basin; Iw = Iowa Basin; M = Michigan Basin; N = north; NA = Northern Appalachian Basin; O = Oklahoma Basin; PN = paleo-north; SA = Southern Appalachian Basin. Modified from Over et al. (2002).

2.2.0 Regional Famennian Formations

Black shale formations that are stratigraphically equivalent to the Kettle Point Formation can be found across United States and Canada, and their appeal as oil and gas plays have led to numerous studies on their geochemical composition and depositional environment. Figure 2 shows the regional names of neighbouring Famennian marine and terrestrial formations and their corresponding basins that will be mentioned in this study. Previous research may show inconsistent nomenclature, such as the interchangeable use of "New Albany Shale" and "Ohio Shale" in Rimmer et al. (2004). Some formations are not spatially bound to a single basin, such as the Chattanooga Formation, which is found in the southern regions of both the Appalachian and Illinois Basins, in the northern regions of the Oklahoma Basin, and throughout the Iowa Basin (Figure 1b) (Over, 2002).

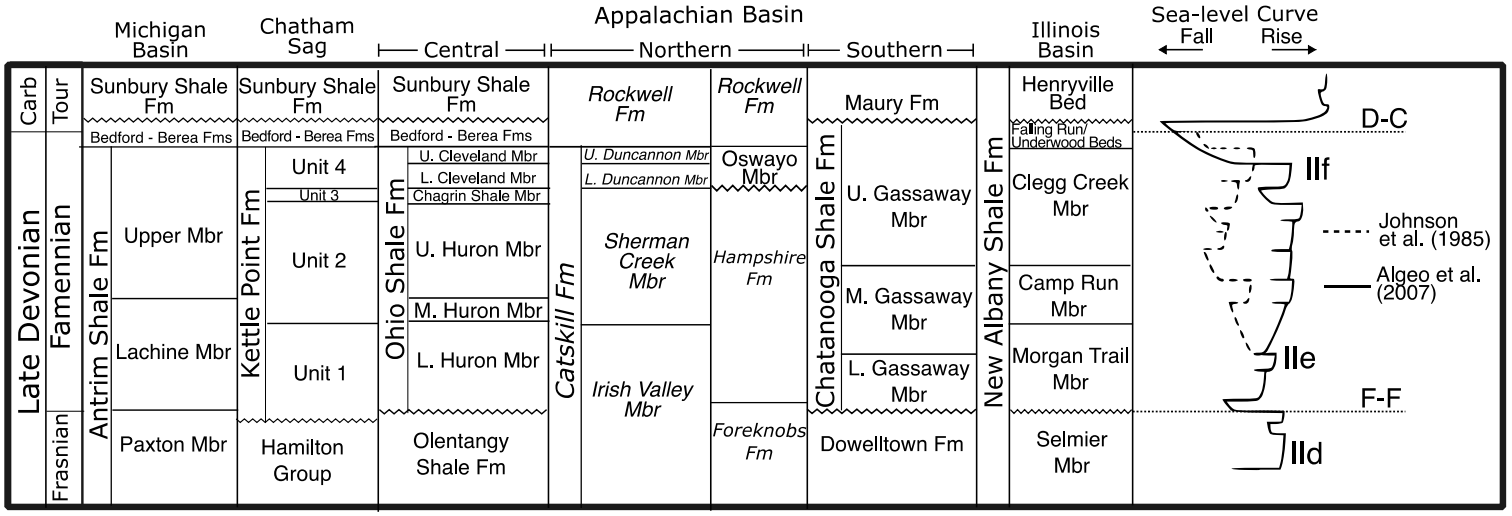

Figure 2 Simplified schematic of Kettle Point Formation units and coeval facies of the eastern NAS. Marine facies in normal typeface and terrestrial facies in italics. Y-axes represents time of deposition relative to sea-level curve. F-F = Frasnian-Famennian boundary; D-C = Devonian-Carboniferous boundary. Data compiled from Algeo et al. (2007), Brezinski et al. (2009), Kendall et al. (2020), Mansour et al. (2022), and Song et al. (2021).

2.2.1 Regional Climate

The Famennian Stage was a period of climate transition across eastern Laurentia. The geologic record shows a shift from a hot and dry paleoclimate during the Early Famennian to a cold and wet climate at the Devonian-Carboniferous (D-C) boundary. For example, the $\delta^{15}N$ and $\delta^{13}C$ values of the Lower Huron and Cleveland Shale Members (Ohio Shale Formation) suggest they were deposited in a greenhouse and an icehouse climate, respectively, and were caused by differences in microbial fixation and burial of atmospheric nitrogen (N) and carbon (C) during the two climate regimes (Tuite et al., 2019). Furthermore, conodont apatite $\delta^{18}O$ values were used to calculate global surface water temperatures, and recorded 30-32°C at the beginning of the Famennian and then a decrease to 25-27°C by the end of the stage (Joachimski et al., 2009).

2.2.2 Regional Glaciation

The D-C glaciation of Gondwanaland is evident throughout South America and northern Africa, and the extent of ice coverage has been more recently discovered in North America (Isaacson et al., 2008). Glacial events were recorded in both terrestrial (Brezinski et al., 2008, 2010) and marine facies (Ettensohn, Seckinger, et al., 2020) of the eastern region of the NAS at the beginning of the Late Famennian. Evidence of tidewater glaciers includes a 400 km by 40 km discontinuous belt of diamictite

sequence interpreted as glacially deposited tillites in the central Appalachian Basin (Brezinski et al., 2008), as well as glaciotectonic shear fabrics and Nye channels interpreted as subglacial environments in the strata below the diamictite facies (Brezinski et al., 2010). The palynology of the diamictite belt correlates its deposition with the upper Cleveland Member (Ohio Shale) and the Oswayo Member (Hampshire) black shales (Ettensohn, Seckinger, et al., 2020). The coeval deposition of large granodiorite boulders in the upper Cleveland Member ~500 km to the west of the diamictite belt are interpreted as ice-rafted debris that calved from the terminus of tidewater glaciers and deposited into the distal marine setting (Ettensohn et al., 2007; Ettensohn, Clayton, et al., 2020). Plutonic zircons from the diamictite indicate provenance of Ordovician-aged uplifted plutons near the foothills of Acadian highlands (Ettensohn, Clayton, et al., 2020 and references therein). The granodiorite of the erratic boulders are also Early to Mid-Ordovician in age and thought to have originated from peri-Laurentian meta-plutonic suites in the central and southern highlands (Ettensohn, Clayton, et al., 2020 and references therein).

2.2.3 Regional Sea-level

The eustatic sea-level curve by Johnson et al. (1985) is commonly used to describe 3rd order transgressive-regressive (T-R) cycles across the eastern Laurentian craton throughout the Devonian. It was constructed using temporal and spatial variations in sedimentary packages and conodont zones. The Kettle Point Formation encompasses the IIe and IIf T-R cycles of the Famennian Stage (Figure 2) (Johnson et al., 1985). The Early to Mid-Famennian IIe T-R cycle is described as an overall regressive episode that was punctuated by two transgressive events, and the Late Famennian IIf cycle as a major transgression leading up to the D-C boundary (Johnson et al., 1985).

More recently, black shale geochemical studies by Algeo et al. (2007) utilised trace element and total organic carbon (TOC) contents of several black shale formations to refine sea-level fluctuations throughout the NAS, and have made modifications to the Famennian sea-level curve of Johnson et al. (1985). The Early to Mid-Famennian is inferred as an overall transgression with minor regressive events (Algeo et al., 2007). A transgressive event occurred at the beginning of the Late Famennian, and then a major regression occurred at the end of the Famennian and across the D-C boundary that is concurrent with the onset of the D-C glaciations (Algeo et al., 2007). Ettensohn, Seckinger, et al. (2020) suggest that the Late Famennian transgression resulted from a combination of global eustatic rise, glacial

loading from the extensive Gondwanaland glaciation, and deformational loading by the Carolina Terrane accretion that resulted in regional subsidence.

2.3.0 Lithology of the Kettle Point Formation

The Kettle Point Formation was divided into four units based on differences in lithofacies. Units 1 and 3 consist of alternating beds of interlaminated black shales (Figure 3a) and bioturbated green-grey mudstones, as well as rare interbeds of red mudstones in select areas within Unit 3 (Bingham-Koslowski et al., 2016). Some black shale interlaminations in these two units consist of whiter and often graded, clay to silt-sized grains of quartz (SiO_2) that alternate with darker clay lamina, and were previously interpreted as high-energy storm deposits or turbidites (Armstrong, 1987; Bingham-Koslowski et al., 2016). Units 2 and 4 are dominated by black shales that appear more massive or non-interlaminated, because of the absence of quartz lamina, the predominance of clay-sized grains, and thinner lamina than the black shales in Units 1 and 3 (Figure 3b) (Bingham-Koslowski et al., 2016). Both black shales lithologies contain pyrite, from framboids (<0.005-0.2 mm) to cm-scale nodules and lenses (Bingham-Koslowski et al., 2016; Russell, 1993). Overall, the Kettle Point Formation is predominantly composed of quartz and illite, and there is no significant mineralogical difference between the black shales and green-grey mudstones, with the exceptions of: 1) ≥ 10% lower quartz contents in the green-grey mudstones and 2) the pyrite and high organic carbon contents in the black shale facies (Delitala, 1984).

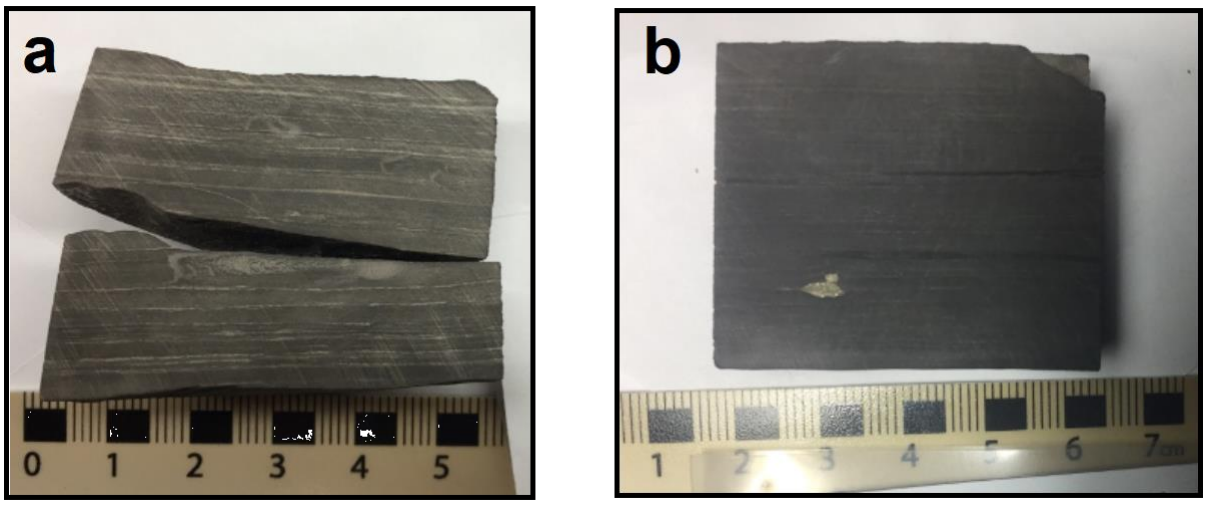

Figure 3 Photos of (a) interlaminated and (b) non-interlaminated black shales. Scale in cm.

2.3.1 Sea-level Influence on Regional Lithostratigraphy

Bingham-Koslowski et al. (2016) propose the four units can be grouped into two separate cycles of sea-level change and suggest Units 1-2 as one cycle and Units 3-4 as another. The interbedding of black shales and green-grey mudstones lithofacies in Unit 1 are inferred as short-term variations in regional climate (Bingham-Koslowski et al., 2016). The black shales represent periods of wetter conditions and increased freshwater input that stratified on top of the denser seawater, which caused stagnation and anoxia within the basin's deep waters (Bingham-Koslowski et al., 2016). The green-grey mudstones represent drier conditions and increased evaporation rates, which caused increased thermohaline circulation by the sinking of saltier and denser surface waters (Bingham-Koslowski et al., 2016 and references therein). Unit 2's non-interlaminated black shales are interpreted as a regional sea-level transgression that submerged the surrounding terrestrial landscape and created a euxinic setting for the deeper waters of the Chatham Sag (Bingham-Koslowski et al., 2016; Kendall et al., 2020). The relative sea-level rise allowed for deep-water basin restriction provided by the Findlay-Algonquin arch system, with some watermass exchange between the Chatham Sag and Appalachian and Michigan Basins (Figure 4a) (Bingham-Koslowski et al., 2016; Kendall et al., 2020). Low energy, upwelling

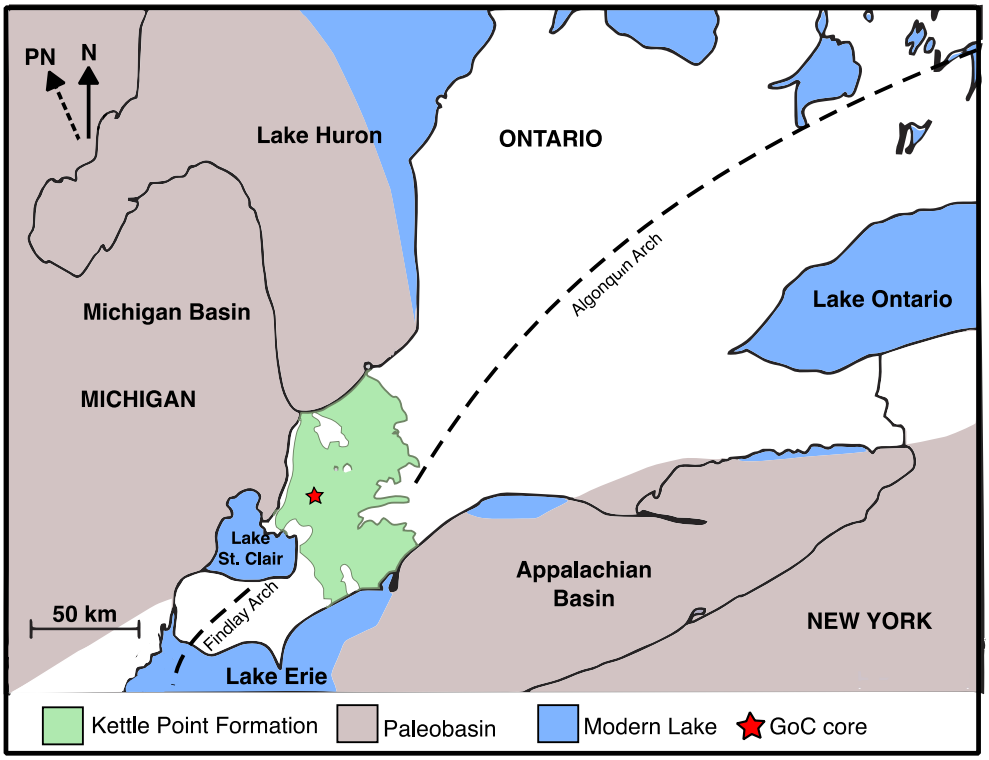

Figure 4a Map of the Chatham Sag sub-basin. Location of study core marked by red star. PN = paleonorth; N = north. Modified from Bingham-Koslowski et al. (2016).

events from surrounding basins provided the Chatham Sag with nutrients required for efficient microbial productivity including sulfate reduction that likely drove deep-water sulfide production and pyrite formation (Bingham-Koslowski et al., 2016; Kendall et al., 2020). Bingham-Koslowski et al. (2016) interpreted the second cycle, consisting of Units 3 and 4, to be similar in relative sea-level changes and depositional environments as Units 1 and 2, respectively. Unit 3 reflects a relative drop in the basin's sea-level to create a shallower water column that, like Unit 1, experienced short-term fluctuations between high-stand stagnation (i.e. black shales) and thermohaline circulation of oxygenated surface waters (i.e. green-grey mudstones) (Bingham-Koslowski et al., 2016). The occurrence of thin, red mudstone facies that alternate with green-grey mudstones may reflect the shallowest, most oxygen-rich conditions within the Chatham Sag (Bingham-Koslowski et al., 2016). Unit 4 indicates an anoxic, deep-basin environment caused by transgressive eustatic conditions, however, Bingham-Koslowski et al. (2016) note that sea-level at this time may not have been as high as during Unit 2 deposition because terrestrial fossils are absent in Unit 4 but present in Unit 2.

2.3.2 Regional Tectonic Influence on Lithostratigraphy

Although the paleoenvironmental interpretations focus on sea-level fluctuations as the main mechanism for lithostratigraphic changes, Bingham-Koslowski (2015) mentions that tectonic activity may have influenced the regional differences observed in the Kettle Point Formation. Increasing trends in Unit 3's overall thickness and the thickness of its green-grey mudstone beds are observed across the formation, from 0.5 m thick beds in the north to 20 m thick in the southwest (Bingham-Koslowski, 2015). Additionally, the presence of red mudstones in Unit 3 are only found in two cores, KP-17 and KP-18, along the southwestern margin (Figure 4b) (Bingham-Koslowski, 2015). The increased thickness of green-grey facies were thought to be deposited into a persistently shallow and oxygenated environment, which was a result of decreased accommodation space along the southwestern margin of the Chatham Sag (Bingham-Koslowski, 2015). While a decrease in sea-level could explain the shallowing, Bingham-Koslowski (2015) also proposes a localized uplift occurred at the end of Unit 2 that was associated with the Acadian Orogeny. The structural uplift may have been a response to far-field flexure to the orogeny in the east that caused either the Findlay Arch to move further into the Chatham Sag, or a structural forebulge to form between the Findlay-Algonquin arches (Bingham-Koslowski, 2015). Another hypothesis for a local uplift was a response to increased sedimentation along the eastern Laurentian margin attributed to the orogeny, which could cause upward flexure of the

craton interior and possibly within the Chatham Sag (Bingham-Koslowski, 2015). An elevated platform around the Findlay Arch that extended northeast into the Chatham Sag is also proposed as a shallowing mechanism (Bingham-Koslowski, 2015). The lack of geological wells south-west of the study area, as well as a lack of lithological data of the coeval Antrim Formation to the west, makes the identification and extent of the localized uplift difficult to determine (Bingham-Koslowski, 2015).

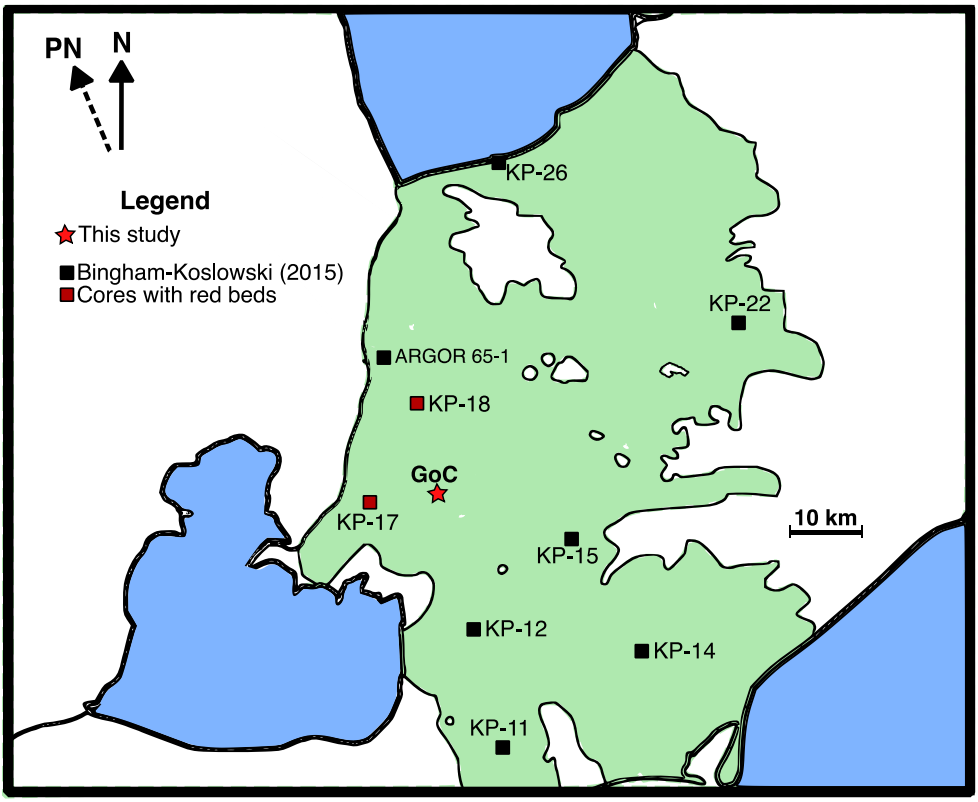

Figure 4b Location of Gore of Chatham (GoC) core and other Kettle Point (KP) cores. PN = paloenorth; N = north. Modified from Bingham-Koslowski et al. (2016).

2.3.3 Local Lithostratigraphy of the Gore of Chatham Core

The core in this study, the Gore of Chatham (GoC) core, is found close to the southwestern margin of the Chatham Sag. A log of the GoC core was done by Wang (2016) and confirmed its lithostratigraphy was similar to cores within the middle of the sub-basin, as described by Bingham-Koslowski et al. (2016). The GoC core is 111.1 m in thickness and the Frasnian-Famennian boundary is located at depth 134.4 m at the bottom of Unit 1 (Figure 5) (Kendall et al., 2020; J. Wang, 2016). Unit 1 is ~17 m thick, and Units 2 and 4 measure 29 m and ~38 m in thickness, respectively (J. Wang, 2016). Unit 3 is 27 m in thickness and lacks the red mudstone facies found in KP-17 and -18. However, the overall thickness of the unit and individual green-grey beds are similar to Unit 3 in the other

southwestern cores. One green-grey bed in the middle of Unit 3, at depths between 77 and 83 m, measures 7 m in thickness (J. Wang, 2016). This is the only thick green-grey bed in Unit 3, whereas the other green-grey facies in the unit measure ≤ 1 m (J. Wang, 2016).

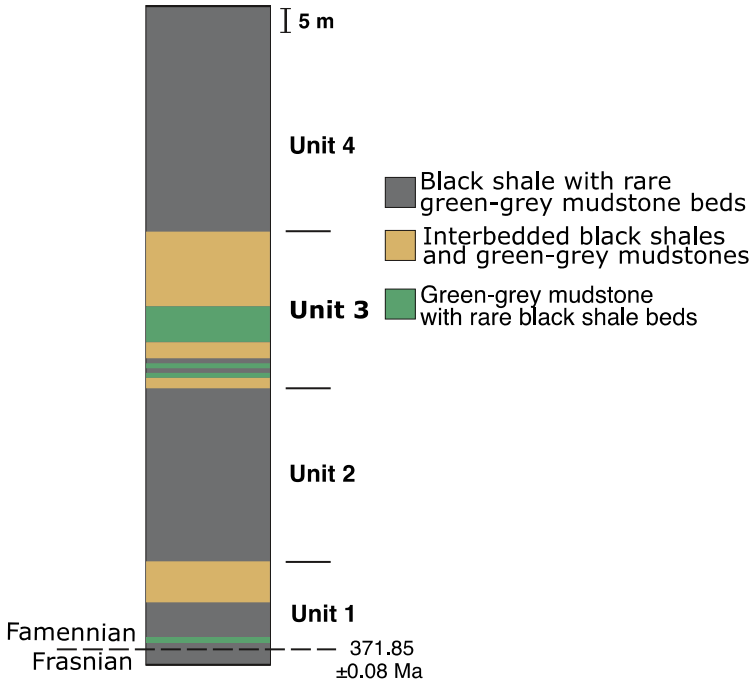

Figure 5 Diagram of GoC core. Age of Frasnian-Famennian boundary from Percival et al. (2018). Modified from Kendall et al. (2020).

3.0.0 Geochemical Background

Elemental paleoproxies thallium (Tl), molybdenum (Mo), and uranium (U) are conservative elements in oxygenated marine waters, and are elementally and isotopically homogenous in the modern ocean due to their longer oceanic residence times (Tl ~20 kyr, Owens et al., 2017; Mo ~440 kyr, Miller et al., 2011; U ~450 kyr, Dunk et al., 2002) compared to the ocean's turnover rate (~2.6 kyr; Henshaw et al., 2000). Understanding their geochemical behaviours in various conditions is necessary to interpret past marine environments from black shales. Modern marine basins and coastlines are used as analogues for ancient marine settings to observe elemental and isotopic behaviours in water columns, at sediment-water boundaries, and in sediment pore waters.

3.1.0 Thallium

3.1.1 Geological Occurrence and Mass Balance

Most geological materials exhibit various abundances of Tl, however, they display minor variation in ε^{205}Tl values, which are calculated as (Nielsen et al., 2017 and references therein; Nielsen & Rehkämper, 2011; Owens et al., 2017):

$$\varepsilon^{205}\text{Tl (ε-units)} = 10^4 \times ({}^{205}\text{Tl}/{}^{203}\text{Tl}_{\text{sample}} - {}^{205}\text{Tl}/{}^{203}\text{Tl}_{\text{NIST SRM 997}}) \div ({}^{205}\text{Tl}/{}^{203}\text{Tl}_{\text{NIST SRM 997}})$$

Sources of Tl to the modern ocean comprise of 23% river water (ε^{205}Tl = –2.5), 35% volcanic gases and 2% aerosols (ε^{205}Tl = –2), 17% hydrothermal fluids (ε^{205}Tl = –2) and 17% Tl dissolution from sediment pore waters (ε^{205}Tl = 0) (Owens, 2019 and references therein). Modern seawater ε^{205}Tl is –6.0 ± 0.6, with an average concentration of 13 ng/g (Owens, 2019). One of two major marine sinks is low-temperature oceanic crust alteration (ε^{205}Tl = –12 to –6), which represents ~63% of marine Tl outflux (Owens, 2019). The other large Tl sink is its adsorption to Mn-oxides and accumulation in marine Fe-Mn crusts in oxic settings (ε^{205}Tl = +6 to +12), which was calculated to constitute ~32% of the ocean's Tl removal (Owens et al., 2017 and references therein). Euxinic/anoxic sediments in modern marine basins and suboxic sediments in oxygen minimum zones (OMZs) are minor sinks, and represent 4% and 1% of Tl outflux from the ocean, respectively (Owens, 2019). The Tl isotope composition of euxinic sediments is largely dependent on the global seawater Tl isotope composition, and the degree of restriction between the local sedimentary basin and the open ocean (Owens et al., 2017). Euxinic sediments of moderately restricted modern basins, like the Cariaco Basin, better reflect the Tl isotope composition of the open ocean but are slightly heavier (ε^{205}Tl = ~−5.5), whereas strongly restricted basins, like the Back Sea, better reflect the Tl compositions of other inputs (ε^{205}Tl = ~−2.5), such as

rivers and aerosols into the basin (Owens et al., 2017). The former also accumulates more Tl in its sediments (300 - 886 ng/g or 0.30 - 0.89 ppm) than the latter (119 - 584 ng/g or 0.12 - 0.59 ppm) (Owens et al., 2017). Modern anoxic, non-euxinic (i.e. ferruginous) basin sediments, like in the Santa Barbara Basin, exhibit Tl isotope compositions slightly heavier than seawater ($\varepsilon^{205}Tl = -5.6 \pm 0.1$) and concentrations between 0.38 and 0.74 ppm (n = 4; Fan et al., 2020), similar to moderately restricted, euxinic sediments.

3.1.2 Geochemical Behaviour

Soluble marine Tl is naturally found as either Tl(I) or Tl(III), with calculations suggesting 1 – 5% of modern seawater is composed of Tl(III) (Rehkämper & Nielsen, 2004). Sorption to Fe-Mn oxyhydroxide particles (Bidoglio et al., 1993; Nielsen et al., 2013; Peacock & Moon, 2012; Rehkämper et al., 2002) and clay minerals (Matthews & Riley, 1970) is a mechanism for scavenging Tl from seawater. The attraction of Tl(I) to the outer sphere of hydrogenic hexagonal birnessite particulates ($(Na, Ca, K)_{0.6}(Mn^{4+}, Mn^{3+})_2O_4 \bullet 1.5H_2O$) oxidizes dissolved Tl(I) to Tl(III), which then allows Tl(III) to securely complex to vacancies in the inner sphere of the crystal structure and precipitate out of seawater (Bidoglio et al., 1993; Nielsen et al., 2013; Peacock & Moon, 2012). Thallium adsorption to hexagonal birnessite is stronger than to Fe-oxides and Fe-oxyhydroxides (i.e. ferrihydrite ($Fe_5HO_8 \bullet 4H_2O$), goethite ($FeO[OH]$), and hematite (Fe_2O_3)) because Tl adsorbs to these minerals through electrostatic interactions, compared to the secure complexation with hexagonal birnessite (J. Liu et al., 2023). As for clays, illite and smectite are common hosts for Tl, and illite exhibits higher affinity for Tl than smectite (Martin et al., 2018). Thallium adsorption and complexation to illite is attributed to similar size and charge as potassium (K), which is found in the interlayers of illite's structure (Wick et al., 2018). Martin et al. (2018) ranked mineral affinity for Tl as follows: Mn-oxides > illite > smectite ~ ferrhydrite ≥ goethite. In addition, Tl is chalcophilic and commonly found in pyrite, including sedimentary pyrite (Nielsen et al., 2009, 2011, 2017). The Tl-S bond is covalent, and Tl is naturally found as Tl(I) within pyrite (Garrido et al., 2020).

3.1.3 Isotopic Behaviour

Thallium consists of two naturally occurring stable isotopes, Tl-203 and Tl-205. Mass-independent nuclear volume effects dominate as the main Tl isotope fractionation mechanism among marine Fe-Mn precipitates (Peacock & Moon, 2012; Schauble, 2007). Adsorption to hexagonal

birnessite initiates equilibrium fractionation due to nuclear field shift effects caused by Tl oxidation (Peacock & Moon, 2012; Schauble, 2007). Nuclear volume fractionation causes the Tl(III) species to be more abundant in Tl-205 than Tl-203 (Schauble, 2007), and in turn, causes hexagonal birnessite to have isotopically heavy Tl compositions ($\varepsilon^{205}Tl = 6 - 12$) in comparison to modern seawater ($\varepsilon^{205}Tl = -6$) (Nielsen et al., 2013, 2017; Owens et al., 2017). Other Mn-oxides (i.e. triclinic birnessite and todorokite $(Na, Ca, K, Ba, Sr)_{1-x}(Mn, Mg, Al)_6O_{12} \bullet 3\text{-}4H_2O$) incorporate Tl(I) into their structure through cation exchange reactions (Wick et al., 2019), and therefore, should not induce an isotope fractionation. Fractionation generally does not occur during adsorption to Fe-oxyhydroxides because it does not require a redox reaction, but instead requires a ligand exchange reaction between Tl(I) and surficial hydroxyl (OH) groups (J. Liu et al., 2023). Adsorption to ferrihydrite favours heavier Tl-205, but only induces a minor Tl isotope fractionation and is the result of shorter and stronger bonds with Tl-205 compared to Tl-203 (J. Liu et al., 2023). It is assumed that adsorption to clay minerals does not cause appreciable isotope fractionation because it also does not require a redox reaction (Martin et al., 2018). Mass-dependant equilibrium fractionation favours Tl-205, resulting in heavier isotope compositions in Fe-Mn crusts, but only contributes to 25% of total redox fractionation processes (Dauphas & Schauble, 2016; Schauble, 2007). In contrast, mass-dependant kinetic fractionation occurs during degassing and evaporation processes, and causes lighter Tl-203 to become enriched in the gas phase (Nielsen et al., 2017).

Because the formation of Tl-rich pyrite does not require the oxidation of T(I) to Tl(III), Nielsen et al. (2011) suggest heavier Tl isotope values in early diagenetic pyrite in black shales are due to Tl-205 delivery to euxinic marine sediments via Fe-Mn oxyhydroxide particulates. Euxinic and ferruginous sediments have been observed to quantitatively remove Tl from pore and bottom-waters, and record the original Tl isotope value of the overlying water column (Fan et al., 2020; Ostrander et al., 2023; Owens et al., 2017; Y. Wang et al., 2022).

In the context of ancient global ocean redox, it is thought that periods of expanded marine euxinia would decrease the oxic regions required for accumulation of Fe-Mn crusts along the seafloor (Owens, 2019). The decrease in oxic seafloor extent would shift the mass balance to decreased Tl accumulation in the Fe-Mn crust oxic sink and increased Tl available for euxinic/anoxic and suboxic sinks (Owens, 2019). Since the preferential sequestering of Tl-205 by Mn-oxides of the oxic sink would diminish, seawater would be enriched in Tl-205 and this mass balance shift would also be apparent in the euxinic/anoxic sediment archives as an increase in heavier Tl-205 accumulation. Assuming

quantitative Tl removal from local bottom-waters to the euxinic/anoxic sediments, these sediments would directly capture the global seawater value if the local depositional environment was well-connected to the open ocean (Owens, 2019). Therefore, ancient sedimentary ε^{205}Tl values of black shales that are more positive (i.e. heavier) than the modern ocean value of –6 ε units indicate periods of globally expanded euxinia/anoxia in comparison to the modern ocean (Owens, 2019).

3.2.0 Molybdenum

3.2.1 Geochemical Behaviour

Molybdenum is commonly found as soluble molybdate (MoO_4^{2-}) in oxic waters, and does not readily react with marine clays and organic matter at pH > 3 (S. Goldberg et al., 1996), but has an affinity to adsorb onto hydrogenic Fe-Mn oxyhydroxide particulates (Fu, 2020; Little et al., 2015). The Mn-oxide birnessite is the dominant phase controlling Mo adsorption onto Fe-Mn oxyhydroxides (Ashiwabara et al., 2009; Barling et al., 2001; Wasylenki et al., 2008, 2011), however, molybdate is known to absorb onto the minor Fe-oxyhydroxide phases (Ashiwabara et al., 2009; T. Goldberg et al., 2009, 2012). A di-protonated Mo species, identified as molybdic acid ($MoO_2(OH)_2$), facilitates molybdate adsorption onto the surface of birnessite, and ultimately forms polymolybdate complexes (Tossell, 2005; Wasylenki et al., 2011). This sorption mechanism may permit subsequent release of Mo because of its likely reversibility (Wasylenki et al., 2008) and may cause soluble Mo to diffuse back into the water column. Mo is also known to adsorb as di-protonated species onto Fe-oxyhydroxide phases (Gustafsson, 2003), however, the exact Mo species on natural, hydrogenic Fe particles is still not known (T. Goldberg et al., 2009, 2012). The hyper-enrichment of oxic pelagic sediments and Fe-Mn oxyhydroxide nodules and crusts, which have authigenic Mo concentrations that reach 100s to 1000s of ppm, may be attributed to Mo co-precipitation with and/or adsorption to significant amounts of insoluble Fe-Mn oxyhydroxides in oxic waters (Kendall et al., 2017 and references therein). However, these oxic sinks have a tendency to leak Mo. Reductive dissolution of buried Fe-Mn oxyhydroxides in the presence of organic matter may release and diffuse Mo into the overlying water column (Kendall et al., 2017 and references therein). Oxic marine sediments with low Mn enrichments do not efficiently sequester Mo and exhibit concentrations similar to continental crust ([Mo] = ~1– 2 ppm; Tissot et al., 2013). Suboxic ($[O_2]_{aq} < 10$ μM and $[H_2S]_{aq} < 1$ μM) marine sediments do not accumulate a significant amount of Mo (Crusius et al., 1996; Nameroff & Balistrieri, 2002), and are not strong Mo sinks.

In euxinic water columns, molybdate converts into highly reactive tetrathiomolybdate (MoS_4^{2-}) or polysulfides ($Mo(IV)X(S_4)S^{2-}$, where X can be O or S), which allows Mo to be scavenged from marine waters by S-rich organic matter and Fe-bearing sulfide minerals (Dahl et al., 2013; Erickson & Helz, 2000; Helz et al., 1996; Tribovillard et al., 2004). In the presence of aqueous sulfur in the form of H_2S or HS^-, molybdate reacts to form thiomolybdates (Erickson & Helz, 2000; Tossell, 2005). A four-step reaction is "switched on" if $[H_2S]_{aq} > 11$ μM in the water column, which cause intermediate mono-, di-, and trithiomolybdates ($MoO_3S^{2-} \rightarrow MoO_2S_2^{2-} \rightarrow MoOS_3^{2-}$) to form and then convert to the final tetrathiomolybdate compound (MoS_4^{2-}) (Erickson & Helz, 2000; Tossell, 2005). Free aqueous hydrogen sulfide concentrations less than 11 μM results in partial conversion of MoO_4^{2-} to less-reactive intermediate thiomolybdates species (Erickson & Helz, 2000; Tossell, 2005). Polysulfides form when aqueous zero-valent sulfur (S_8) reacts with trithiomolybdate ($MoOS_3^{2-}$) to create a ring-like structure (Dahl et al., 2013; Vorlicek et al., 2004). Dahl et al. (2013) note that Fe-sulfide minerals readily scavenge polysulfides. In sulfidic waters, Mo has been observed to be reduced in the presence of OM, and then precipitate as Mo-sulfide compounds (Scholz et al., 2017). However, it is argued that the correlations between Mo and organic carbon are an indirect result of microbially mediated oxidation of OM associated with sulfate reduction to sulfide (Helz & Vorlicek, 2019). In sulfidic pore waters, authigenic Mo can coprecipitate with Fe-sulfide phases, as long as the total sulfide concentration is at least 0.1 μM (Zheng et al., 2000). Without soluble Fe present, authigenic Mo can precipitate as a sulfide if the total aqueous sulfide concentration of the pore waters is at least 100 μM (Zheng et al., 2000).

Scott & Lyons (2012) outlined a general criterion to assist with interpretations of Mo concentrations in ancient black shales based on conditions in modern euxinic marine environments:

1) Authigenic accumulations between continental crust values (1 – 2 ppm; Tissot et al., 2013) and 25 ppm may reflect the presence of dissolved sulfide confined to the pore waters in the sediment column.
2) Authigenic accumulations >100 ppm indicate excess amounts of dissolved Mo and aqueous sulfide were present in the euxinic water column for prolonged periods of time, with a minimum of one year.
3) Authigenic accumulations between 25 and 100 ppm suggest several more factors influenced Mo sequestration and require further investigation. Factors could include high sedimentation rates that dilute sedimentary trace metal concentrations in euxinic environments, low initial dissolved Mo concentrations in more restricted basins, the pH of the water column that dictate the

behaviour of Mo depositional mechanisms, and the depositional environment's ability to fluctuate between euxinic and non-euxinic conditions.

3.2.2 Isotopic Behaviour

Mo has seven naturally occurring stable isotopes: Mo-92, Mo-94, Mo-95, Mo-96, Mo-97, Mo-98, and Mo-100 (Anbar, 2004). In current marine geochemical studies, the $\delta^{98/95}$Mo notation is used because of the significant difference in mass between Mo-98 and Mo-95, as well as the greater abundance of the two compared to the other five isotopes, and is calculated as (Nägler et al., 2014; M. White, 2013):

$$\delta^{98}\text{Mo (‰)} = 10^3 \times [(^{98}\text{Mo}/^{95}\text{Mo}_{\text{sample}}) \div (^{98}\text{Mo}/^{95}\text{Mo}_{\text{NIST SRM 3134}}) - 1] + 0.25‰$$

Molybdenum isotope fractionation on the surface of the Mn-oxide birnessite is dominated by slow, mass-dependent, equilibrium fractionation (Barling et al., 2001; Dahl et al., 2010; Neubert et al., 2008; Tossell, 2005). Wasylenki et al. (2011) observed a change in molybdate's coordination geometry from a tetrahedral structure to an octahedral one while reacting with molybdic acid during adsorption. The structural change favours lighter Mo isotopes to preferentially bond to molybdic acid and form the polynuclear complexes (Wasylenki et al., 2011). Fe-oxyhydroxides also preferentially adsorb lighter Mo isotopes (T. Goldberg et al., 2009), but have a diminished Mo isotope fractionation compared to Mn-oxides due to the presence of both tetrahedral and octahedral Mo species, resulting in adsorption of both light and heavy Mo isotopes (Wasylenki et al. 2011). Goldberg et al. (2009) note that fractionation between dissolved and adsorbed Mo phases ($\Delta^{98}\text{Mo}_{\text{diss-ads}}$) is controlled by adsorption factors such as pH and the coordination geometry of the adsorbed Mo species, but these also vary among different sizes of particle surface area and different Fe-oxyhydroxide minerals, such as ferrihydrite ($\Delta^{98}\text{Mo}_{\text{diss-ads}} = 0.83 \pm 0.60‰$), goethite ($\Delta^{98}\text{Mo}_{\text{diss-ads}} = 1.4 \pm 0.48‰$) and hematite ($\Delta^{98}\text{Mo}_{\text{diss-ads}} = 2.19 \pm 0.54‰$). As a result of fractionation by Fe-Mn oxyhydroxides, modern oxic Fe-Mn crusts have lighter Mo isotope compositions ($\delta^{98}\text{Mo} = –0.7‰$) compared to seawater ($\delta^{98}\text{Mo} = 2.3‰$) (Nägler et al., 2014; Poulson et al., 2006). Sediments that have overlying mildly oxygenated bottom-waters are split into three groups: 1) Mn-rich sediments with low $[H_2S]_{aq}$ in porewaters ($\delta^{98}\text{Mo} = –1.0‰$ to $+0.4‰$); 2) Fe-rich sediments with low $[H_2S]_{aq}$ in porewaters ($\delta^{98}\text{Mo} = –0.5‰$ to $+2‰$); and 3) sediments with high $[H_2S]_{aq}$ in porewaters ($\delta^{98}\text{Mo} = 1.6 \pm 0.2‰$) (T. Goldberg et al., 2012).

In experimental euxinic conditions, kinetic fractionation favoured lighter Mo isotopes to form into tetrathiomolybdate, which resulted in the water column becoming isotopically heavier in Mo after

the tetrathiomolybdate compounds are removed from solution (i.e. become insoluble) (Kerl et al., 2017). Restricted euxinic basins allow for long-term and consistent contact between Mo species and dissolved sulfides, which allows for chemical equilibrium and quantitative conversion of molybdate to tetrathiomolybdate and polysulfides (Erickson & Helz, 2000; Helz et al., 2011; Nägler et al., 2011; Scholz et al., 2013; Tossell, 2005; Vorlicek et al., 2004). Also, near-quantitative scavenging of the tetrathiomolybdates and polysulfides by S-rich organic matter and Fe-sulfide minerals in restricted basins allows almost all aqueous bottom-water Mo to accumulate in euxinic sediments with little to no net isotope fractionation, providing that the aqueous sulfide concentration remains at or above 11 μM (i.e. strongly euxinic) (Erickson & Helz, 2000; Neubert et al., 2008; Scholz et al., 2013; Tossell, 2005). As a result, authigenic sedimentary Mo in restricted, euxinic marine sediments reflect a similar Mo isotopic composition to the overlying water column (Neubert et al., 2008; Poulson et al., 2006; Scholz et al., 2013; Tossell, 2005). Highly restricted basins, like the modern Black Sea, that have sediments deposited into strongly euxinic bottom-waters also record the Mo isotope composition of open ocean seawater ($\delta^{98}Mo = 2.34 \pm 0.10‰$) due to the long oceanic residence time of Mo (~440 kyr; Miller et al., 2011) (Neubert et al., 2008). However, if the concentration is below 11 μM (i.e. weakly euxinic) like in the less restricted Cariaco Basin and Baltic Sea, the presence of intermediate thiomolybdates and non-quantitative Mo removal favours sequestration of lighter Mo into sediments, and creates an isotopic offset between the water column and sediments ($\Delta^{98}Mo_{sediment\text{-}water}$ up to 3‰) that results in a wide range of sedimentary $\delta^{98}Mo$ values (–0.6 to +1.8‰; Kendall et al., 2017; Neubert et al., 2008). In euxinic and anoxic, non-sulfidic settings, organic particulates have the affinity to adsorb octahedrally coordinated Mo complexes, similar to Mo adsorption to Fe-Mn oxyhydroxides, and therefore, organic matter (OM) scavenges lighter Mo isotopes (Dahl et al., 2017; King et al., 2018).

Similar to Tl isotopes, periods of expanded global ocean euxinia can be inferred from sedimentary archives with the understanding of the global Mo mass balance relationships. Extensive ocean euxinia will decrease the surface area of well-oxygenated seafloor, where Mo is adsorbed and buried with Fe-Mn oxyhydroxides in Fe-Mn crusts and with OM in pelagic sediments (i.e. the oxic sink) (Morford & Emerson, 1999; Siebert et al., 2003). Instead of being captured by the oxic sink, lighter-mass Mo isotopes remain in the water and shift the seawater composition to less positive (i.e. lighter) $\delta^{98}Mo$ values. The decreased flux to the oxic sink allows for an increased flux of aqueous Mo into euxinic sediments (i.e. the euxinic sink) and, assuming these sediments quantitatively capture

seawater Mo compositions, results in ancient sedimentary $\delta^{98}Mo$ values less positive (i.e. lighter) in black shales than the modern seawater value of 2.34‰ (Barling et al., 2001; Pearce et al., 2008).

3.3.0 Uranium

3.3.1 Geochemical Behaviour

Uranium is commonly found as U(VI) in soluble uranyl ions (UO_2^{+}) that complex as soluble carbonate ions ($UO_2(CO_3)_3^{4-}$) and phosphate complexes ($(UO_2)_2(PO_4)_2 \cdot nH_2O$, n = 6-12) in oxic marine waters (Calvert & Pedersen, 1993; Čejka & Muck, 1984; Ivanovich & Harmon, 1992; Klinkhammer & Palmer, 1991), which are unreactive in water columns at typical marine pH and temperatures (Tribovillard et al., 2006). Uranium adsorption onto the Mn-oxide birnessite (Brennecka et al., 2011) and onto Fe-oxyhydroxide phases (Waite et al., 1994) involves a change in the geometric coordination of uranyl ions, which is reminiscent of Mo adsorption to Fe-Mn oxyhydroxides, however, the exact mechanism has not been identified. Although Fe-Mn oxyhydroxides have the potential to adsorb U, their affinity to each other is weak (Algeo & Tribovillard, 2009; Bura-Nakić et al., 2018) and U is not effectively enriched in oxic sediments (Morford, Martin, François, et al., 2009).

In anoxic and euxinic water columns, dissolved U is removed from solution through four different pathways (Brüske et al., 2020): 1) uptake and biotic reduction of soluble U(VI) to insoluble U(IV) by sulfate-reducing, Fe-reducing, and fermenting bacteria (Rolison et al., 2017; Stylo et al., 2015); 2) reduction of U(VI) and complexation with sinking organic particulates (Zheng et al., 2002a) or in an organic floccule layer at the sediment-water interface (Andersen et al., 2020; Cheng et al., 2020); 3) reduction of U(VI) by H_2S (Barnes & Cochran, 1993); and 4) diffusion of soluble U(VI) from the water column into anoxic pore waters, then reduction and precipitation of U(IV) via pathways 1 and 3 (Klinkhammer & Palmer, 1991; Morford et al., 2005). Insoluble U precipitates as uraninite (UO_2) during abiotic reduction, or as organic-metal ligands when reduced with biogenic matter (Algeo & Tribovillard, 2009). The diffusion-reduction mechanism (pathway 4) is thought to be the dominant enrichment mechanism in most anoxic/euxinic settings, however, there is still debate on whether U reduction mainly occurs in sediment pore waters or in the water column. Microbial reduction of U is commonly located below the Fe(III) - Fe(II) redoxcline where bacteria use U(VI) as an electron accepter (Little et al., 2015; Lovley et al., 1991; Morford et al., 2005; Morford, Martin, & Carney, 2009). Remobilization (i.e. re-solubilisation) of U in surface sediments is caused by either bioturbation (Zheng et al., 2002b) or irrigation of anoxic/euxinic sediments with oxygen-rich water (Morford, Martin, & Carney, 2009).

Remobilized U either releases back into the water column or diffuses deeper into the sediments (McManus et al., 2005).

3.3.2 Isotopic Behaviour

Natural U isotopes consist of radioactive U-234, U-235, and U-238, and geochemical studies on geological materials older than 1 Ma must analyze U-235 and U-238, and not U-234, because of their longer half-lives (Andersen et al., 2014 and references therein). The $\delta^{238}U$ notation is calculated as (Andersen et al., 2014):

$$\delta^{238}U\ (‰) = 10^3 \times [(^{238}U/^{235}U_{sample}) \div (^{238}U/^{235}U_{CRM\ 145}) - 1]$$

Mass-dependent, equilibrium isotope fractionation occurs during U adsorption onto Fe-Mn-oxyhydroxides in oxic waters, which preferentially incorporates lighter ^{235}U and results in a offset of $\Delta^{238}U_{diss\text{-}ads} = \sim 0.2‰$ (Brennecka et al., 2011; Weyer et al., 2008). Similar to Mo isotope fractionation on Fe-Mn oxyhydroxides, the change in coordination geometry of uranyl ions during adsorption controls U isotope fractionation (Brennecka et al., 2011; Weyer et al., 2008).

Mass-independent, equilibrium isotope fractionation occurs during the reduction of U(VI) to U(IV) in anoxic and euxinic waters (Schauble, 2006; Weyer et al., 2008). This U isotope fractionation is volume-dependent and is driven by nuclear field shift effects, resulting in anoxic/euxinic sediments enriched in heavier U-238 (McManus et al., 2005; Schauble, 2007). The fractionation factor (i.e. the isotopic difference between sediments and water; $\Delta^{238}U_{sediment\text{-}water}$) during the diffusion-reduction pathway ranges between 0.60‰ and 0.84‰ (Brüske et al., 2020 and references therein). Non-diffusion-limited U reduction by organic matter in the water column, either by particles or permeable flocculant layers, also causes a large $\Delta^{238}U_{sediment\text{-}water}$ from 0.60‰ up to 1.2‰ (Andersen et al., 2020; Clarkson et al., 2023). The fractionation factor during microbial reduction of U(VI) to U(IV) ($\Delta^{238}U_{microbe\text{-}water}$) ranges between 0.68‰ and 0.99‰ (Andersen et al., 2020; Basu et al., 2014). Strongly euxinic conditions promote faster reduction reactions and quantitative removal of U from porewaters, which results in little to no fractionation and $\delta^{238}U$ values similar to the overlying seawater (Brüske et al., 2020). In contrast, the low $[H_2S]_{aq}$ of weakly euxinic conditions causes slower reduction rates and partial U reduction, which imparts fractionation between the sediments and the water column, and results in higher, more positive sedimentary $\delta^{238}U$ values compared to modern seawater values ($\delta^{238}U = -0.39 \pm 0.02‰$) (Brüske et al., 2020).

Reconstructing ancient global redox conditions assumes changes in U accumulation in redox-associated sinks, while maintaining steady fluxes and isotope compositions of other sources and sinks. Unlike Tl and Mo, the largest modern sinks of U are suboxic/reducing sediments (~26% of total ocean outflux) and euxinic sediments (~20% of total ocean outflux) (Lau et al., 2019). During periods of expanded global ocean euxinia, the surface area of these sinks would increase and remove more of the heavier U-238 isotope during reduction pathways into anoxic sinks, leaving lighter U-235 in seawater (X. Lu et al., 2020). Therefore, the quantitative U removal from bottom-waters to sediments in the local depositional environment would preserve global seawater $\delta^{238}U$ values and result in lower (i.e. lighter) sedimentary $\delta^{238}U$ compositions in black shales compared to modern seawater ($\delta^{238}U = -0.39‰$).

3.4.0 Fe-Mn Oxyhydroxides

In natural marine settings, manganese is found either as soluble Mn(II) in anoxic environments or insoluble Mn(III) and Mn(IV) in oxygenated waters (Calvert & Pedersen, 1996), with the latter known to form Mn-oxyhydroxides (MnO_x, $x > 2$; Neretin et al., 2003). There are many hydrogenic minerals that are considered Mn-oxyhydroxides, however, the most abundant are todorokite, and triclinic and hexagonal birnessite, in no particular order (Burns et al., 1977). While MnO_x minerals are found in the upper, oxic portion of the water column, Fe-oxyhydroxide minerals aggregate to MnO_x that settle into the lower, weakly oxic/suboxic sections of the water column (Dellwig et al., 2010). Minerals such as ferrihydrite, goethite, lepidocrocite (γ-FeO[OH]), and hematite are considered common marine Fe-oxyhydroxides (Dellwig et al., 2010; T. Goldberg et al., 2009), which form as coatings on settling MnO_x particles (Dellwig et al., 2010). Experiments by Dellwig et al. (2010) show Fe phases accrete when soluble Fe(II) is oxidized by Mn(IV) of the MnO_x core, or oxidized by free aqueous O_2. As described in previous sections, Fe-Mn oxyhydroxides have an affinity to adsorb TMs (i.e. Tl, Mo) and potentially transport them to basin sediments, which may significantly enrich sediments in these TMs under particular water redox conditions (Dellwig et al., 2010; Scholz et al., 2013, 2018). Coined as "shuttles", these Fe-Mn oxyhydroxide particles can laterally or vertically transport TMs to deeper and more euxinic areas of a basin.

3.4.1 Lateral Shuttle

The lateral or "benthic redox" shuttle requires diffusion of soluble Mn(II) and Fe(II) from suboxic porewaters on the basin shelf into the overlying oxic water column, where they are oxidized and precipitate as Fe-Mn oxyhydroxides or form metal-organic complexes, and adsorb dissolved TMs

(Figure 6a) (Lenstra et al., 2020). From the shelfal water column, they are laterally transported offshore to deeper sections of the basin, where the particulates sink into euxinic bottom-waters. Particulate Fe-Mn is reduced back to dissolved Mn(II) and Fe(II) at the aqueous sulfide boundary (i.e. redoxcline) and diffuse upwards into overlying oxic waters. Some Fe and Mn continues to cycle at the redoxcline where it is oxidized, is precipitated, sinks, then is reductively dissolved and diffuses upwards again (Lenstra et al., 2020). The "shuttle" is attributed to the Fe-Mn particulates that reductively dissolve below the redoxcline and then re-precipitate as insoluble sulfide (Fe and Mn) and carbonate (Mn) minerals, which scavenge and deliver TMs to the sediment floor (Chen et al., 2022).

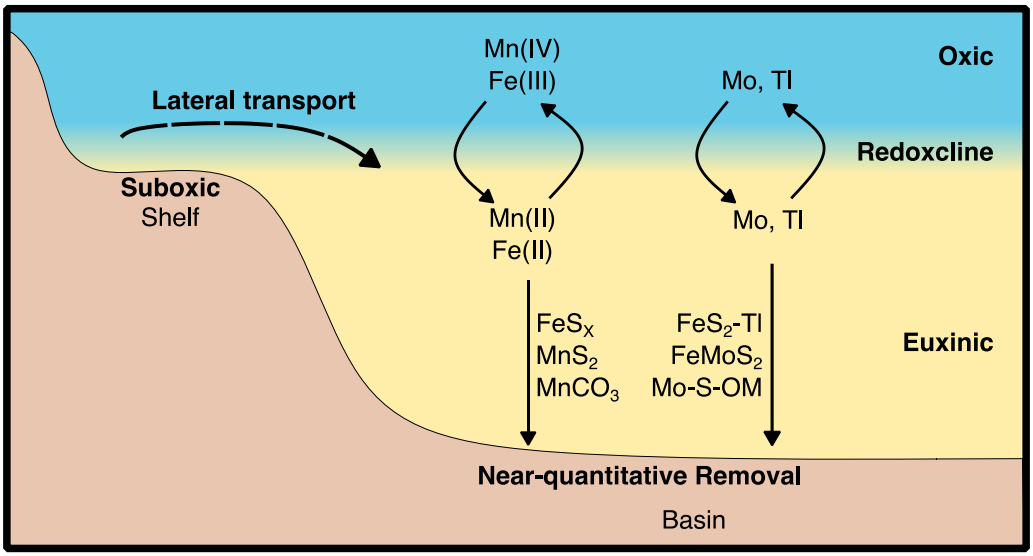

Figure 6a Diagram of the lateral particulate shuttle. Modified from Chen et al. (2022).

3.4.2 Vertical Shuttle

The vertical or "particulate" shuttle occurs solely within the deep basin and requires a deeper redoxcline that is close to the sediment-water boundary (Figure 6b). Particulate Fe-Mn in the overlying oxic waters adsorb TMs and sink downwards towards the redoxcline, where reductive dissolution occurs. Like the lateral shuttle, dissolved Fe(II) and Mn(II) diffuses upwards and cycles around the redoxcline, alternating between soluble and insoluble phases. The "shuttle" occurs when particulate Fe-Mn releases adsorbed TMs close to the sediment-water boundary during reductive dissolution (Dellwig et al., 2010). Trace metals are then scavenged by pyrite and OM or react with aqueous sulfide to form sulfide minerals and are deposited in the sediments. In order for the vertical shuttle to enrich significant amounts of sedimentary Mo (>100 ppm), Scholz et al. (2013) suggests the residence time of the deep

basin water must be relatively short, from several weeks to a few years. The constant renewal of ocean water to the system allows for an influx of free dissolved oxygen, major elements (i.e. Fe and Mn) and TMs (i.e. Mo and Tl). This maintains the circulation of the particulate shuttle and significant TM enrichment of the sediments (Dellwig et al., 2010). Weakly restricted basins that have intermittent influx of oceanic water, or continental margins with upwelling cells in the oxygen-minimum zones are ideal settings for periodic renewal of seawater (Scholz et al., 2013).

While authigenic Mo sediment accumulation is remarkably accelerated, U is much less affected

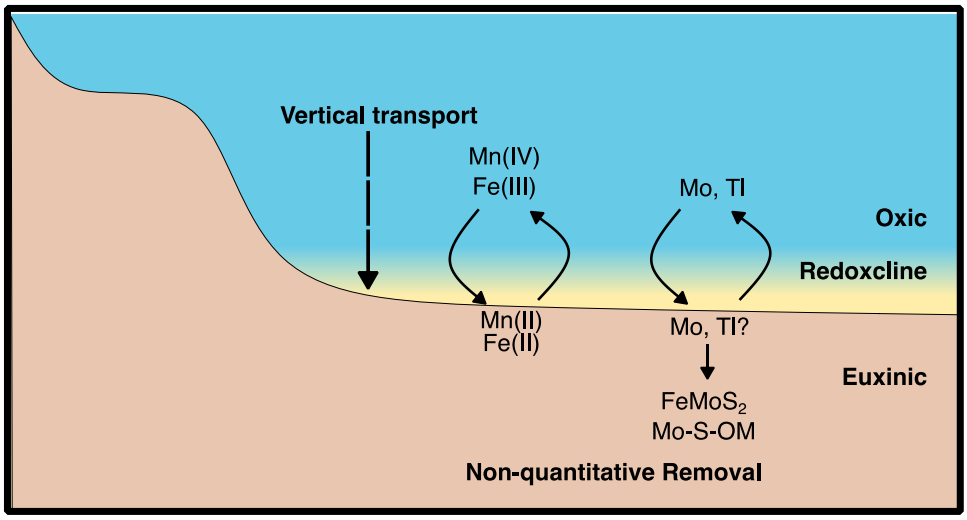

Figure 6b Diagram of the vertical particulate shuttle. Question mark represents unknown fate of Tl. Modified from Chen et al. (2022).

by the Fe-Mn oxyhydroxide shuttle and thus does not become enriched to the same extent (Algeo & Tribovillard, 2009). Authigenic Tl accumulation has been investigated in regards to local and global Fe-Mn oxyhydroxide burial and/or shuttling in ancient sediments (e.g. Fan et al., 2020; Ostrander et al., 2017, 2020; and Owens et al., 2017), however, a recent study of the modern Black Sea sediments has concluded that lateral Fe-Mn particulate shuttling does not influence the local accumulation of sedimentary Tl (Chen et al., 2022). It is suggested that reductive dissolution of Fe-Mn particulates at the Black Sea's shallow chemocline releases the majority of adsorbed Tl back into the water column instead of becoming buried in the basin sediments (Chen et al., 2022). The effect of vertical particulate shuttling on Tl accumulation and isotope expressions have not been assessed in modern environments, and its influence remains relatively unknown (Chen et al., 2022).

3.5.0 Multi-Element Proxies

Due to the possibility of anomalous trends from using a single element proxy, which are trends that do not reflect those of modern analogue basins (e.g. Herrmann et al. (2012)), the comparison of several elements is more reliable to constrain local basin conditions because differences in removal pathways can be exploited (e.g. Tribovillard et al., 2006). The following are the current multi-elemental systems that can assist in interpreting local paleoredox, paleohydrographic, and paleosalinity conditions.

3.5.1 Mo - U Elemental Covariation

The relationship between authigenic Mo and U accumulation in marine sediments can assist with interpreting the benthic redox conditions, the presence and efficiency of an Fe-Mn shuttle, and the restriction to the open ocean in marine basins (Algeo & Tribovillard, 2009; Tribovillard et al., 2012). Figure 7 summarizes these interpretations by comparing the trace metal enrichment factors (EFs), which is the relative enrichment of a metal in a black shale compared to average Post-Archean Australian Shale or average upper continental crust (Algeo & Tribovillard, 2009) (see Section 5.4.0 for EF calculation). A weakly restricted basin with a fluctuating, deep-water chemocline and a functioning Fe-Mn particulate

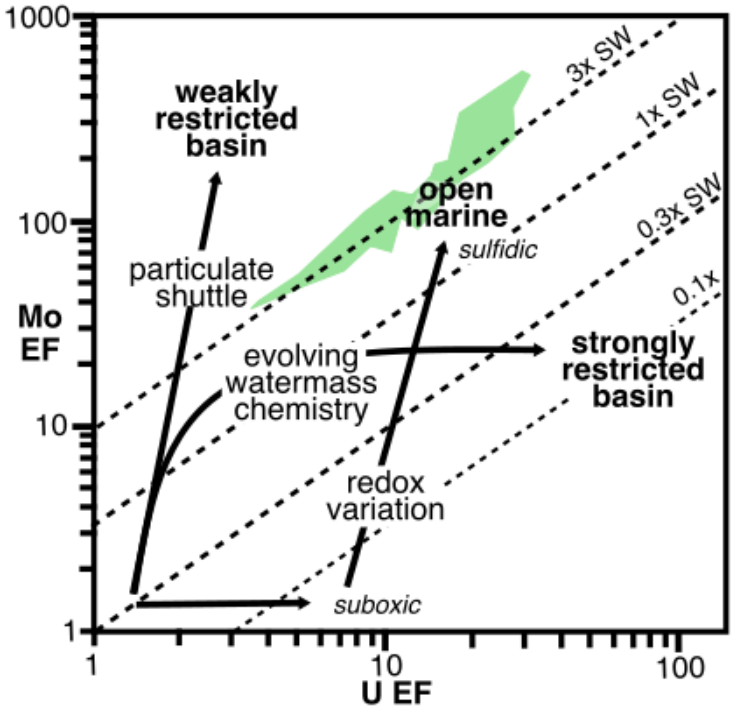

Figure 7 Cross plot between Mo and U EFs. Arrows show trends of different degrees of basin restriction. Green shading represents EFs of Kettle Point black shales. Modified from Algeo and Tribovillard (2009) and Kendall et al. (2020).

shuttle will have a larger increase in Mo enrichment because the particulate shuttle efficiently transports Mo to sediments without significant adsorption and transport of U (Algeo & Tribovillard, 2009; Tribovillard et al., 2012). Therefore, the Mo/U EF ratio of the sediments would be greater than the Mo/U ratio of modern seawater due to the euxinic conditions that promote sedimentary Mo and U enrichment, and particulate shuttling that favour Mo burial in sediments. Renewal of TMs from the ocean into the weakly restricted basin also promotes high Mo and U EFs. In contrast, redox-stratified and stagnant basins that are heavily restricted from open ocean inputs are less likely to have a particulate shuttle and will have some variation in their water column chemistry over time, depending on the initial concentration of dissolved metals, as well as the frequency and magnitude of changes to basin restriction (Algeo & Tribovillard, 2009). In Figure 7, the Mo EFs of a highly restricted basin plateau because kinetic reactions between Mo and $[H_2S]_{aq}$ occur more rapidly than those between U and $[H_2S]_{aq}$, which exhausts the basin's aqueous Mo reservoir before aqueous U (Algeo & Tribovillard, 2009). Sediments underlying suboxic bottom waters will have increasing U enrichment with little to no Mo because U reduction occurs shallower in the sediment column; at or near the sediment-water interface within the Fe-reducing zone, compared to Mo reduction in deeper, sulfidic porewaters in the sulfate-reducing zone (Algeo & Tribovillard, 2009). A shift towards more sulfidic porewaters or bottom-waters causes an increased enrichment in Mo in comparison to U (e.g. Canfield & Thamdrup (2009)) and is caused by the upward, vertical shift of the chemocline from deeper to shallower porewaters or into the water column (Algeo & Tribovillard, 2009).

3.5.2 Mo - U Isotopic Covariation

The water chemistry evolution and restriction of modern euxinic basins can be interpreted by comparing the isotopic compositions of sedimentary Mo and U. These isotope ratios can be used to reconstruct the local marine redox evolution of ancient basins. Figure 8 shows the average $\delta^{98}Mo_{auth}$ and $\delta^{238}U_{auth}$ in sediments of modern basins with varying magnitudes of euxinia and deep-water renewal rates. An inverse correlation between $\delta^{98}Mo_{auth}$ and $\delta^{238}U_{auth}$ is apparent moving from weakly restricted and weakly or intermittently euxinic waters (e.g. Saanich Inlet) to strongly restricted and strongly euxinic waters (e.g. Kyllaren Fjord and Black Sea), with the latter approaching the $\delta^{98}Mo$ and $\delta^{238}U$ of global modern oxygenated seawater. An inverse correlation is apparent between $\delta^{98}Mo$ and $\delta^{238}U$ because lighter-massed Mo isotopes and the heavier U-238 isotope are preferentially removed to euxinic sediments. The Black Sea displays a divergence from the trend of the other basins because of its longer

deep-water renewal time and the predominant diffusion-reduction mechanism that fractionates sediment $\delta^{238}U_{auth}$ around 0.4‰ higher than the modern open ocean U signature (–0.39‰) (Bura-Nakić et al., 2018; Noordmann et al., 2015). A secondary trend for a functioning Fe-Mn particulate shuttle shows the evolution towards lighter $\delta^{98}Mo$ in sediments with minimal change in $\delta^{238}U$. Bura-Nakić et al. (2018) note that the trends take two assumptions into consideration:

1) Mo isotope fractionation between the water column and sediments is substantially larger during non-quantitative removal in weakly restricted basins (e.g. Saanich Inlet) from the water column compared to a smaller Mo isotope fractionation during quantitative or near-quantitative removal in strongly restricted basins (e.g. Kyllaren Fjord and Black Sea).
2) Each basins' fractionation factor ($\Delta^{238}U_{sediment\text{-}water}$) between the deep-water column and sediments is consistent, which means the difference between sedimentary $\delta^{238}U_{auth}$ and $\delta^{238}U_{water}$ remain constant and there is no significant change in fractionation during the input and/or removal of U from the basin's bottom-waters. Consequently, this also assumes that the basins' restriction to the open ocean remains constant.

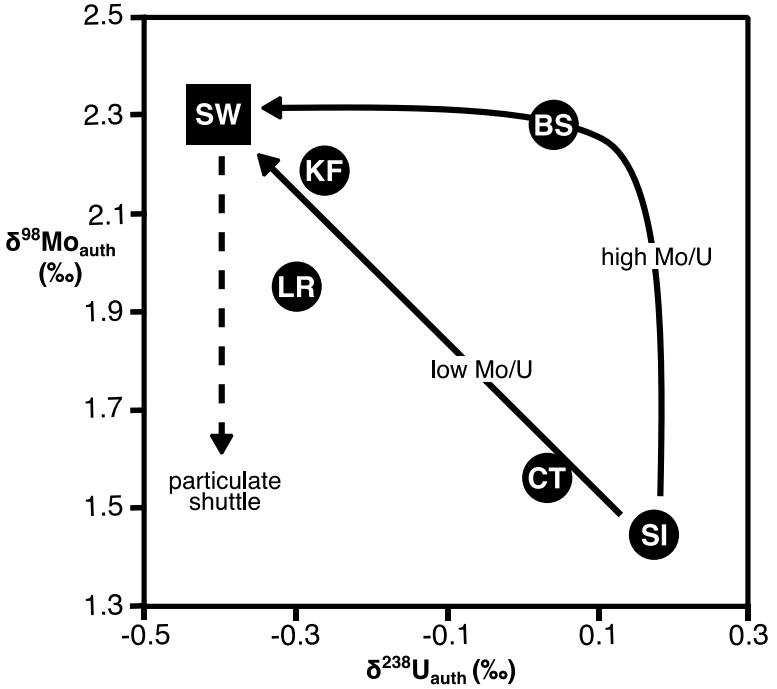

Figure 8 Cross plot of average authigenic Mo and U isotope ratios of modern euxinic basins. BS = Black Sea; CT = Cariaco Trench; KF = Kyllaren Fjord; LR = Lake Rogoznica; SI = Saanich Inlet; SW = seawater; Modified from Bura-Nakić et al. (2018).

3.5.3 Paleosalinity Proxies

Paleosalinity reconstruction of ancient watermasses is a relatively new trace element application. Ratios between boron and gallium (B/Ga), strontium and barium (Sr/Ba), and total sulfur and organic carbon (TS/TOC) are utilized together as proxies to identify three salinity regimes: freshwater (< 1 psu; practical salinity unit), brackish (1 - 30 psu), and marine (30 - 38 psu) (Wei & Algeo, 2020). Thresholds for each regime, which are based on data from modern environments, are as follows (Wei & Algeo, 2020):

- Freshwater: B/Ga < 3, Sr/Ba < 0.2, TS/TOC < 0.1
- Brackish: B/Ga = 3 - 6, Sr/Ba = 0.2 - 0.5, TS/TOC > 0.1
- Marine: B/Ga > 6, Sr/Ba > 0.5, TS/TOC > 0.1

The TS/TOC proxy cannot clearly distinguish between brackish and marine salinities because it depends on aqueous sulfate concentrations and availability of organic matter for microbial sulfate reduction, which are variable in both marine and brackish water (Wei & Algeo, 2020). However, it is suggested that TS/TOC > 0.5 are more likely to be marine than brackish (Wei & Algeo, 2020). The accuracies of the proxies thresholds to predict paleosalinity is around 88% for B/Ga, 66% for Sr/Ba, and 91% for TS/TOC (Wei & Algeo, 2020).

4.0.0 Previous Paleoproxy Research

4.1.0 Local Basin Paleoredox

A paleodepositional model of the Kettle Point Formation, which included local paleohydrographic and water column redox conditions, was interpreted by Bingham-Koslowski et al. (2016) using fossil content and sedimentological data of the entire lithofacies assemblage. More recently, Kendall et al. (2020) utilized geochemical data of the black shale facies, such as the coupled Mo - U isotope paleoredox proxies and trace metal elemental abundances, to interpret stratigraphic trends that reflect changes in local redox conditions of the water column in the Chatham Sag, and also reflect the basin's hydrological connection to the ancient ocean. An inverse correlation between $\delta^{98}Mo$ and $\delta^{238}U$, which corresponded to an upward stratigraphic trend of decreasing $\delta^{98}Mo$ and increasing $\delta^{238}U$, is interpreted as a change from strongly euxinic ($[H_2S]_{aq} > 11$ μM; relatively higher $\delta^{98}Mo$ and lower $\delta^{238}U$) to weakly euxinic ($[H_2S]_{aq} < 11$ μM; lower $\delta^{98}Mo$ and higher $\delta^{238}U$) conditions (Kendall et al., 2020). When comparing the overall authigenic abundances of Mo to U (Mo_{auth}, U_{auth}), all Kettle Point samples showed Mo/U ratios three times higher than modern seawater ratios, which suggested the Chatham Sag maintained a connection with the open ocean throughout the Kettle Point Formation's deposition (Kendall et al., 2020). An Fe-Mn particulate shuttle may have also been present, which is reflected in the high Mo accumulation and lower Mo isotope compositions ($\delta^{98}Mo_{auth} = 0.55 - 2.05‰$) compared to the signature of modern seawater ($\delta^{98}Mo = 2.3 \pm 0.10‰$) (Kendall et al., 2020; Poulson et al., 2006). The shuttle may have been most efficient during deposition of the youngest black shales (Unit 4 of the Bingham-Koslowski et al. (2016) model) because it has the lowest $\delta^{98}Mo$ values ($\delta^{98}Mo_{auth} = 0.55 - 1.32‰$) and the highest concentrations of Mo (Kendall et al., 2020). Paleosalinity proxies exhibited a change from marine to brackish conditions moving upsection, which was inferred as a decrease in sea-level that is correlated to major regression of the Latest Famennian (Kendall et al., 2020). The regression increased basin restriction to the open ocean, and thus, diminished the influx of marine waters to the Chatham Sag and emphasized the freshwater input from riverine sources (Kendall et al., 2020).

4.2.0 Global Ocean Paleoredox

Although the stratigraphic trends in Mo and U isotope compositions of the Kettle Point black shales were mostly influenced by local isotope fractionation in the Chatham Sag, Kendall et al. (2020) provided insight on the global redox conditions of the Early Famennian ocean. When plotting Mo and U

isotope compositions in Figure 9, Kendall et al. (2020) noted that the Kettle Point negative trend paralleled that of modern euxinic analogues, however, the Kettle Point values were slightly lower. They concluded that the lower values reflected slightly lower seawater isotope compositions during the Early Famennian, which was caused by greater global sediment sequestration of Mo and U due to a slightly larger extent of ocean euxinia at that time (Kendall et al., 2020). An expansion of ocean euxinia decreases the area of oxic seafloor where lighter-mass Mo isotopes are buried with Mn-oxides and simultaneously increases the area of seafloor where heavier U-238 is removed into euxinic sediments. Therefore, seawater becomes enriched in both lighter Mo and U-235 isotopes and are recorded in the sedimentary archive as lower or more negative δ^{98}Mo and δ^{238}U. The highest δ^{98}Mo (2.0‰) and lowest δ^{238}U (–0.3‰) of the lower Kettle Point Formation represent the isotopic compositions that are the least fractionated from ancient seawater, and are thought to represent the minimum Mo and maximum U coeval seawater isotope compositions (Kendall et al., 2020). Extrapolation of the Kettle Point regression line and using the vertical δ^{98}Mo offset of ~0.3‰ from the modern euxinic basin regression line in

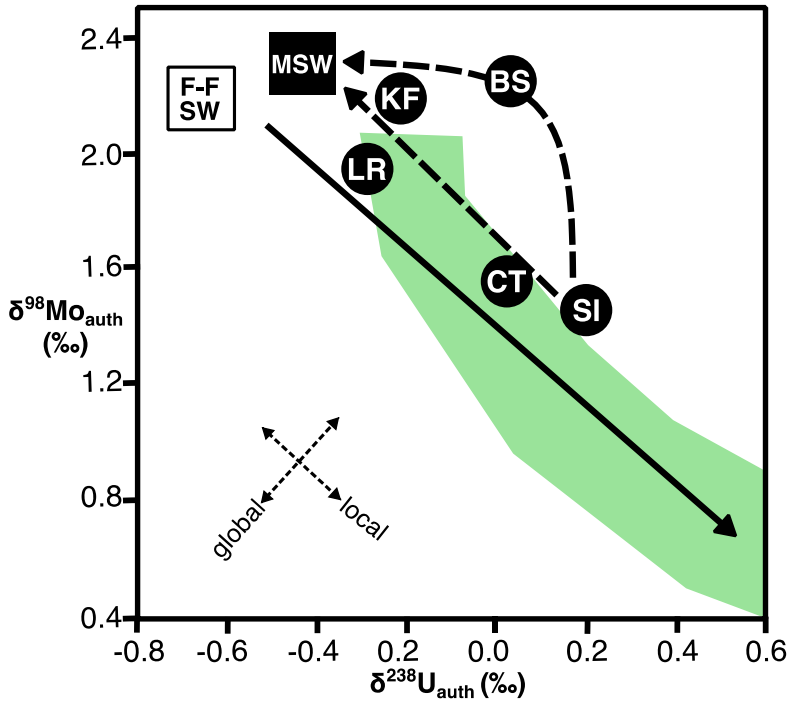

Figure 9 Cross plot of authigenic Mo and U isotope ratios of the Kettle Point black shales. Green shading represents space where black shales generally plot. Solid arrow represents the regression line of the inverse correlation between the two isotope systems; arrowhead indicates general stratigraphic trend from Unit 1 to 4. Smaller dashed arrows represent general trends caused by shifts in either local or global redox conditions. F-F SW = Frasnian-Famennian seawater; MSW = modern seawater. See Figure 8 for other abbreviations. Modified from Kendall et al. (2020).

Figure 8 suggests Early Famennian global seawater $\delta^{98}Mo$ and $\delta^{238}U$ was ~2.0 - 2.2‰ and −0.7 to −0.4‰, respectively, which are slightly lower than modern seawater values of $\delta^{98}Mo = 2.3 \pm 0.1$‰ and $\delta^{238}U = -0.39 \pm 0.02$‰ (Kendall et al., 2020 and references therein). Therefore, the extent of ocean euxinia during the Early Famennian was slightly greater than today (Kendall et al. 2020).

5.0.0 Methods

5.1.0 X-Ray Diffraction Analysis

Bulk rock powder samples were sent to Activation Laboratories (ActLabs) in Ancaster, ON for X-ray diffraction (XRD) analysis. Samples were mixed with corundum, which was used as an internal standard (ActLabs, 2022). Measurements were performed on a Bruker D8 Endeavour diffractometer that was equipped with a Cu X-ray source (ActLabs, 2022). The diffractometer operated under the following parameters: 40 kV and 40 mA; range 4 - 70 deg 2θ; step size 0.02 deg 2θ; time per step 0.5 sec; fixed divergence slit, angle 0.3^0; sample rotation 1 rev/sec (ActLabs, 2022). Mineral identification was determined using the PDF4/Minerals ICDD database, and crystalline mineral quantities were calculated using the Rietveld method (ActLabs, 2022).

5.2.0 Sample Preparations

Sample preparation and mass spectrometry analyses were conducted at the Metal Isotope Geochemistry Laboratory, University of Waterloo, Waterloo, ON.

5.2.1 Total Digestion for Bulk Rock Analysis

Approximately 100 - 150 mg of bulk rock powder were ashed at 550°C for 12 hours to destroy organic matter (Kendall et al., 2020; J. Wang, 2016). Ashed powders were transfer to 22 ml Savillex Teflon beakers and completely digested with a triple-acid method. Samples were first heated in 2.5 mL nitric acid (HNO_3) and 0.5 ml hydrofluoric acid (HF) at 110°C for over 48 hours, then in 3 ml hydrochloric acid (HCl) and 1 mL HNO_3 at 110°C for over 48 h, and finally in 2 mL of HCl at 110°C for 24 hours (Kendall et al., 2020; J. Wang, 2016). Afterwards, the final solution was dried then stored in a 6 M HCl stock solution (Kendall et al., 2020; J. Wang, 2016).

5.2.2 Authigenic Thallium Leach

Approximately 100 mg of bulk rock powder were heated in 6 mL of 2 M HNO_3 at 110°C for 16 hours. The HNO_3 leachate, which contained the authigenic Tl fraction, was separated from the residual sediment by centrifugation. After separation, the authigenic fraction was dried, then heated in 1 mL of 16 M HNO_3 and 1 mL hydrogen peroxide (H_2O_2) at 110°C for 16 hours. This HNO_3 - H_2O_2 treatment was repeated two more times to destroy remaining organic matter. Afterwards, the authigenic fraction was dried then stored in a 6 M HCl stock solution.

5.2.3 Anion Exchange Chromatography

To isolate the authigenic Tl from the rest of the matrix for isotopic analysis, the 6 M HCl stock solutions were purified via an anion exchange chromatographic procedure. The following procedure is modified from Nielsen et al. (2004), Rehkämper et al. (2002), and Rehkämper & Halliday (1999).

The anion chromatography procedure used 0.2 mL of Bio-Rad AG1-X8 anion-exchange resin beds in BioRad Polyprep® plastic chromatography columns. Brominated water (Br_2 water) was produced prior to the column chemistry. Before sample loading, the resin beds were cleaned with a 0.1 M HCl - SO_2 (sulfur dioxide) solution, and then conditioned with 0.1 M HCl solution and a 0.1 M HCl - 1% Br_2 water solution. Afterwards, aliquots of the 6 M HCl stock solutions containing 60 ng of Tl were dried at 110°C, then dissolved in 1 mL of 1 M HCl and 100 µL of Br_2 water. After loading samples into the columns, the major and minor elements were eluted using three different acid solutions. First, a solution of 0.5 M HNO_3 and 3% Br_2 water solution was passed through the column. The second pass was a 2 M HNO_3 - 3% Br_2 water solution, and the third pass was a 0.1 M HCl - 1% Br_2 water solution. Finally, Tl was eluted from the resins using a 0.1 M HCl - SO_2 solution. The Tl fraction was dried down and stored in a 16 M HNO_3 solution. Yield recovery of Tl ranged between 85% and 115%.

5.3.0 Mass Spectrometry Analysis

5.3.1 Elemental Abundances

Elemental abundances were measured on an Agilent 8800 Triple Quadrupole Inductively Coupled Plasma Mass Spectrometer. Internal standards of scandium (Sc), germanium (Ge), indium (In), and bismuth (Bi) were measured to correct instrumental drift. Secondary standards of certified United States Geological Survey (USGS) Water Standards T-207, T-211, and T-225 were measured to verify instrument accuracy and precision, and measurements were in agreement with reported values within 4 - 9%.

5.3.2 Isotope Compositions

The black shale isotope ratios were measured on a Nu Plasma II Multi-Collector Inductively Coupled Plasma Mass Spectrometer. Aliquots contained 20 ng of Tl and spiked with 100 ng of lead (Pb) NIST SRM 981to correct for instrumental mass fractionation effects. Older studies used NIST SRM 997 as the primary Tl standard (e.g. Rehkämper & Halliday, 1999), however, it is no longer available for purchase. Instead, Tl isotope ratios were normalized relative to the primary NIST SRM 3158 Tl

standard, and measurements of SRM 3158 against itself yielded $\varepsilon^{205}Tl_{mean} = 0.0 \pm 0.3$ 2SD (2 standard deviations) (n = 124). Measurements of SRM 3158 against SRM 997 produced an isotopic difference of 0.1 ± 0.3 ε units (2SD, n= 39), which confirmed that the Tl isotope composition of the two standards are statistically indistinguishable.

The ARISTAR Reference Standard was used as a secondary standard ($\varepsilon^{205}Tl_{mean} = 1.6 \pm 0.4$ 2SD, n = 43). Geological reference material from the USGS were also measured, specifically the Columbia River Basalt (BCR-2; $\varepsilon^{205}Tl_{mean} = -2.3 \pm 0.4$ 2SD, n = 5) and the Silver Plume Granodiorite (GSP-2; $\varepsilon^{205}Tl_{mean} = -2.3 \pm 0.8$ 2SD, n = 3) Reference Standards, which were reproducible within error to measurements by Brett et al. (2018) (BCR-2: $\varepsilon^{205}Tl = -2.4 \pm 0.2$ 2SD and GSP-2: $\varepsilon^{205}Tl = -2.5 \pm 0.6$ 2SD). Additionally, black shales from the Velkerri and Wollogorang Formations were also measured, as their Tl isotope compositions are known from previous studies with similar nitric acid leach and anion exchange chromatography preparation (Z. Li et al., 2021). Velkerri and Wollogorang Tl isotope ratios are reported in Table 1. A mean deviation of 0.1 ε units was calculated between the Velkerri/Wollogorang measurements of this study and those of Z. Li et al. (2021).

Instrumental mass fractionation was monitored using a standard-sample bracketing method, which involved a measurement of the primary SRM 3158 standard after two unknown sample measurements. The secondary ARISTAR standard was measured after seven unknown sample measurements to monitor instrumental drift and verify instrumental reproducibility.

Table 1 Authigenic Tl isotope ratios of the Velkerri and Wollogorang Formations. Values are from this study and Li et al., (2021).

Formation	Drill Hole	Depth Interval (m)	Mean $\varepsilon^{205}Tl$	2SD	n	$\varepsilon^{205}Tl$ (Li et al., 2021)	2SD	Deviation
Velkerri	Urapunga-4	136.98 - 137.05	-2.2	0.2	4	-2.0	0.3	-0.2
		137.19 - 137.26	-2.1	0.3	4	-3.1	0.1	1.0
		137.46 - 137.52	-1.7	0.1	3	-2.6	0.2	0.9
		325.71 - 325.78	-3.8	0.4	5	-3.2	0.3	-0.6
		326.20 - 325.28	-4.1	0.2	2	-3.2	0.4	-0.9
		326.42 - 326.48	-3.4	0.6	2	-3.1	0.5	-0.3
Wollogorang	Mount Young 2	74.27 - 74.29	-3.7	0.4	6	-4.5	0.3	0.8
		76.00 - 76.03	-4.6	1.1	5	-5.1	0.3	0.5

5.4.0 Enrichment Factors

Enrichment factors (EFs) are calculated to remove detrital influences from bulk trace element concentrations and to make easier comparisons between different rock units (Tribovillard et al., 2006). Trace metal (TM) concentrations (usually in μg/g) are normalized against bulk aluminum (Al) contents in weight percent (wt. %), and then normalized to a standard like the average composition of the upper continental crust (UCC). Enrichment factors are calculated as follows (Tribovillard et al., 2006):

$$EF_{TM} = (TM/Al)_{sample} \div (TM/Al)_{UCC}$$

If the EF > 1, then the sample is relatively more enriched in the TM compared to the UCC (Tribovillard et al., 2006). The following metal concentrations for average UCC are taken from Rudnick & Gao (2013) and are used to calculate TM EFs in this study: Al = 8.15 wt. %, Tl = 0.9 μg/g, Mo = 1.1 μg/g, U = 2.7 μg/g; Mn = 0.077 wt. %, and Ba = 624 μg/g.

6.0.0 Results

This section uses the following descriptive words to convey the strength of the correlation coefficient (r) between two geochemical parameters:

- Weak: $0 < r < 0.39$
- Moderate: $0.40 < r < 0.69$
- Strong: $0.70 < r < 0.85$
- Very strong: $0.86 < r < 1.0$

6.1.0 Mineralogy

The XRD data confirm the major minerals of the Kettle Point black shales in the GoC core are quartz and illite, which have a range of 28.0 - 56.1 wt.% (mean = 41.1 wt.%) and 17.9 - 39.1 wt.% (mean = 29.3 wt.%), respectively (Table 2). Quartz reaches a maximum of 56.1 wt.% at the base of Unit 2, and the maximum for illite is 39.1 wt.% in the middle of Unit 3. Minor mineralogy consists of chlorite (1.5 - 5.5 wt.%; mean = 3.6 wt.%), K-feldspar (1.4 - 4.2 wt.%; mean = 3.6 wt.%), kaolinite (0.4 - 3.3 wt.%; mean = 1.6 wt.%), pyrite (0.8 - 2.8 wt.%; mean = 1.3 wt.%), and marcasite (0.1 - 1.8 wt.%; mean = 0.6 wt.%). Minor amounts of gypsum (0.3 - 2.1 wt.%; mean = 1.1 wt.%) and jarosite-natrojarosite (0.5 - 2.2 wt.%; mean = 1.3 wt.%) are found in Units 1 to 3 but are absent in Unit 4. Three samples at the top of Unit 4 contain plagioclase (0.4 - 1.2 wt.%; mean = 0.7), and the top-most Unit 4 sample has minor amounts of dolomite (1.1 wt.%) and barite (0.4 wt.%).

Table 2 XRD mineralogy data. Values are in wt. %

Unit	Sample	Depth (m)	Quartz	Muscovite/Illite	K feldspar	Plagioclase	Chlorite	Kaolinite	Calcite	Dolomite
4	KPZ-1	28.0	28.0	25.9	1.4	0	3.7	3.3	0	1.1
	KPZ-7	34.4	41.8	30.7	3.6	1.2	3.2	1.5	0	0
	KPW3	41.2	34.1	32.2	2.0	0.6	2.6	2.3	0	0
	KPR6	48.6	39.1	26.3	2.4	0.4	2.5	1.6	0.3	0
	KPR14	56.8	44.3	29.2	3.0	0	3.6	1.6	0	0
	KPP11	61.6	38.2	33.7	2.6	0	4	2.1	0.8	0
3	KPP4	73.9	42.5	33.4	2.3	0	5.5	2.3	0.6	0
	KPP3	76.6	40.3	39.1	3.6	0	3.6	1.8	0	0
	KP20	87.7	39.6	34.6	3.4	0	4.6	1.9	0	0
2	KP18	92.0	38.9	35.3	2.5	0	4.3	1.3	0	0
	KP12	105.1	46.6	26.8	2.9	0	2.1	0.6	0	0
	KP7	114.2	56.1	17.9	3.2	0	1.5	0.4	0	0
1	KP5	120.2	46.7	25.5	4.2	0	3.9	0.5	0	0
	KP20	128.6	43.2	24.0	3.6	0	4.7	1.9	0	0
	KP1	135.3	36.8	24.3	4.0	0	3.6	0.9	0	0

Table 2 continued. Values in wt. %.

Unit	Sample	Depth (m)	Barite	Gypsum	Jarosite-Natrojarosite	Pyrite	Marcasite	Amorphous
4	KPZ-1	28.0	0.4	0	0	0.9	0.3	35
	KPZ-7	34.4	0	0	0	1.0	0.4	17
	KPW3	41.2	0	0	0	1.4	0.2	25
	KPR6	48.6	0	0	0	0.9	0.4	26
	KPR14	56.8	0	0	0	0.8	0.3	17
	KPP11	61.6	0	0	0	1.2	0.6	17
3	KPP4	73.9	0	0	0	0.8	0.4	12
	KPP3	76.6	0	0.7	1.3	1.1	0	9
	KP20	87.7	0	0.3	0	1.5	0.5	14
2	KP18	92.0	0	1.0	0	1.5	0.7	15
	KP12	105.1	0	1.1	1.5	2.2	0.7	16
	KP7	114.2	0	2.1	2.2	1.1	0.4	15
1	KP5	120.2	0	2.0	1.6	2.8	1.8	11
	KP20	128.6	0	1.2	0.9	1.8	0.9	18
	KP1	135.3	0	0.4	0.5	1.2	0.6	28

6.2.0 Elemental Concentrations and Covariations

The redox-sensitive TMs have similar stratigraphic trends of relatively consistent authigenic (2M HNO_3 leach) enrichments in Units 1 to 3, followed by increased enrichments in Unit 4 (Figure 10 a-e). Authigenic Tl (0.72 - 14 µg/g; mean = 4.3 µg/g), U (3.4 - 43 µg/g; mean = 17 µg/g), Mo (31 - 334 µg/g; mean = 99 µg/g), Re (10 - 331 ng/g; mean = 108 ng/g), and V (9.4 - 266 µg/g; mean = 86 µg/g) concentrations for the entire Kettle Point Formation display wide ranges because of the higher enrichments in Unit 4. For example, Tl concentrations in Units 1, 2, and 3 have ranges of 1.4 - 4.3 µg/g, 0.72 - 2.4 µg/g, and 1.7 - 2.7 µg/g, respectively, whereas Tl concentrations in Unit 4 are 3.2 - 14.3 µg/g. Authigenic Tl concentrations have a very strong, positive correlation with bulk rock Tl concentrations ($r = 0.99$; $p < 0.001$) (Figure 11).

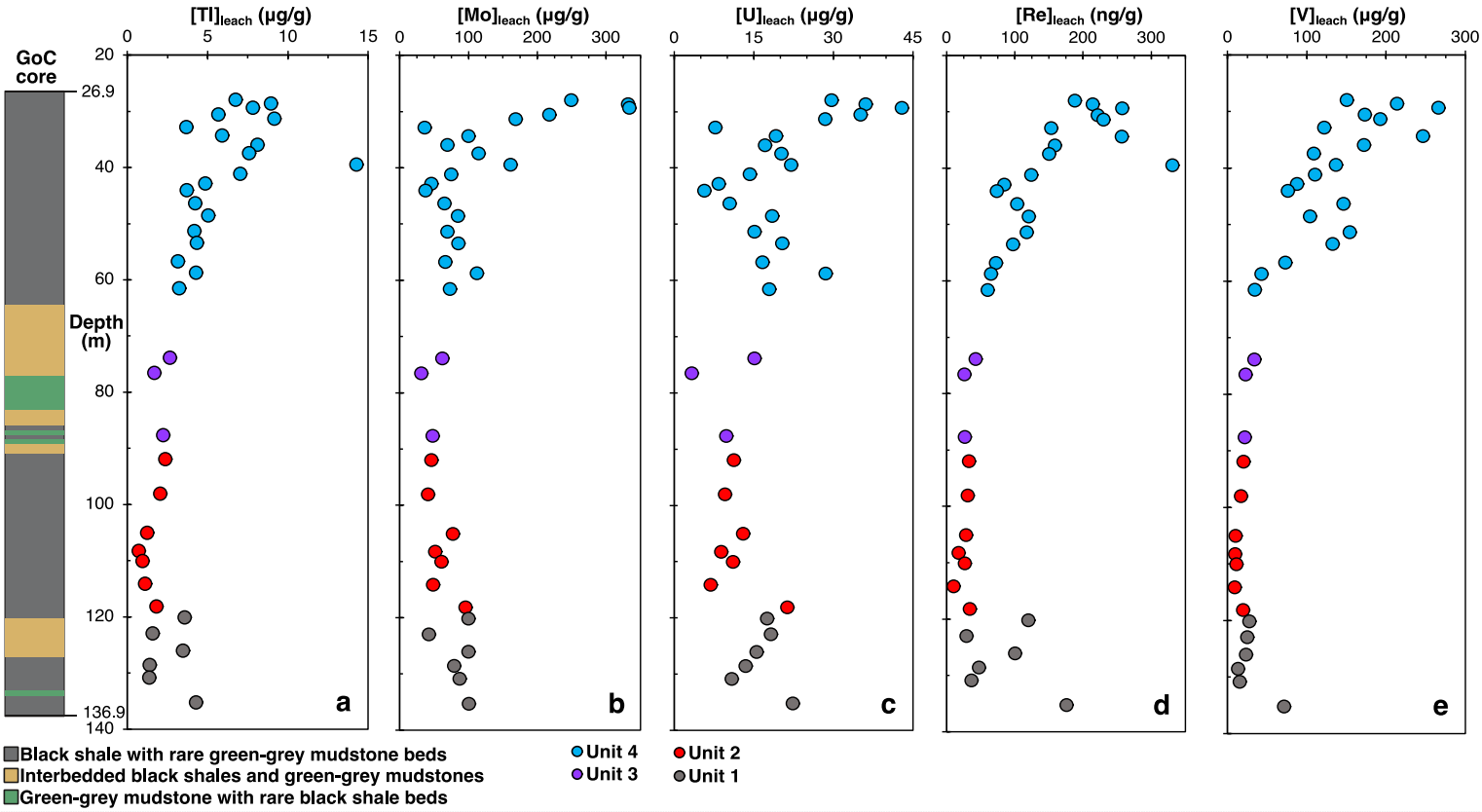

Figure 10 Stratigraphic trends of authigenic (leached) trace element concentrations. Trace elements are a) Tl, b) Mo, c) U, d) Re, and e) V.

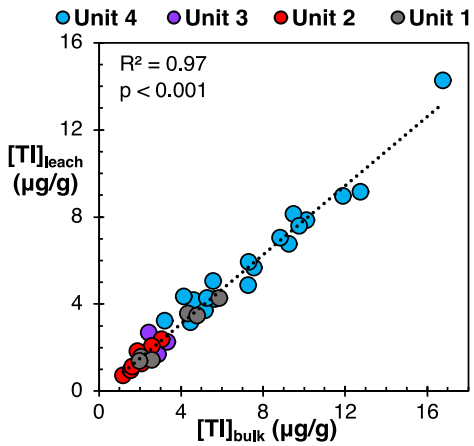

Figure 11 Cross plot between authigenic (leached) and bulk rock Tl concentrations.

Covariation graphs between authigenic Tl and other authigenic TM concentrations show that these enrichments reveal a close association between Tl and some TMs. Covariation plots of U and Mo versus Tl (Figures 12 a, b) show that they are moderately correlated, though still statistically significant for Mo ($r = 0.61$; $p < 0.001$) and U ($r = 0.59$; $p < 0.001$). The cross plots that compare Re and V to Tl (Figures 12 c,d) show Re ($r = 0.90$; $p < 0.001$) and V ($r = 0.76$; $p < 0.001$) enrichments closely follow that of Tl.

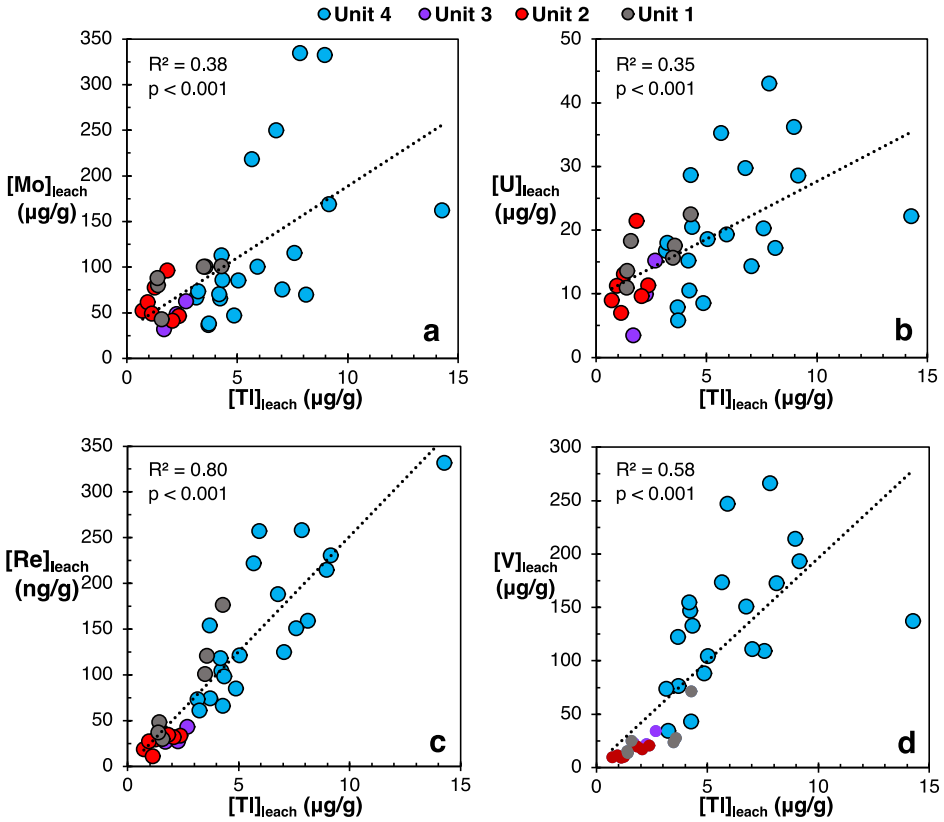

Figure 12 Cross plots between authigenic Tl and leached trace element concentrations. Trace elements are a) Mo, b) U, c) Re, and d) V.

Comparisons of authigenic Tl with major element contents from bulk rock and leached analyses show variable covariations. There is no correlation between authigenic Tl and bulk sulfur-pyrite (S_{pyrite}) ($r = 0.07$; $p > 0.05$) or total sulfur (TS) ($r = –0.26$; $p > 0.05$) (Figures 13 a,b). The positive correlations with bulk total organic carbon (TOC) ($r = 0.38$; $p > 0.01$) and bulk aluminum (Al) ($r = 0.39$; $p > 0.01$) are weak (Figures 13 c,d). Authigenic Tl does not show a correlation with leached Al ($r = 0.04$), Fe ($r = –0.21$), potassium (K) ($r = –0.13$), Mg ($r = 0.01$), Mn ($r = –0.15$), sodium (Na) ($r = –0.02$), and phosphorus (P) ($r = 0.25$; $p > 0.05$ for all) (Figures 14 a-g). Therefore, major elements that represent likely Tl host phases, such as illite (Martin et al., 2018; Wick et al., 2018, 2020), pyrite (Nielsen et al., 2011), and organic carbon (Watanabe & Takahashi, 2015), are not individually significant controls on Tl enrichment, and authigenic Tl is probably distributed amongst these hosts. Additionally, the weak correlation between authigenic Tl and bulk Al contents, as well as the very strong correlation between authigenic and bulk Tl concentrations (Figure 11), suggest that most of the Tl fraction is authigenic and not controlled by the detrital silicate fraction.

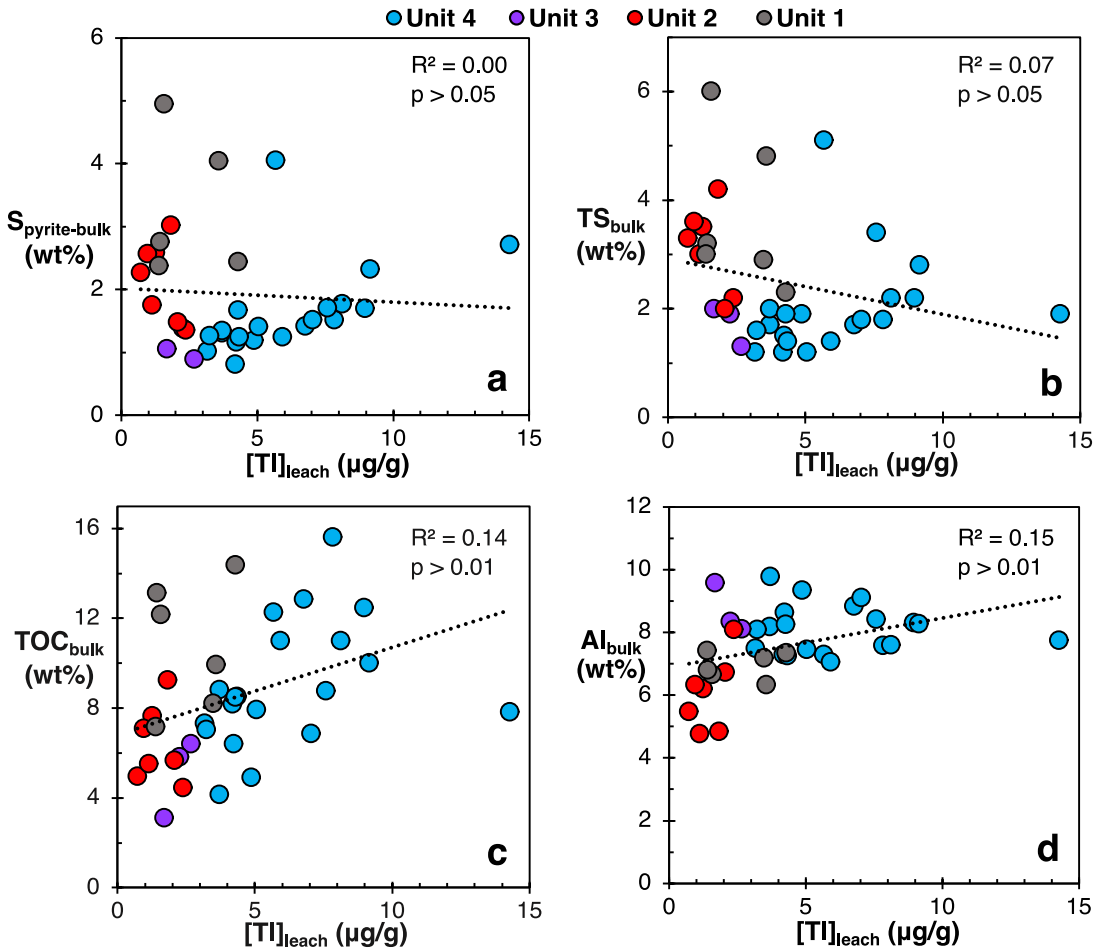

Figure 13 Cross plots between authigenic Tl concentrations and bulk rock major element contents. Major elements are a) S-pyrite, b) TS, c) TOC, and d) Al.

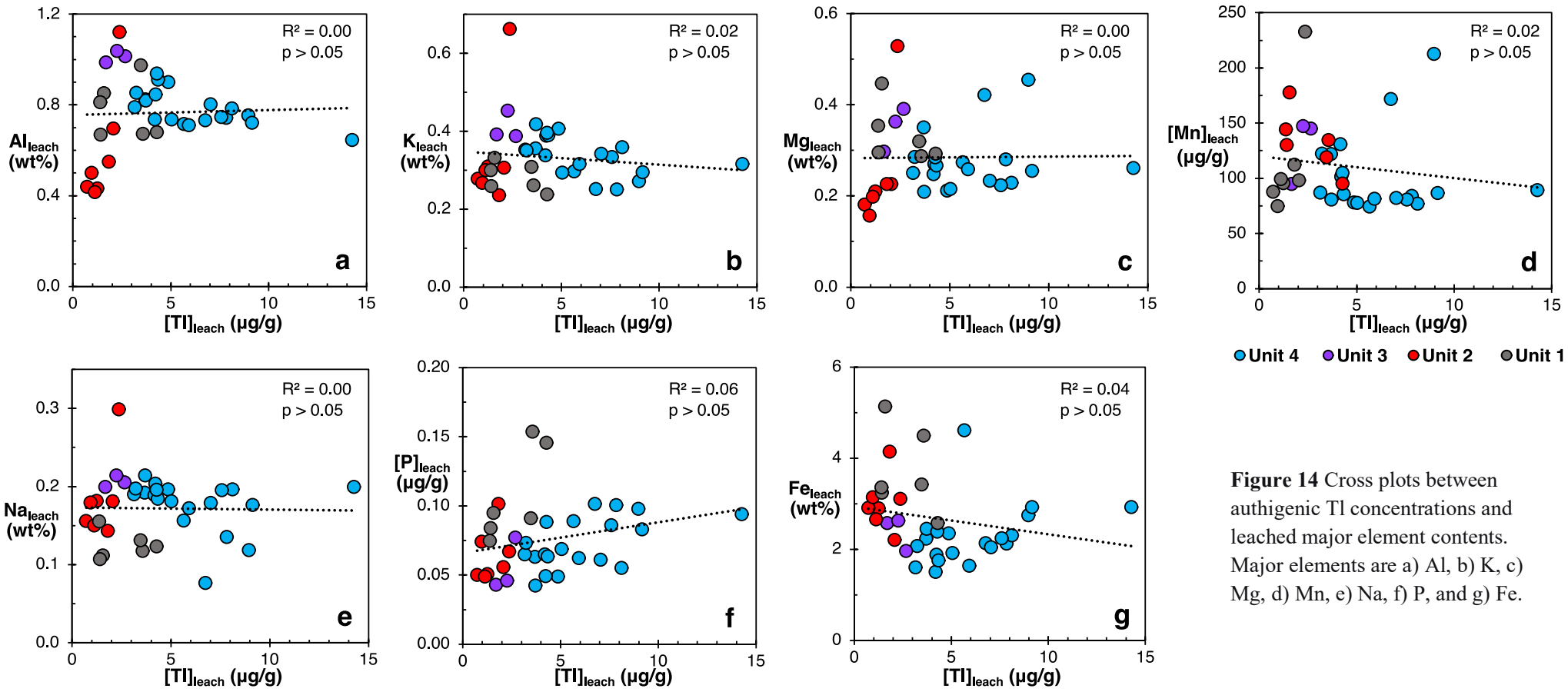

Figure 14 Cross plots between authigenic Tl concentrations and leached major element contents. Major elements are a) Al, b) K, c) Mg, d) Mn, e) Na, f) P, and g) Fe.

Stratigraphic trends of paleosalinity proxies exhibit decreasing trends, from marine to brackish values, when moving upsection (Figures 15 a-c). Cross plots of authigenic Tl and paleosalinity proxies are shown in Figures 16 a-c. Although the Sr/Ba paleosalinity proxy does not have a significant association with Tl concentrations ($r = -0.20$; $p > 0.05$) (Figure 16a), the B/Ga and TS/TOC proxies (Figure 16 b, c) have moderate, negative covariations with Tl concentrations ($r = -0.54$ and $r = -0.52$, respectively; $p = 0.001$ for both proxies).

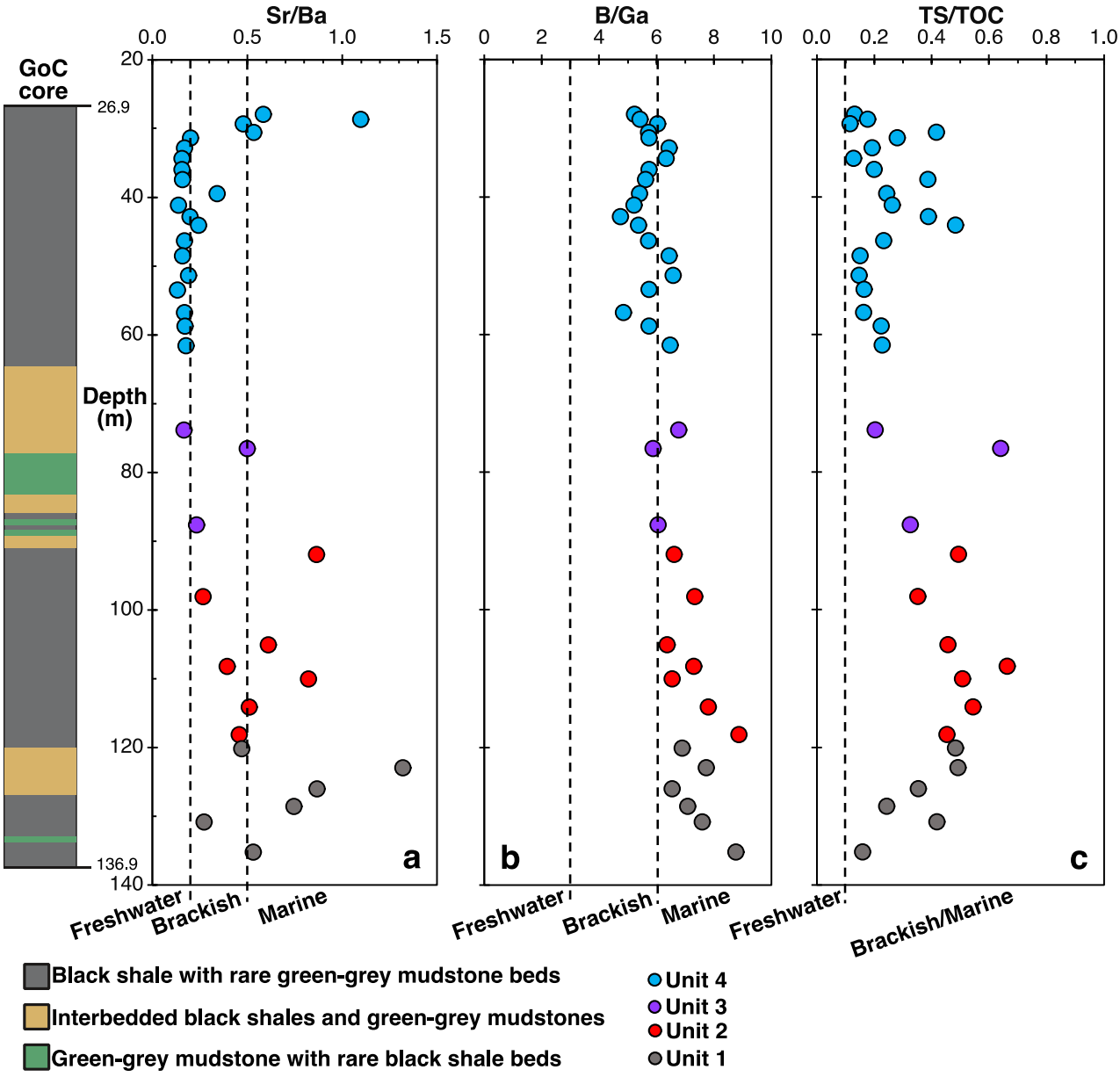

Figure 15 Stratigraphic trends of paleosalinity proxies. Proxies are a) Sr/Ba, b) B/Ga, and c) TS/TOC from bulk rock data.

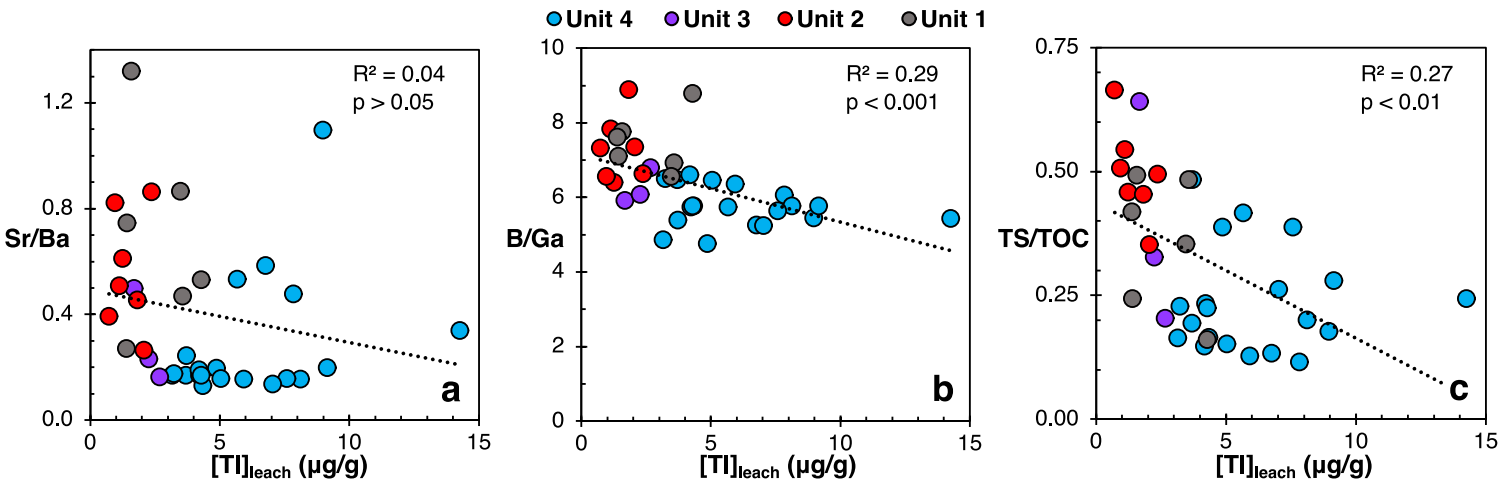

Figure 16 Cross plots between authigenic Tl concentrations and paleosalinity proxies. Proxies are a) Sr/Ba, b) B/Ga, and c) TS/TOC from bulk rock data.

6.3.0 Isotope Ratios and Covariations

Authigenic Tl isotope ratios have a general trend of less to more negative moving stratigraphically upsection and range from –7.2 to –2.0 ± 0.4 ε units (2SD; $\varepsilon^{205}Tl_{mean}$ = –4.5 ε units) (Figure 17a). Molybdenum isotope ratios (Figure 17b) also trend to more negative values moving upsection and range between 0.68 and 2.0 ± 0.11‰ (2SD; $\delta^{98}Mo_{mean}$ = 1.1‰). Uranium isotope ratios (Figure 17c) trend opposite to the other proxies, from more to less negative, and range between –0.29 and 0.60 ± 0.08‰ (2SD; $\delta^{238}U_{mean}$ = 0.23‰). Organic geochemical indicators from bulk rock analysis include $\delta^{13}C$ values (Figure 17d) that have a small range from –30.6 to –29.1‰ ($\delta^{13}C_{mean}$ = –29.8‰), and TOC contents (Figure 17e) that range from 3.1 to 14 wt.% (TOC_{mean} = 8.5 wt.%).

A strong negative correlation ($r = –0.79$; $p < 0.01$) between authigenic Tl concentrations and Tl isotope ratios (Figure 18a) show that samples with lower concentrations have higher isotope ratios, and that samples with higher concentrations have lower isotope ratios. Similar strong and very strong negative covariations between Tl isotope ratios and authigenic Re ($r = –0.79$; $p < 0.01$) and V ($r = –0.87$; $p < 0.01$) concentrations (Figures 18 d,e) reaffirms the close relationships between these metals. Molybdenum ($r = –0.47$; $p < 0.01$) and U concentrations ($r = –0.46$; $p < 0.01$) also display negative covariations with Tl isotope values (Figures 18 b, c), albeit not as strongly as for Re and V, which further supports a minor decoupling between the Tl enrichment pathways in sediments and those of Mo and U.

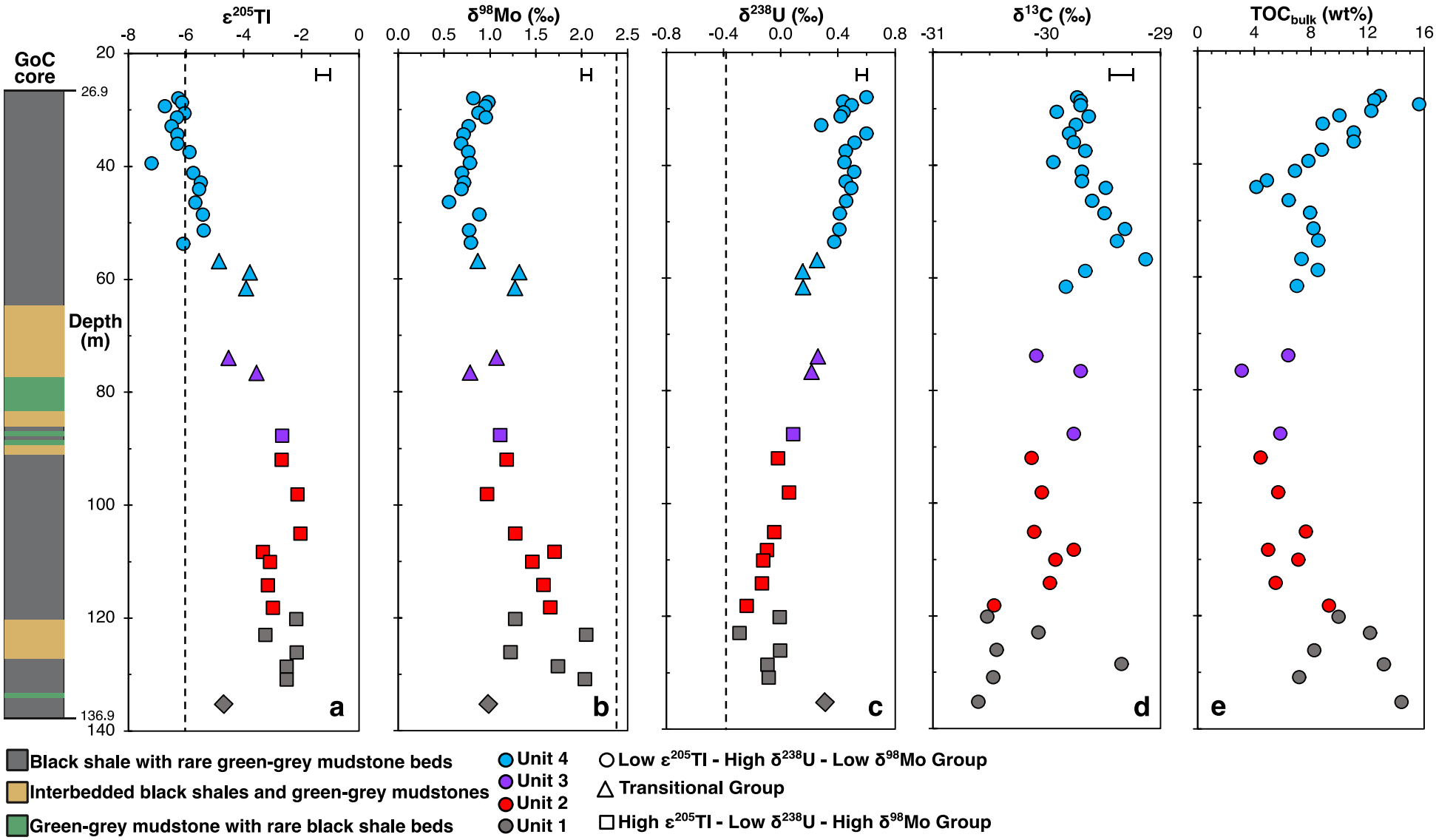

Figure 17 Stratigraphic trends of authigenic paleoredox isotope proxies and organic geochemical indicators. Paleoredox proxies are a) Tl, b) Mo, and c) U isotope ratios and bulk rock organic geochemical indicators are d) C isotope ratios and e) TOC contents. Dashed lines are modern seawater isotope compositions of Tl (-6 ε units), Mo (2.3‰), and U (-0.39‰). The 2SD of Tl (0.4 ε units), Mo (0.11‰), U (0.8‰), and C (0.2‰) isotope ratios represented by error bars.

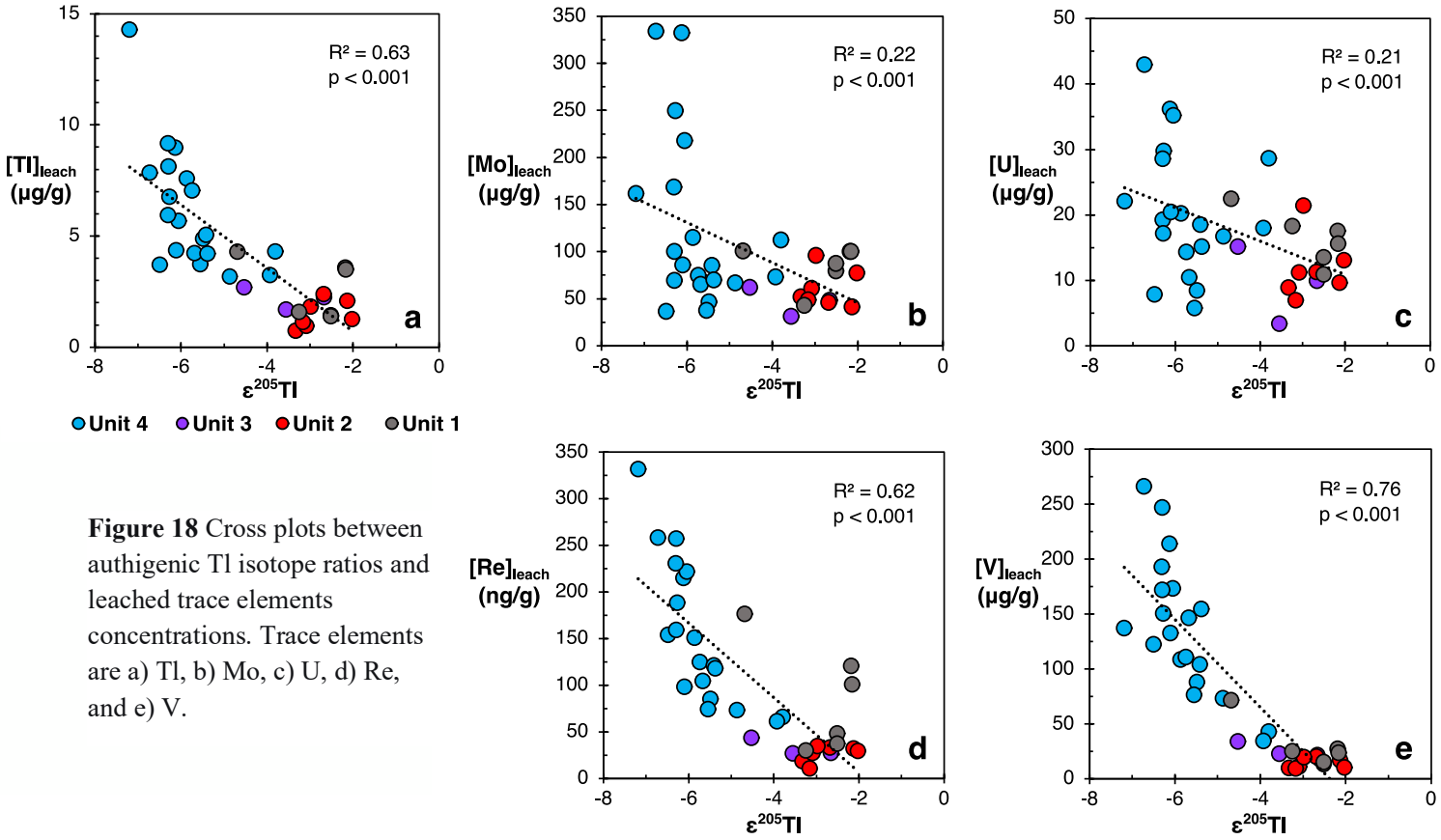

Figure 18 Cross plots between authigenic Tl isotope ratios and leached trace elements concentrations. Trace elements are a) Tl, b) Mo, c) U, d) Re, and e) V.

When comparing the authigenic Tl, Mo, and U isotope ratios, Tl exhibits strong covariation with both U and Mo. Specifically, Tl isotope ratios have a strong positive correlation with authigenic Mo isotope ratios ($r = 0.71$; $p < 0.01$) but a very strong negative correlation with authigenic U isotope ratios ($r = –0.89$; $p < 0.01$) (Figures 19 a, b). Both Tl - Mo isotope and Tl - U isotope graphs show three distinct sample groupings; these groupings are more apparent between U and Tl. The groups are described as a) the high Tl – low U – high Mo isotope ratio group ($\varepsilon^{205}Tl_{mean} = –2.7 \pm 0.4$ 2SD, $n = 13$), b) the low Tl – high U – low Mo isotope ratio group ($\varepsilon^{205}Tl_{mean} = –6.1 \pm 0.6$ 2SD, $n = 17$), and c) the transitional group ($\varepsilon^{205}Tl_{mean} = –4.1 \pm 0.5$ 2SD, $n = 5$). The high Tl - low U - high Mo isotope ratio samples are exclusively found in Unit 4, whereas the low Tl - high U - low Mo isotope ratio group consists of samples from Units 1 to 3. The transitional group has samples from Unit 3 and lower Unit 4 and represents a transition between the other two groups with respect to isotope ratios. There is one Unit 1 sample (diamond symbol) that displays similar isotope ratios as those in the transition group but is temporally unrelated because it is found at the very bottom of the core, and therefore, is not considered a part of the transitional group nor the high Tl - low U - high Mo group.

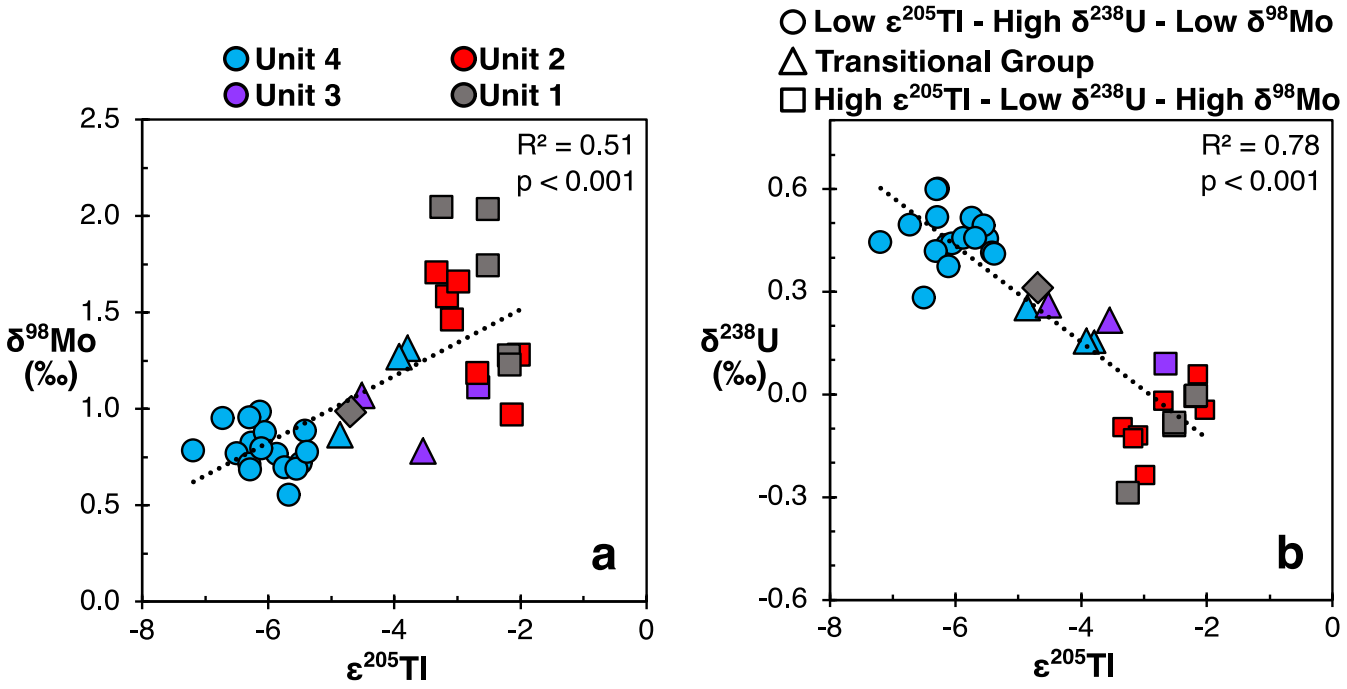

Figure 19 Cross plots between paleoredox proxies. Authigenic Tl isotope ratios (x-axis) compared to a) authigenic Mo isotope ratios and b) authigenic U isotope ratios (y-axis).

Like the covariation graphs involving Tl concentrations, there are variable associations between authigenic Tl isotope ratios and whole-rock major element contents (Figures 20 a-f). There is no statistical significance to the correlations with S_{pyrite} ($r = 0.30$; $p > 0.05$) and TOC contents ($r = –0.32$; $p > 0.05$). Although the negative correlation with bulk Al ($r = –0.33$; $p < 0.05$) and positive correlation with TS ($r = 0.42$; $p < 0.05$) are statistically significant, their relationship with Tl isotope ratios is weak and thus are not a strong control on Tl isotope expression. Both bulk ($r = 0.25$) and leached Mn ($r = 0.28$; $p > 0.05$ for both) also have statistically insignificant correlations with Tl isotope ratios.

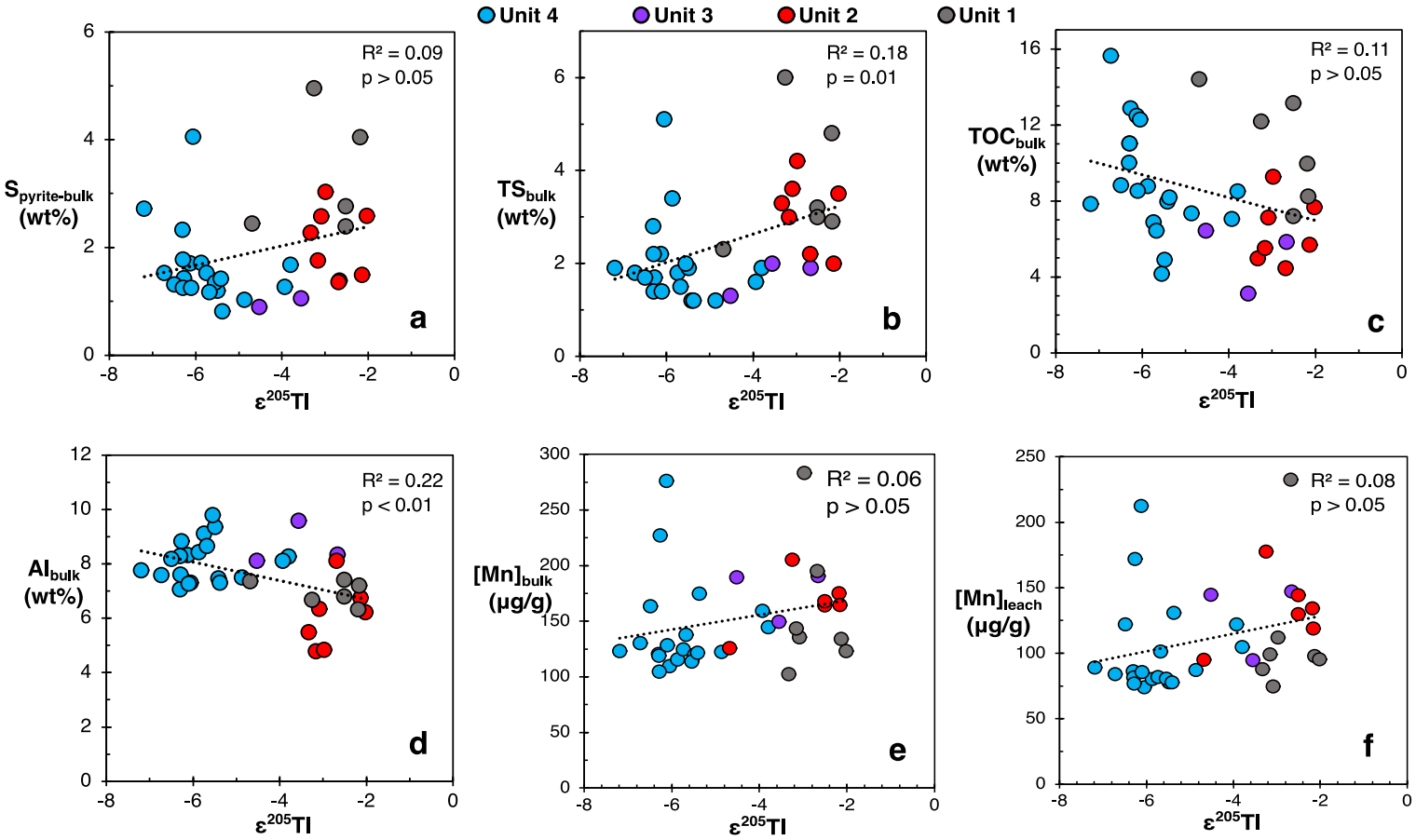

Figure 20 Cross plots between authigenic Tl isotope ratios and bulk rock major elements. Major elements are a) S-pyrite, b) TS, c) TOC, d) Al e) Mn contents and f) leached Mn concentrations.

The cross plots between paleosalinity proxies and paleoredox proxies are shown in Figures 21 a-i. Covariations between paleosalinity and Tl isotope ratios (Figures 21 a-c) are all positive but are moderately correlated with TS/TOC ($r = 0.60$; $p < 0.05$) and B/Ga ($r = 0.57$; $p < 0.001$), and weakly correlated with Sr/Ba ($r = 0.38$; $p < 0.01$). The cross plots between the paleosalinity proxies and authigenic Mo isotope ratios (Figures 21 d-f) and authigenic U isotope ratios (Figures 21 g-i) display stronger relationships than the covariations with Tl isotope ratios. Molybdenum isotopes exhibit moderate, positive correlations with Sr/Ba ($r = 0.51$), TS/TOC ($r = 0.41$; $p < 0.01$ for both), and B/Ga ($r = 0.68$; $p < 0.001$). Uranium isotopes have a moderate, negative correlation with B/Ga ($r = –0.69$) TS/TOC ($r = –0.62$; $p < 0.001$ for both), and Sr/Ba ($r = –0.49$; $p < 0.01$).

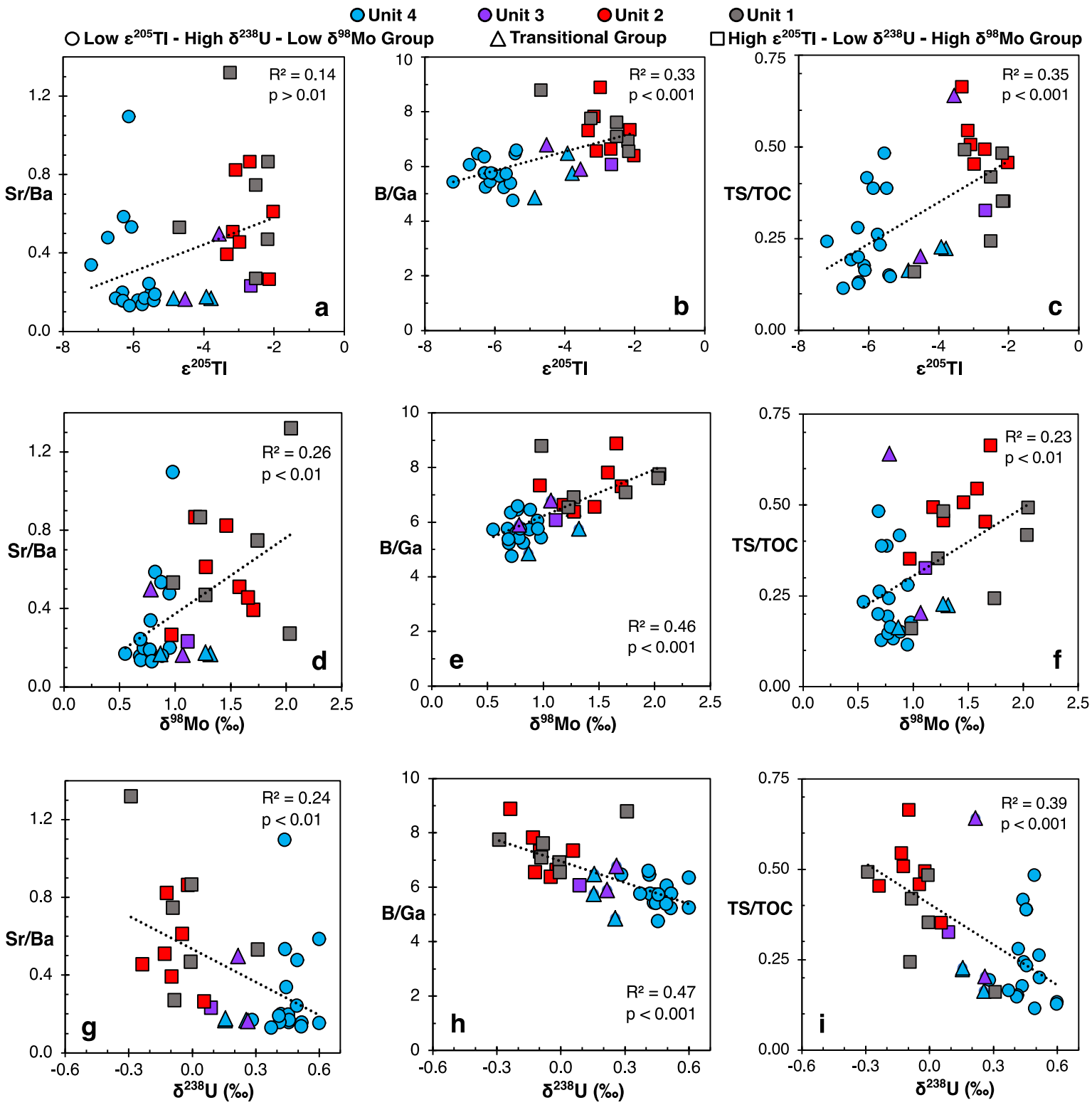

Figure 21 Cross plots between paleoredox and paleosalinity proxies. Paleoredox isotope proxies (Tl, Mo, U) are along x-axis and paleosalinity proxies (Sr/Ba, B/Ga, TS/TOC) are along the y-axis.

7.0.0 Discussion

7.1.0 Mineralogy Interpretations

7.1.1 Sulfates and Sulfides

The presence or absence of certain minerals can provide insight to the formation's depositional environment, and the sulfide and sulfate contents are of particular interest. The stratigraphic trends of all mineral populations decrease when moving up the GoC core (Figure 22). The presence of jarosite, marcasite, and gypsum in Units 1 to 3, and their lower contents in Unit 4, aligns with previous interpretations by Kendall et al. (2020). The sulfates and marcasite form during the aqueous oxidation of pyrite, which requires free dissolved oxygen to occur (Q. Li et al., 2020; X. Liu et al., 2018; Schieber, 2011). Units 1 and 2 were interpreted as more strongly euxinic than Units 3 and 4 (Kendall et al., 2020), thereby more aqueous sulfide was available to form pyrite in basin sediments during deposition of black shales in Units 1 and 2 compared to Units 3 and 4. The requirement of free dissolved oxygen for pyrite oxidation indicates the Chatham Sag experienced deep-water reoxygenation that was frequent enough to induce pyrite oxidation and thus sulfate and marcasite precipitation, but infrequent and transient enough for strong bottom-water euxinia to occur during Units 1 and 2. The weaker euxinic conditions in Unit 4 produced lower pyrite contents and, consequently, lower sulfate and marcasite precipitation during reoxygenation events.

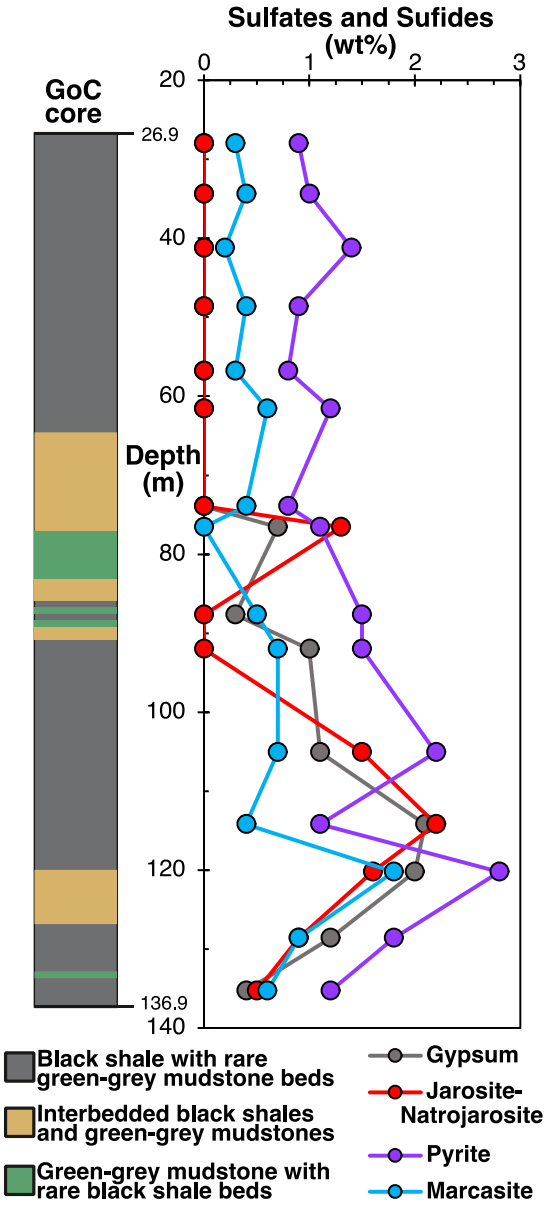

Figure 22 Stratigraphic trends of sulfate and sulfide contents.

7.1.2 Clays

The proportions of clay minerals can record changes in weathering and climate conditions. For example, higher Weathering Index (WI: kaolinite/(illite+chlorite)) values indicate weathering in warm, humid climates and lower values reflect weathering in dry, cold climates (Duchamp-Alphonse et al.,

2011). However, caution is taken when interpreting the clay fraction of the Kettle Point black shales. Scanning electron microscope (SEM) data from a previous mineralogical study found illite morphologies of both detrital (i.e. sourced from river inputs) and diagenetic (i.e. formed in-situ from diagenetic illitization of smectite) sources (Delitala, 1984). Therefore, reconstruction of the initial depositional environment would not be accurate without detailed stratigraphic positions of each morphology and additional XRD data, like smectite and layered illite/smectite contents. Although clay assemblages would be an asset, this study will not be applying these proxies to the paleoenvironmental reconstruction.

7.2.0 Decision Tree

The authigenic Tl isotope ratios of the Kettle Point black shales need to reflect the overlying seawater Tl isotope ratios to accurately interpret the depositional paleoenvironment. A simplified decision tree (Figure 23) developed by Wang et al. (2022) utilizes Mn, Ba, and U EFs of modern organic-rich sediments to evaluate if they record the overlying seawater Tl isotope ratio (i.e. quantitative sedimentary Tl enrichment), or if the Tl isotopes record an ambiguous signal. Quantitative enrichment of Tl relies on reducing sediment porewaters, which were observed to quickly reduce and remove aqueous Tl from seawater (Ahrens et al., 2021). Even if bottom-waters are not completely anoxic, porewaters can become reducing under high productivity and/or sedimentation rates that are accompanied by shallow

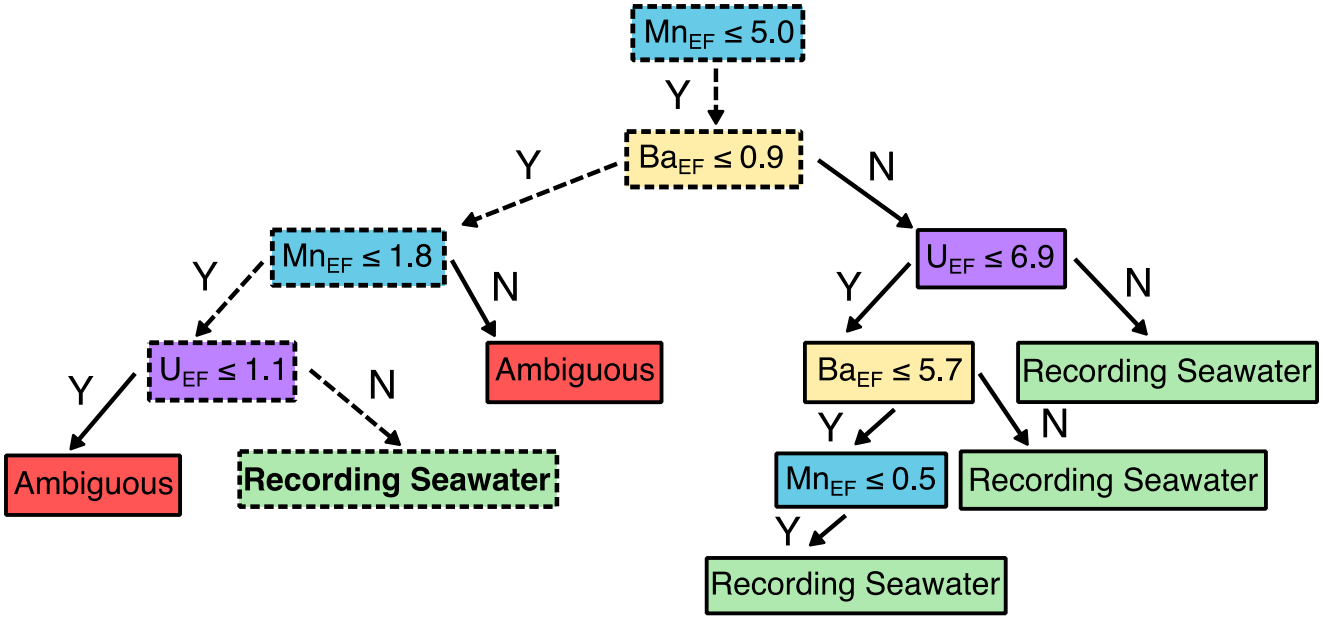

Figure 23 Simplified decision tree modified from Wang et al. (2022). Dashed arrows and boxes represent branches and EF thresholds for the Kettle Point black shales. Y = yes; N = no.

oxygen diffusion into surface sediments, such as in oxygen minimum zones (OMZs) of modern ocean (Y. Wang et al., 2022). Decision tree pathways that result in ambiguous signals do not solely rely on the reductive porewater mechanism and may or may not quantitatively record seawater Tl compositions (Y. Wang et al., 2022). Ambiguous signals are caused by the predominance of other sedimentary Tl enrichment mechanisms, such as reducing bottom-water conditions caused by microbial degradation of organic matter that are indicated by $U_{EF} < 7$ and high TOC contents (>1 wt.%) (Y. Wang et al., 2022).

Assumptions are made when applying the decision tree to ancient sediments such as black shales. It is assumed that the Late Devonian ocean reservoir of Mn, Ba, and U is relatively similar to that of the modern ocean and that factors contributing to metal transport to the ocean, such as rates of oxidative weathering, are also similar to that of today (Wang et al., 2022). According to Scott et al. (2008), modern oxidative weathering rates were established roughly 550 Mya, which is ~180 million years before deposition of the Kettle Point Formation. Secondly, it is assumed that the oxygenation levels of the ancient open ocean were like those of modern seawater. For this case study, the Late Devonian ocean may have been more reducing than the modern ocean (Kendall et al., 2020; Racki, 2005; D. A. White et al., 2018), and the U EF thresholds would be lower in response to the decreased oceanic reservoir of aqueous U. However, because the U EFs of the Kettle Point Formation are well above the modern U thresholds, the black shales should still have quantitatively captured the seawater Tl isotope composition. By applying the EFs of Mn (0.12 - 0.62), Ba (0.12 - 0.88), and U (4 - 23) (Appendix C) of the Kettle Point Formation, the decision tree confirms that the black shales recorded the overlying seawater ε^{205}Tl and allows for the following interpretations.

7.3.0 Possible Interpretations

7.3.1 Local Fe-Mn Oxyhydroxide Shuttle

The first possible interpretation considers the influence of Fe-Mn oxyhydroxides as a key mechanism for sedimentary TM enrichment and Tl isotope expression. Although Mo isotope ratios are low enough in Unit 4 to invoke particulate shuttling, an inverse covariation between the Tl and Mo isotope systems should also be apparent (Owens et al., 2017). Since that is not observed, and Tl isotope ratios have a moderate positive correlation with Mo isotopes (Figure 19a), both vertical and lateral Fe-Mn shuttling is rejected as possible enrichment mechanisms for TMs.

7.3.2 Regional Redox Conditions

Like recent sedimentary Tl isotope studies, redox interpretations assume that the isotopic composition of different Tl sources (e.g. rivers and aerosols) are similar to each other throughout black shale deposition (Owens, 2019). Another assumption is that the Tl flux into the hydrothermal crust alteration sink also remains the same because the rate of global seafloor spreading does not change significantly over the geologically short periods of black shale deposition (Nielsen et al., 2009; Owens, 2019). Therefore, a change in the Tl isotope ratios is most likely caused by a change in redox-associated sinks, primarily an expansion or contraction of the oxic sediment sink (Owens, 2019). While other studies have made these assumptions on a global scale, it was determined that the redox shift within the Chatham Sag must be on a smaller scale to accommodate the inverse Mo and U isotope covariation caused by a local redox change from strongly to weakly euxinic (Kendall et al., 2020). Thus, a regional redox shift is a possible cause for the change in Tl isotope ratios.

This interpretation relies on the change in Mn-oxide precipitation within the Chatham Sag. The high Tl - low U - high Mo isotope ratio group represent relatively higher bottom-water H_2S concentrations from Units 1 to lower Unit 3, when low dissolved oxygen levels could have also been extensive across the entire Chatham Sag. This resulted in low Mn-oxide precipitation on a regional scale, which allowed the heavier Tl-205 isotope to be sequestered by basin sediments rather than adsorbed onto Mn-oxide particulates in oxic surface waters and buried in oxic sediments along shallow basin margins. Additionally, black shale deposition during Units 1 to lower Unit 3 is characterized by infrequent replenishments of seawater to the sub-basin, which allowed the Chatham Sag to maintain a low TM reservoir instead of becoming depleted and to sequester heavier Tl-205 into basin sediments. The transition period from upper Unit 3 to lower Unit 4, represented by the transitional group, is when Mn-oxide precipitation started to increase and resulted in increased Tl-205 isotope burial into oxic sediments. The frequency of seawater replenishments also increased, which supplied both TMs and free dissolved oxygen to the Chatham Sag. The frequency of transient reoxygenation events reached its peak during the weakly euxinic period in the middle of Unit 4, which is represented by the low Tl - high U - low Mo isotope ratio group. Trace metal enrichments remained high while the precipitation and burial of Mn-oxides was further enhanced and continued to remove Tl-205 isotopes from the water column. This caused the water column to become more enriched in lighter Tl-203 and sedimentary Tl isotope ratios of the deep basin to shift to more negative (i.e. lighter) values, which are captured at the top of the GoC core.

The variation of Mn-oxide precipitation is not evident in the covariation between Tl isotope ratios and bulk (Figure 20e) and leached Mn (Figure 20f). It could be argued that the location of the GoC core within the Chatham Sag was responsible for these weak correlations. The fluctuating redox conditions, which are evident by the interbedding of green-grey mudstones and black shales, means that this locality was exposed to frequent anoxic conditions. This would prevent burial of Mn-oxides due to their reductive dissolution when the redoxcline was at or above the sediment water interface. Studies of the stratigraphically equivalent New Albany Shale and Antrim Shale hypothesize that basin shelves could have been vertically positioned above the chemocline and exposed to predominantly oxic conditions (Brown & Kenig, 2004; Cluff, 1980). The shelf is where Mn-oxides could successfully capture and preferentially bury Tl-205 in oxic sediments, whereas the deeper and commonly anoxic portions of the Chatham Sag did not have significant Mn-oxide burial, including at the GoC locality.

However, if Mn-oxides were controlling sedimentary TM isotope expression, the weakly euxinic period in upper Unit 4 should also result in adsorption of lighter Mo isotopes onto Mn-oxides and subsequent burial in oxic shelf sediments. This would leave heavier Mo-98 in the water column and result in more positive (i.e. heavier) sedimentary Mo isotope ratios recorded in upper Unit 4. Molybdenum isotope ratios would increase from open ocean values ($\delta^{98}Mo = 2.3‰$) in Units 1 - lower Unit 3 to higher, more positive Mo isotope ratios in upper Unit 4 and should create an inverse correlation with Tl isotope ratios. Like the Fe-Mn shuttle interpretation, this regional redox interpretation is rejected because the positive rather than negative correlation is observed between the Tl and Mo isotope ratios (Figure 19a).

7.3.3 Regional Hydrographic Conditions

Interpretations should also consider the degree of basin restriction to the open ocean as another control on trace metal accumulation. Kendall et al. (2020) previously interpreted the Mo and U EF relationship to reflect the Chatham Sag's constant semi-restriction, and that local redox variation was the dominant control on Mo and U isotope ratios. The addition of Tl isotopes to the Mo-U systems reveals basin restriction as an important control on Tl isotope expression. The strongly euxinic samples from Unit 1 to lower Unit 3 have a mean $\varepsilon^{205}Tl = –2.7 \pm 0.4$ 2SD, and is similar to the Tl isotope ratio of the modern Black Sea oxic surface water ($\varepsilon^{205}Tl = –2.2 \pm 0.3$ 2SD; Owens et al., 2017). This reflects the Black Sea's strong restriction to the modern ocean and the dominant Tl input from freshwater riverine sources associated with continental runoff ($\varepsilon^{205}Tl = –2.5 \pm 1.0$ 2SD; Nielsen et al., 2005). Therefore, the

Chatham Sag could have been more restricted to the ancient ocean during the deposition of Unit 1 to lower Unit 3, and the Tl isotope ratios fingerprint the input of river water runoff from the Laurentia craton. Conversely, the weakly euxinic samples of upper Unit 4 have a mean $\varepsilon^{205}Tl = -6.1 \pm 0.6$, which is close to the Tl isotope ratio of the modern ocean ($\varepsilon^{205}Tl = -6.0 \pm 0.3$ 2SD; Owens et al., 2017). These samples represent a less restricted basin that had frequent replenishments of seawater from the ancient ocean. The change in basin restriction aligns with the change in local redox conditions, from strongly restricted that develops strong bottom-water euxinia to weakly restricted with weaker bottom-water euxinia, as observed in modern marine basins.

7.4.0 Paleosalinity Proxies and Discrepancies with Possible Interpretations

7.4.1 Trace Metal Enrichments

The addition of paleosalinity proxies from bulk rock analysis creates inconsistences with the Tl - U - Mo paleoredox proxies. Paleosalinity proxies (Sr/Ba, B/Ga, and TS/TOC; Figures 15 a-c) show an overall decreasing trend when moving up the GoC core, which indicates a shift from marine waters in Unit 1 to brackish waters in Unit 4 (Kendall et al., 2020). This is initially perplexing when also considering the increased TM accumulations in Unit 4, because modern river water has significantly lower concentrations of TMs compared to ocean water. More specifically, the modern riverine dissolved Tl concentration is $1 - 7 \times 10^{-3}$ ng/g (Nielsen et al., 2005) and the modern ocean dissolved Tl concentration is 13 ng/g (Owens, 2019). Therefore, the increased TM concentrations in the upper Unit 4 should not be possible solely by an increased flux of river water, which instead would decrease the Chatham Sag's TM reservoir and result in lower sedimentary TM enrichments. Consequently, there must have been significant replenishment of ocean water to the Chatham Sag during the deposition of Unit 4 that resulted in higher TM enrichments.

7.4.2. Modern Isotope Signals

The positive correlation between the B/Ga and TS/TOC proxies and the Tl (Figures 21 b,c) and Mo (Figures 21 h,i) isotope ratios and the negative correlation with U isotope ratios (Figure 21 e,f) suggest a change between the paleoredox and paleosalinity proxies that was moderately coupled. However, discrepancies arise when comparing paleosalinity to modern Tl isotope signatures. From Unit 1 to lower Unit 3, the paleosalinity proxies suggest more marine inputs and although U and Mo isotope ratios are close to modern ocean values ($\delta^{238}U = -0.39$ ‰ and $\delta^{98}Mo = 2.3$‰), the Tl isotope ratios are

closer to modern riverine Tl isotope values. In upper Unit 4, the more brackish paleosalinity reflects an increase in freshwater from riverine sources, but the Tl isotope ratios reflect those of the modern ocean and the U isotope ratios are higher than the upper limit ratio of modern river inputs ($\delta^{238}U = 0.06‰$; Andersen et al., 2017). Although Mo isotope ratios in upper Unit 4 are similar to average modern riverine values ($\delta^{98}Mo = 0.3 - 0.7‰$; Archer & Vance, 2008; King & Pett-Ridge, 2018), Kendall et al. (2020) noted that the amount of river water needed to shift the sedimentary Mo isotopic composition to a riverine signature is excessively high and unrealistic.

7.4.3. Regional Sea-Level and Hydrography

The last issue between the paleosalinity and the Tl isotope ratios is the role of regional sea-level and basin restriction to the ancient ocean. In Unit 1 to lower Unit 3, the strongly euxinic conditions would traditionally imply a relatively lower sea-level that resulted in a more restricted basin, which caused Tl isotope ratios to reflect those of modern river sources. This interpretation also assumes that modern oxidative weathering rates and the modern upper continental crust composition are similar to those during the Late Devonian (Gaschnig et al., 2016; Scott et al., 2008). However, the marine paleosalinity suggests that the Chatham Sag was substantially connected to the open ocean, and consequently, the regional sea-level was relatively higher than basin sills to allow for watermass exchange and the predominance of marine salinity in the deep basin of the Chatham Sag. In upper Unit 4, the weakly euxinic conditions suggest a higher sea-level and a less restricted Chatham Sag that resulted in sedimentary Tl isotope ratios that reflect open ocean sources, which would not be significantly different from the modern open ocean value. The paleosalinity proxies conflict with this interpretation, because the brackish values indicate an increase in freshwater inputs and a decrease of oceanic inputs to the sub-basin that could be attributed to increased basin restriction.

7.5.0 Preferred Interpretation

An interpretation that encompasses both paleosalinity proxies and the Tl - Mo - U isotope systems, and avoids the above-mentioned discrepancies, requires regional changes in water sources and basin restriction to the open ocean. During deposition of the high Tl - low U - high Mo isotope ratio group in Units 1 to lower Unit 3, the Chatham Sag's restriction to the open ocean was relatively strong but was still connected enough to promote high salinity and maintain low sedimentary TM enrichments in the deep basin. The U and Mo isotope ratios reflect the locally near-quantitative drawdown of U and

Mo, which was induced by infrequent oceanic inputs and high bottom-water sulfide concentrations. The Tl isotope ratios represent the dominant river inputs in response to the stronger basin restriction. In contrast, the low Tl - high U - low Mo isotope ratio group of the upper Unit 4 represents increased freshwater inputs and concomitant decreased basin restriction. The increased freshwater shifted the salinity to more brackish conditions and, in combination with more frequent oceanic inputs from the improved connectivity with the open ocean, also diluted dissolved sulfide concentrations of the deeper bottom-waters in the Chatham Sag. The U and Mo isotope ratios represent the locally non-quantitative removal of U and Mo to weakly euxinic basin sediments, while the Tl isotope ratios reflect the decrease in basin restriction to the open ocean. The Chatham Sag must have been hydrologically well-connected to the ancient ocean to record the high enrichment of TMs and the open ocean Tl isotope signature of upper Unit 4, and there must have been an increased influx from freshwater sources to allow for a concurrent change to brackish salinity near the sediment-water interface within the deep basin.

The benefit of analyzing both Tl isotopes and the U-Mo isotope systems is the difference in residence times, which allows for inference of both short- and long-term variations in seawater compositions. The shorter residence time of Tl (~20 kyr, Owens et al., 2017) allows Tl isotopes to be more sensitive to short-term changes, such as changes in TM sources to the overlying water column (Owens, 2019). In contrast, U (~450 kyr, Dunk et al., 2002) and Mo (~440 kyr, Miller et al., 2011) isotope systems respond to long-term redox variations in the deep basin (Brüske et al., 2020).

The transitional sample group of the upper Unit 3 - lower Unit 4 represents the period when changes in local bottom-water redox, basin restriction, and salinity commenced. However, the weak to moderate correlations between the paleoredox and paleosalinity proxies (Figures 21 a-i) display decoupling between the salinity changes and the variations in basin restriction and local redox conditions. This decoupling is probably caused by several environmental factors affecting the Kettle Point Formation's depositional environment. Therefore, the following subsections consider possible mechanisms that shifted paleoenvironmental conditions in the Chatham Sag and the surrounding eastern NAS.

7.5.1 Local Uplift Mechanism for Decreased Basin Restriction

The decreased basin restriction may have been caused solely by the Late Famennian eustatic transgression observed across the eastern NAS (Figure 2) or with the assistance of decreased accommodation space of the basin, such as the tectonic mechanisms hypothesized by Bingham-

Koslowski (2015) in Section 2.3.2 (Figure 24a). The local uplift could have facilitated a better hydrological connection to the other basins by raising the floor of the sub-basin and decreasing its accommodation space. However, tectonic influences likely affect sedimentary deposition cycles on a long timescale that ranges 10^6 - 10^8 years (i.e. 2^{nd} - 3^{rd} order) (Ettensohn et al., 2019 and references therein). Shorter cycles of 10^4 - 10^5 years (i.e. 4^{th} - 6^{th} order) are more likely to reflect high-frequency eustatic or climatic changes (Ettensohn et al., 2019 and references), which is in better agreement with the geologically short interval of the transitional period. A localized tectonic mechanism is not completely ruled out, but it is difficult to support with one drill core. The local structure should have only affected the southwestern margin of the roughly 80 km-wide Chatham Sag, therefore, analysing Tl - Mo - U isotope compositions of a core transect that traversed across the sub-basin, from the southwest to the northeast margin, could help determine if the hypothetical uplift affected the degree of restriction within other areas. Although a local tectonic mechanism may explain a decrease in basin restriction near the GoC core, it would not contribute to the shift in paleosalinity.

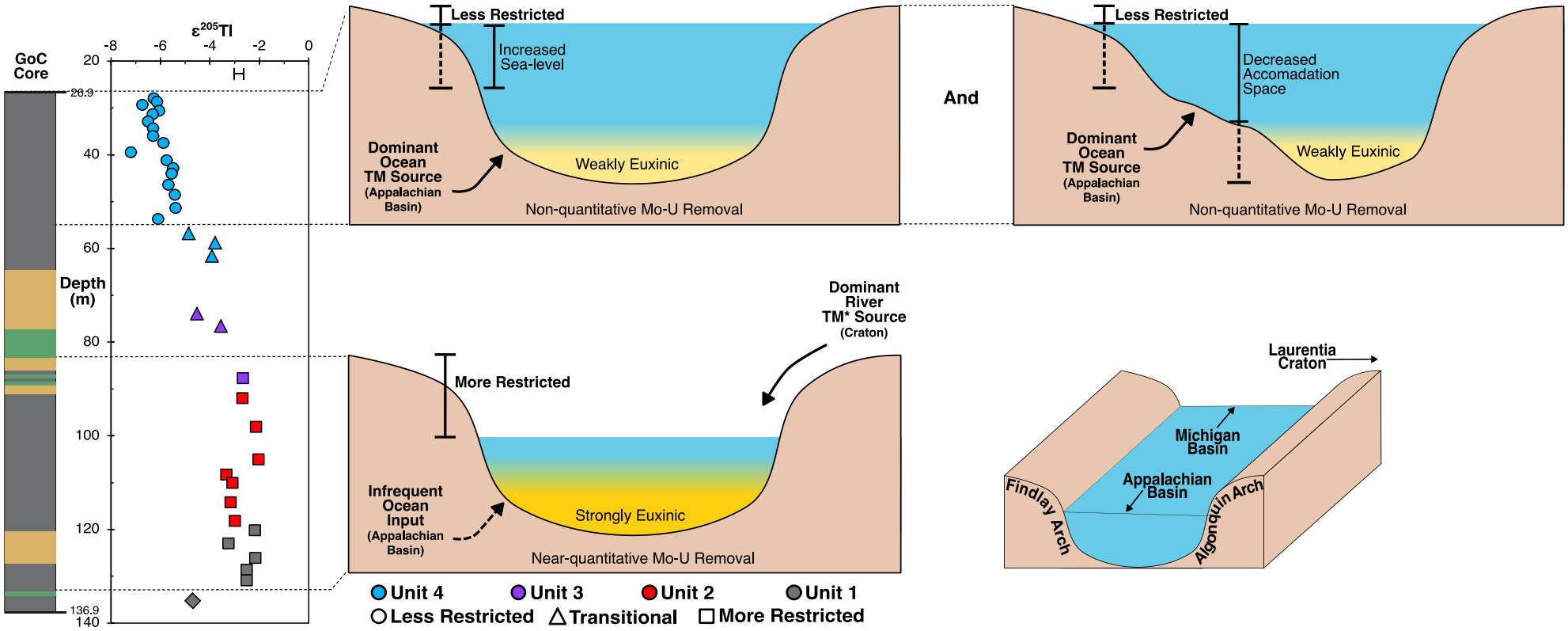

Figure 24a Depositional model showing changes to local redox conditions and basin restriction of the Chatham Sag during the Famennian. *TMs include Tl, V, and Re and exclude Mo and U for riverine source. Not to scale.

7.5.2 Glacial Meltwater Mechanism for Decreased Paleosalinity

The transition from marine to brackish salinity could have been caused by several changes to the hydrology of the Chatham Sag. More specifically, the brackish salinity conditions are the result of an increase in freshwater and not a decrease in marine water inputs, which was previously ruled out due to the high TMs of upper Unit 4. The first source of freshwater considered is low-saline meltwater from the Acadian highland glaciations (Figure 24b). Mixing of meltwater and seawater in the central Appalachian Basin followed by subsequent transport of the brackish water to the Chatham Sag could be a possible mechanism. Paleosalinity data of the Ohio Shale Formation record a subtle lateral change in salinity from low-brackish in the northern region to high-brackish in the southern Central Appalachian Basin during the Middle Devonian to Early Mississippian, but was attributed to freshwater inputs from the Catskill delta to the north (Gilleaudeau et al., 2021) and not specifically glacial meltwater. The stratigraphic trends of the Ohio Shale proxies were not provided, and a temporal shift in salinities cannot be identified in the Central Appalachian Basin and correlated to this study. Regardless, the Chatham Sag could have received an influx of brackish waters from the Appalachian Basin during Unit 4, causing the deep waters of the Chatham Sag to become brackish as well. Additionally, the onset of brackish conditions of upper Unit 3 coincides with deltaic draining of the Acadian highlands into the Central Appalachian Basin, which was recorded in the stratigraphically equivalent Chagrin Shale Member. The contact between the grey Chagrin Shale and the black Cleveland Shale Members consist of thinly interbedded black and grey shales, and are considered intercalated vertical transition contacts or intercalated zones (ICZs) (Dunkel et al., 2022). The ICZs are interpreted as lateral migrations of two coeval depositional environments. Black shales represent freshwater flooding of active deltaic channels that transported high amounts of nutrients, sediment, and terrestrial OM to the Appalachian Basin, and grey shales represent flooding outside of active channels, such as between the channels or into abandoned deltaic lobes (Dunkel et al., 2022). While Dunkel et al. (2022) do not specify the cause of flooding, episodes of glacial meltout from alpine glaciers in the Acadian highlands are not disregarded as a possible flooding mechanism and a source of increased freshwater to the Appalachian Basin and neighbouring Chatham Sag. However, this flooding could also be caused by increased precipitation around the eastern NAS.

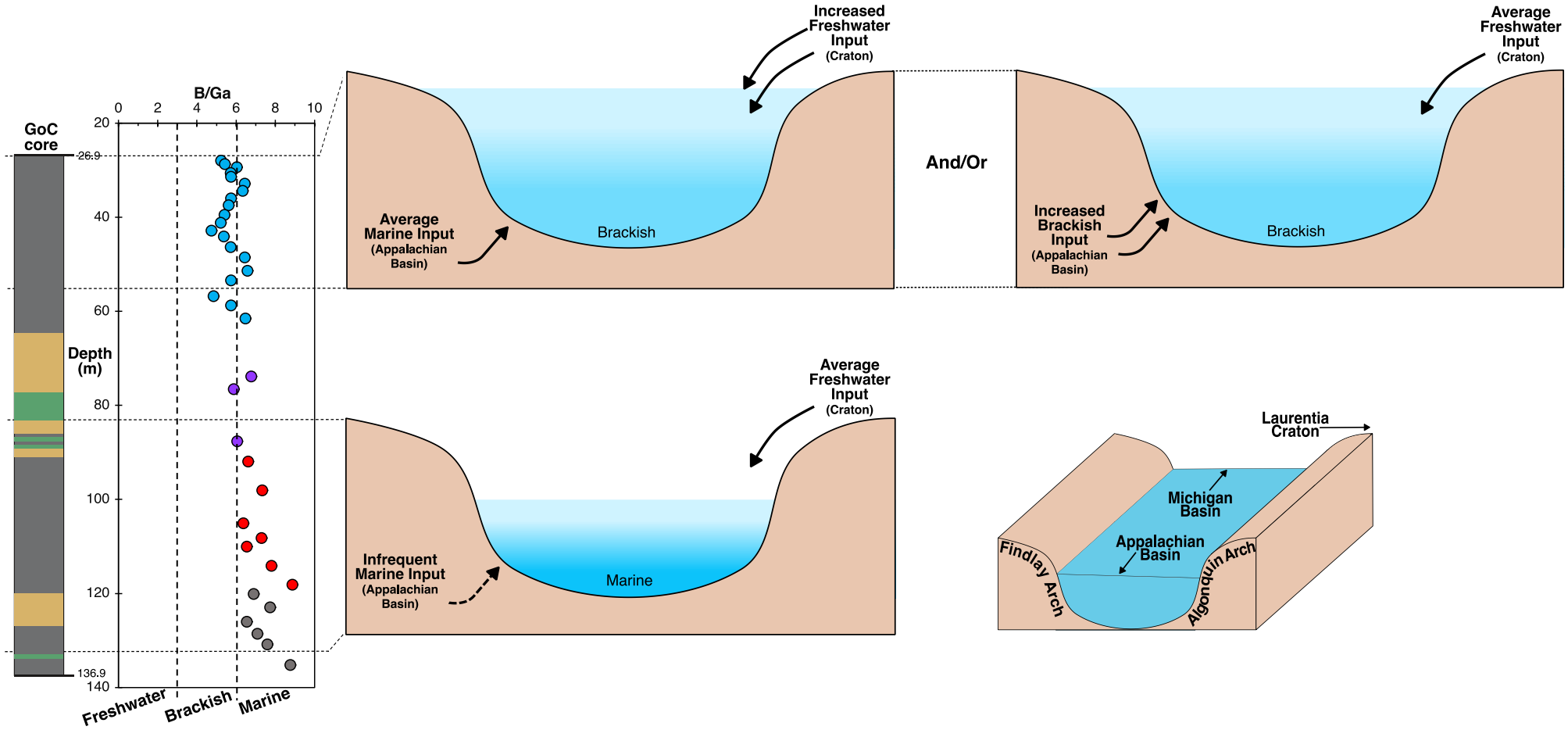

Figure 24b Depositional model showing changes to hydrological conditions of the Chatham Sag during the Famennian. Not to scale.

7.4.3. Regional Climate Mechanism for Decreased Paleosalinity

The final mechanism to consider is an increase in regional precipitation and continental run-off as a freshwater source to the Chatham Sag (Figure 24b), which may have coincided with a shift in regional climate from warm and dry to cool and wet conditions during the Famennian. Although glacial meltwaters could be responsible for the brackish salinity and deltaic flooding events in the Central Appalachian Basin, increased precipitation across the eastern Laurentian Craton could also be responsible for such conditions. A previous study of the Cleveland Shale Member in the Central Appalachian Basin found increased TOC and terrestrial organic matter (OM) in comparison to lower members, which is linked to an increased sediment flux into the basin (Rimmer et al., 2004). Lu et al. (2019) also noted an increase in terrestrial macerals (i.e. vitrinite and inertinite) and plant remanents in conjuction with an increase in terrestrial weathering proxies and detrital sediment input within the upper Chattanooga Shale of the Southern Appalachian Basin. In the Illinois Basin to the paleo-south, the Gassaway Member of the Chattanooga Shale Formation exhibits increased terrestrial inputs and a simultaneous shift from marine to brackish paleosalinity at the beginning of the Fammenian (Song et al., 2021). These increasing trends can be attributed to a wetter paleoclimate that increased precipitation and terrestrial weathering, which consequently increased sediment and terrestrial OM transport to regions around the eastern NAS. Furthermore, the most compelling evidence of climate transition can be seen in coeval terrestrial facies of the Catskill Formation. Located in the Northern Appalachian Basin, a gradational shift in Catskill lithofacies' colour and thickness was attributed to a change in precipitation intensity and frequency (Brezinski et al., 2009). More specifically, the Upper Famennian Duncannon Member contains a transition zone from thin reddish sandstone beds and paleo-entisols produced in drier climates to thicker green-grey sandstone facies and paleo-vertisols produced in wetter climates (Brezinski et al., 2009).

Unlike the surrounding formations, the organic geochemical indicators of Kettle Point black shales do not show obvious increases of terrestrial OM inputs. There is an increase in TOC contents (Figure 17e) and an increase in $\delta^{13}C$ to less negative values (Figure17d) moving stratigraphically upsection. However, Devonian-aged terrestrial OM has $\delta^{13}C$ ratios of ~ –26‰ and marine-sourced OM ratios are ~ –30‰ (Maynard, 1981), and the highest $\delta^{13}C$ value of –29.1‰ is located in the transitional period of the lower Unit 4. Although the OM of Kettle Point black shales were evaluated as marine-derived (Kendall et al., 2020), a trend to less negative values in Unit 4 may indicate increased organic contents of terrestrial provenance (Maynard, 1981). One factor that may have suppressed the $\delta^{13}C$ from

reaching terrestrial values is the proximity of the GoC core to ancient shorelines (Maynard, 1981) and its distance from the shores of the Laurentian Craton may have been too far to receive terrestrial OM from freshwater inputs. A more probable factor could be the simultaneous increase in buried marine-derived OM attributed to intolerance of low-salinity conditions. Organisms and microbial communities that thrive in high-salinity environments could have been displaced and buried in basin sediments. For example, a shift to low-brackish paleosalinity during the Famennian-aged Gassaway Member of the Illinois Basin favoured low-salinity bacteria and algal communities that replaced high-salinity microorganisms (Song et al., 2021). Support for both terrestrial- and marine-derived OM in the Kettle Point black shales is reflected by the predominance of intermediate Type II kerogen in most Kettle Point black shales (Obermajer et al., 1997), however, some samples exhibit an increase in Type III kerogen that is derived from woody plant matter (Béland-Otis, 2013; Hamblin, 2010; Obermajer et al., 1997). The stratigraphic positions of these Type III samples are not indicated, and therefore, they cannot be directly correlated to geochemical trends of this study. Furthermore, vitrinite was also found in Kettle Point black shales (Delitala, 1984), but its abundance also has not been stratigraphically described. It is recommended that future research of Kettle Point kerogen types and organic macerals include stratigraphic positions to utilize these geochemical indicators for paleoenvironmental reconstruction through deep-time.

Conclusions

This study used the combination of Tl - Mo - U isotope paleoredox proxies with paleosalinity proxies of the Kettle Point Formation black shales to constrain the paleodepositional environment of Chatham Sag throughout the Famennian Stage. The triple isotope paleoredox proxies showed a shift in local deep-basin redox, from strongly to weakly euxinic conditions, and revealed a change in the Chatham Sag's connection to the ancient open ocean that shifted input sources from riverine to marine. Paleosalinity proxies exhibited a salinity shift from marine to brackish waters in the deep basin. The integration of these proxies further constrained the marine paleoenvironment conditions and allowed for the elimination of improbable and conflicting controls on watermass geochemistry. Specifically, the increase in TM enrichments from marine sources must have been caused by an increased sea-level that decreased in basin restriction, while the change to brackish conditions must have been from increased freshwater inputs to the Chatham Sag. Geochemical and stratigraphic evidence from neighbouring formations provided context for the regional conditions of the eastern North American Seaway, which displayed changes to its hydrology that could be explained by increased freshwater flooding and precipitation to the region. Ultimately, the Tl paleoredox proxy can capture small-scale local and regional paleoenvironmental shifts in ancient epeiric seas and should be interpreted with other geochemical proxies to assess the viability of large-scale, global ocean redox paleo-reconstructions.

Bibliography

ActLabs. (2022). *X-Ray Diffraction Analysis of Fifteen Samples: Report #A22-11779.*

Ahrens, J., Beck, M., Böning, P., Degenhardt, J., Pahnke, K., Schnetger, B., & Brumsack, H. J. (2021). Thallium cycling in pore waters of intertidal beach sediments. *Geochimica et Cosmochimica Acta*, *306*, 321–339. https://doi.org/10.1016/j.gca.2021.04.009

Algeo, T. J., Lyons, T. W., Blakey, R. C., & Over, D. J. (2007). Hydrographic conditions of the Devono–Carboniferous North American Seaway inferred from sedimentary Mo–TOC relationships. *Palaeogeography, Palaeoclimatology, Palaeoecology*, *256*(3–4), 204–230. https://doi.org/10.1029/2004PA001112

Algeo, T. J., & Tribovillard, N. (2009). Environmental analysis of paleoceanographic systems based on molybdenum-uranium covariation. *Chemical Geology*, *268*(3–4), 211–225. https://doi.org/10.1016/j.chemgeo.2009.09.001

Anbar, A. D. (2004). Molybdenum stable isotopes: Observations, interpretations and directions. In *Reviews in Mineralogy and Geochemistry* (Vol. 55). https://doi.org/10.2138/gsrmg.55.1.429

Andersen, M. B., Matthews, A. D., Bar-Matthews, M., & Vance, D. (2020). Rapid onset of ocean anoxia shown by high U and low Mo isotope compositions of sapropel S1. *Geochemical Perspectives Letters*, *15*, 10. https://doi.org/10.7185/geochemlet.2027

Andersen, M. B., Romaniello, S. J., Vance, D., Little, S. H., Herdman, R., & Lyons, T. W. (2014). A modern framework for the interpretation of 238U/235U in studies of ancient ocean redox. *Earth and Planetary Science Letters*, *400*, 184–194. https://doi.org/10.1016/j.epsl.2014.05.051

Andersen, M. B., Stirling, C. H., & Weyer, S. (2017). Uranium isotope fractionation. *Non-Traditional Stable Isotopes*, *82*, 799–850. https://doi.org/10.2138/rmg.2017.82.19

Archer, C., & Vance, D. (2008). The isotopic signature of the global riverine molybdenum flux and anoxia in the ancient oceans. *Nature Geoscience*, *1*(9), 597–600. https://doi.org/10.1038/ngeo282

Armstrong, D. K. (1987). *Trace element geochemistry and petrology of the Kettle Point Formation (Upper Devonian), a black shale unit of southwestern Ontario*. University of Waterloo.

Ashiwabara, T. K., Akahashi, Y. T., & Animizu, M. T. (2009). A XAFS study on the mechanism of isotopic fractionation of molybdenum during its adsorption on ferromanganese oxides. *Geochemical Journal*, *43*, 31–36.

Barling, J., Arnold, G. L., & Anbar, A. D. (2001). Natural mass-dependent variations in the isotopic composition of molybdenum. *Earth and Planetary Science Letters*, *193*(3–4), 447–457.

https://doi.org/10.1016/S0012-821X(01)00514-3

Barnes, C. E., & Cochran, J. K. (1993). Uranium geochemistry in estuarine sediments: Controls on removal and release processes. *Geochimica et Cosmochimica Acta*, *57*(3), 555–569. https://doi.org/10.1016/0016-7037(93)90367-6

Basu, A., Sanford, R. A., Johnson, T. M., Lundstrom, C. C., & Löffler, F. E. (2014). Uranium isotopic fractionation factors during U(VI) reduction by bacterial isolates. *Geochimica et Cosmochimica Acta*, *136*, 100–113. https://doi.org/10.1016/j.gca.2014.02.041

Béland-Otis, C. (2013). *Gas Assessment of the Devonian Kettle Point Formation: Vol. Open File*.

Bennett, W. W., & Canfield, D. E. (2020). Redox-sensitive trace metals as paleoredox proxies: A review and analysis of data from modern sediments. *Earth-Science Reviews*, *204*(March), 103175. https://doi.org/10.1016/j.earscirev.2020.103175

Bidoglio, G., Gibson, P. N., O'Gorman, M., & Roberts, K. J. (1993). X-ray absorption spectroscopy investigation of surface redox transformations of thallium and chromium on colloidal mineral oxides. *Geochimica et Cosmochimica Acta*, *57*(10), 2389–2394. https://doi.org/10.1016/0016-7037(93)90576-I

Bingham-Koslowski, N. (2015). *High resolution stratigraphy and paleoenvironmental reconstruction of the Upper Devonian Kettle Point Formation , southwestern Ontario , Canada* (Issue August). University of Western Ontario.

Bingham-Koslowski, N., Tsujita, C. J., Jin, J., & Azmy, K. (2016). Widespread late devonian marine anoxia in eastern north america: A case study of the kettle point formation black shale, Southwestern Ontario. *Canadian Journal of Earth Sciences*, *53*(8), 837–855. https://doi.org/10.1139/cjes-2015-0227

Bowman, C. N., Young, S. A., Kaljo, D., Eriksson, M. E., Them, T. R., Hints, O., Martma, T., & Owens, J. D. (2019). Linking the progressive expansion of reducing conditions to a stepwise mass extinction event in the late Silurian oceans. *Geology*, *47*(10), 968–972. https://doi.org/10.1130/G46571.1

Brennecka, G. A., Wasylenki, L. E., Bargar, J. R., Weyer, S., & Anbar, A. D. (2011). Uranium isotope fractionation during adsorption to Mn-oxyhydroxides. *Environmental Science and Technology*, *45*(4), 1370–1375. https://doi.org/10.1021/es103061v

Brett, A., Prytulak, J., Hammond, S. J., & Rehkämper, M. (2018). Thallium Mass Fraction and Stable Isotope Ratios of Sixteen Geological Reference Materials. *Geostandards and Geoanalytical*

Research, *42*(3), 339–360. https://doi.org/10.1111/ggr.12215

Brezinski, D. K., Cecil, C. B., & Skema, V. W. (2010). Late Devonian glacigenic and associated facies from the central Appalachian Basin, eastern United States. *Bulletin of the Geological Society of America*, *122*(1–2), 265–281. https://doi.org/10.1130/B26556.1

Brezinski, D. K., Cecil, C. B., Skema, V. W., & Kertis, C. A. (2009). Evidence for long-term climate change in Upper Devonian strata of the central Appalachians. *Palaeogeography, Palaeoclimatology, Palaeoecology*, *284*(3–4), 315–325. https://doi.org/10.1016/j.palaeo.2009.10.010

Brezinski, D. K., Cecil, C. B., Skema, V. W., & Stamm, R. (2008). Late Devonian glacial deposits from the eastern United States signal an end of the mid-Paleozoic warm period. *Palaeogeography, Palaeoclimatology, Palaeoecology*, *268*(3–4), 143–151. https://doi.org/10.1016/j.palaeo.2008.03.042

Brown, T. C., & Kenig, F. (2004). Water column structure during deposition of Middle Devonian–Lower Mississippian black and green/gray shales of the Illinois and Michigan Basins: a biomarker approach. *Palaeogeography, Palaeoclimatology, Palaeoecology*, *215*(1–2), 59–85. https://doi.org/10.1016/j.palaeo.2004.08.004

Brüske, A., Weyer, S., Zhao, M. Y., Planavsky, N. J., Wegwerth, A., Neubert, N., Dellwig, O., Lau, K. V., & Lyons, T. W. (2020). Correlated molybdenum and uranium isotope signatures in modern anoxic sediments: Implications for their use as paleo-redox proxy. *Geochimica et Cosmochimica Acta*, *270*, 449–474. https://doi.org/10.1016/j.gca.2019.11.031

Bura-Nakić, E., Andersen, M. B., Archer, C., de Souza, G. F., Marguš, M., & Vance, D. (2018). Coupled Mo-U abundances and isotopes in a small marine euxinic basin: Constraints on processes in euxinic basins. *Geochimica et Cosmochimica Acta*, *222*, 212–229. https://doi.org/10.1016/j.gca.2017.10.023

Burns, R. G., Burns, V. M., & Easton, A. J. (1977). *The Mineralogy and Crystal Chemistry of Deep-Sea Manganese Nodules, a Polymetallic Resource of the Twenty-First Century (and Discussion)*. *286*(1336), 283–301.

Calvert, S. E., & Pedersen, T. F. (1993). Geochemistry of recent oxic and anoxic marine sediments: Implications for the geological record. *Marine Geology*, *113*(1–2), 67–88. https://doi.org/10.1016/0025-3227(93)90150-T

Calvert, S. E., & Pedersen, T. F. (1996). Sedimentary geochemistry of manganese: Implications for the

environment of formation of manganiferous black shales. *Economic Geology*, *91*(1), 36–47. https://doi.org/10.2113/gsecongeo.91.1.36

Canfield, D. E., & Thamdrup, B. (2009). Towards a consistent classification scheme for geochemical environments, or, why we wish the term "suboxic" would go away: Editorial. *Geobiology*, *7*(4), 385–392. https://doi.org/10.1111/j.1472-4669.2009.00214.x

Čejka, J., & Muck, A. (1984). To the infrared spectroscopy of natural uranyl phosphates. *Physics and Chemistry of Minerals*, *11*(4), 172–177. https://doi.org/10.1007/BF00387848

Chen, X., Li, S., Newby, S. M., Lyons, T. W., Wu, F., & Owens, J. D. (2022). Iron and manganese shuttle has no effect on sedimentary thallium and vanadium isotope signatures in Black Sea sediments. *Geochimica et Cosmochimica Acta*, *317*, 218–233. https://doi.org/10.1016/j.gca.2021.11.010

Cheng, M., Li, C., Jin, C., Wang, H., Algeo, T. J., Lyons, T. W., Zhang, F., & Anbar, A. (2020). Evidence for high organic carbon export to the early Cambrian seafloor. *Geochimica et Cosmochimica Acta*, *287*, 125–140. https://doi.org/10.1016/j.gca.2020.01.050

Clarkson, M. O., Sweere, T. C., Chiu, C. F., Hennekam, R., Bowyer, F., & Wood, R. A. (2023). Environmental controls on very high δ238U values in reducing sediments: Implications for Neoproterozoic seawater records. *Earth-Science Reviews*, *237*(November 2022), 104306. https://doi.org/10.1016/j.earscirev.2022.104306

Cluff, R. M. (1980). Paleoenvironment of the New Albany Shale group (Devonian-Misssissippian) of Illinois. *Journal of Sedimentary Petrology*, *50*(3), 767–780.

Crusius, J., Calve, S., Pedersen, T. F., & Sage, D. (1996). Rhenium and molybdenum enrichments in sediments as indicators of Oxic, Suboxic and Sulfidic Conditions of Deposition. *Earth and Planetary Science Letters 145*, *145*(96), 65–78.

Dahl, T. W., Anbar, A. D., Gordon, G. W., Rosing, M. T., Frei, R. E., & Canfield, D. E. (2010). The behavior of molybdenum and its isotopes across the chemocline and in the sediments of sulfidic Lake Cadagno, Switzerland. *Geochimica et Cosmochimica Acta*, *74*(1), 144–163. https://doi.org/10.1016/j.gca.2009.09.018

Dahl, T. W., Chappaz, A., Fitts, J. P., & Lyons, T. W. (2013). Molybdenum reduction in a sulfidic lake: Evidence from X-ray absorption fine-structure spectroscopy and implications for the Mo paleoproxy. *Geochimica et Cosmochimica Acta*, *103*, 213–231. https://doi.org/10.1016/j.gca.2012.10.058

Dahl, T. W., Chappaz, A., Hoek, J., McKenzie, C. J., Svane, S., & Canfield, D. E. (2017). Evidence of molybdenum association with particulate organic matter under sulfidic conditions. *Geobiology*, *15*(2), 311–323. https://doi.org/10.1111/gbi.12220

Dauphas, N., & Schauble, E. A. (2016). Mass Fractionation Laws, Mass-Independent Effects, and Isotopic Anomalies. *Annual Review of Earth and Planetary Sciences*, *44*, 709–783. https://doi.org/10.1146/annurev-earth-060115-012157

Delitala, F. A. (1984). *The Mineralogy and Geochemistry of the Kettle Point Oil Shale, S.W. Ontario* [University of Western Ontario]. https://books.google.ca/books?id=wtvwvgEACAAJ

Dellwig, O., Leipe, T., März, C., Glockzin, M., Pollehne, F., Schnetger, B., Yakushev, E. V., Böttcher, M. E., & Brumsack, H. J. (2010). A new particulate Mn-Fe-P-shuttle at the redoxcline of anoxic basins. *Geochimica et Cosmochimica Acta*, *74*(24), 7100–7115. https://doi.org/10.1016/j.gca.2010.09.017

Duchamp-Alphonse, S., Fiet, N., Adatte, T., & Pagel, M. (2011). Climate and sea-level variations along the northwestern Tethyan margin during the Valanginian C-isotope excursion: Mineralogical evidence from the Vocontian Basin (SE France). *Palaeogeography, Palaeoclimatology, Palaeoecology*, *302*(3–4), 243–254. https://doi.org/10.1016/j.palaeo.2011.01.015

Dunk, R. M., Mills, R. A., & Jenkins, W. J. (2002). A reevaluation of the oceanic uranium budget for the Holocene. *Chemical Geology*, *190*(1–4), 45–67. https://doi.org/10.1016/S0009-2541(02)00110-9

Dunkel, C. A., Vázquez-Ortega, A., & Evans, J. E. (2022). Black shale–gray shale transitions in a Late Devonian shale succession, Central Appalachian Basin (Northern Ohio): Sedimentary and geochemical evidence for terrestrial organic matter input driving anoxia events. *Palaeogeography, Palaeoclimatology, Palaeoecology*, *608*(October), 111271. https://doi.org/10.1016/j.palaeo.2022.111271

Erickson, B. E., & Helz, G. R. (2000). Molybdenum(VI) speciation in sulfidic waters: Stability and lability of thiomolybdates. *Geochimica et Cosmochimica Acta*, *64*(7), 1149–1158. https://doi.org/10.1016/S0016-7037(99)00423-8

Ettensohn, F. R., Clayton, G., Mason, C. E., & Krause, F. (2020). Late Devonian lonestones, diamictites, and coeval black shales from the Appalachian Basin: Discerning relationships and implications for Late Devonian Appalachian history and glacially driven seafloor anoxia. In *The Appalachian Geology of John M. Dennison: Rocks, People, and a Few Good Restaurants along the Way* (Issue

Special Paper 545). The Geological Society of America. https://doi.org/10.1130/2020.2545(05)CITATIONS

Ettensohn, F. R., Lierman, T. R., & Mason, C. E. (2007). Dropstones, Glaciation, and Black Shales: New Inferences on Black-Shale Origins from the Upper Ohio Shale in Northeastern Kentucky. *American Association of Petroleum Geologists Eastern Section Meeting Abstracts with Programs*, 33–34.

Ettensohn, F. R., Pashin, J. C., & Gilliam, W. (2019). Chapter 4 - The Appalachian and Black Warrior Basins: Foreland Basins in the Eastern United States. In A. D. B. T.-T. S. B. of the U. S. and C. (Second E. Miall (Ed.), *The Sedimentary Basins of the United States and Canada* (pp. 129–237). Elsevier. https://doi.org/https://doi.org/10.1016/B978-0-444-63895-3.00004-8

Ettensohn, F. R., Seckinger, D. C., Eble, C. F., Clayton, G., Li, J., Martins, G. A., Hodelka, B. N., Lo, E. L., Harris, F. R., & Taghizadeh, N. (2020). Age and tectonic significance of diamictites at the Devonian- Mississippian transition in the central Appalachian Basin. In C. S. Swezey & M. W. Carter (Eds.), *Geology Field Trips in and around the U.S. Capital* (Vol. 57, Issue May, pp. 79–103). The Geological Society of America. https://doi.org/10.1130/2020.0057(04)

Fan, H., Nielsen, S. G., Owens, J. D., Auro, M., Shu, Y., Hardisty, D. S., Horner, T. J., Bowman, C. N., Young, S. A., & Wen, H. (2020). Constraining oceanic oxygenation during the Shuram excursion in South China using thallium isotopes. *Geobiology*, *18*(3), 348–365. https://doi.org/10.1111/gbi.12379

Fu, Y. (2020). Non-traditional stable isotope geochemistry of marine ferromanganese crusts and nodules. *Journal of Oceanography*, *76*(2), 71–89. https://doi.org/10.1007/s10872-019-00534-5

Garrido, F., Garcia-Guinea, J., Lopez-Arce, P., Voegelin, A., Göttlicher, J., Mangold, S., & Almendros, G. (2020). Thallium and co-genetic trace elements in hydrothermal Fe-Mn deposits of Central Spain. *Science of the Total Environment*, *717*, 137162. https://doi.org/10.1016/j.scitotenv.2020.137162

Gaschnig, R. M., Rudnick, R. L., McDonough, W. F., Kaufman, A. J., Valley, J. W., Hu, Z., Gao, S., & Beck, M. L. (2016). Compositional evolution of the upper continental crust through time, as constrained by ancient glacial diamictites. *Geochimica et Cosmochimica Acta*, *186*, 316–343. https://doi.org/10.1016/j.gca.2016.03.020

Gilleaudeau, G. J., Algeo, T. J., Lyons, T. W., Bates, S., & Anbar, A. D. (2021). Novel watermass reconstruction in the Early Mississippian Appalachian Seaway based on integrated proxy records of

redox and salinity. *Earth and Planetary Science Letters*, *558*, 116746. https://doi.org/10.1016/j.epsl.2021.116746

Goldberg, S., Forster, H. S., & Godfrey, C. L. (1996). Molybdenum Adsorption on Oxides, Clay Minerals, and Soils. *Soil Science Society of America Journal*, *60*(2), 425–432. https://doi.org/10.2136/sssaj1996.03615995006000020013x

Goldberg, T., Archer, C., Vance, D., & Poulton, S. W. (2009). Mo isotope fractionation during adsorption to Fe (oxyhydr)oxides. *Geochimica et Cosmochimica Acta*, *73*(21), 6502–6516. https://doi.org/10.1016/j.gca.2009.08.004

Goldberg, T., Archer, C., Vance, D., Thamdrup, B., McAnena, A., & Poulton, S. W. (2012). Controls on Mo isotope fractionations in a Mn-rich anoxic marine sediment, Gullmar Fjord, Sweden. *Chemical Geology*, *296–297*, 73–82. https://doi.org/10.1016/j.chemgeo.2011.12.020

Gustafsson, J. P. (2003). Modelling molybdate and tungstate adsorption to ferrihydrite. *Chemical Geology*, *200*(1), 105–115. https://doi.org/https://doi.org/10.1016/S0009-2541(03)00161-X

Hamblin, A. P. (2010). Detailed outcrop and core measured sections of the Kettle Point Formation, southwestern Ontario, with reference to shale gas potential. *Geological Survey of Canada Open File*, *6579*, 1–26. https://doi.org/10.4095/285564

Helz, G. R., Bura-Nakić, E., Mikac, N., & Ciglenečki, I. (2011). New model for molybdenum behavior in euxinic waters. *Chemical Geology*, *284*(3–4), 323–332. https://doi.org/10.1016/j.chemgeo.2011.03.012

Helz, G. R., Miller, C. V., Charnock, J. M., Mosselmans, J. F. W., Pattrick, R. A. D., Garner, C. D., & Vaughan, D. J. (1996). Mechanism of molybdenum removal from the sea and its concentration in black shales: EXAFS evidence. *Geochimica et Cosmochimica Acta*, *60*(19), 3631–3642. https://doi.org/10.1016/0016-7037(96)00195-0

Helz, G. R., & Vorlicek, T. P. (2019). Precipitation of molybdenum from euxinic waters and the role of organic matter. *Chemical Geology*, *509*(January), 178–193. https://doi.org/10.1016/j.chemgeo.2019.02.001

Henshaw, P. C., Charlson, R. J., & Burges, S. J. (2000). 6 - Water and the Hydrosphere. In M. C. Jacobson, R. J. Charlson, H. Rodhe, & G. H. B. T.-I. G. Orians (Eds.), *Earth System Science* (Vol. 72, pp. 109–131). Academic Press. https://doi.org/https://doi.org/10.1016/S0074-6142(00)80112-6

Herrmann, A. D., Kendall, B., Algeo, T. J., Gordon, G. W., Wasylenki, L. E., & Anbar, A. D. (2012). Anomalous molybdenum isotope trends in Upper Pennsylvanian euxinic facies: Significance for

use of δ 98Mo as a global marine redox proxy. *Chemical Geology*, *324–325*, 87–98. https://doi.org/10.1016/j.chemgeo.2012.05.013

Hlohowskyj, S. R., Chappaz, A., & Dickson, A. J. (2021). Molybdenum as a paleoredox proxy. In *Cambridge Elements: Geochemical Tracers in Earth System Science*. Cambridge University Press. https://doi.org/10.1017/9781108993777

Isaacson, P. E., Díaz-Martínez, E., Grader, G. W., Kalvoda, J., Babek, O., & Devuyst, F. X. (2008). Late Devonian-earliest Mississippian glaciation in Gondwanaland and its biogeographic consequences. *Palaeogeography, Palaeoclimatology, Palaeoecology*, *268*(3–4), 126–142. https://doi.org/10.1016/j.palaeo.2008.03.047

Ivanovich, M., & Harmon, R. S. (Eds.). (1992). *Uranium-series disequilibrium: Applications to earth, marine, and environmental sciences* (2nd ed.). Clarendon Press.

Joachimski, M. M., Breisig, S., Buggisch, W., Talent, J. A., Mawson, R., Gereke, M., Morrow, J. R., Day, J., & Weddige, K. (2009). Devonian climate and reef evolution: Insights from oxygen isotopes in apatite. *Earth and Planetary Science Letters*, *284*(3–4), 599–609. https://doi.org/10.1016/j.epsl.2009.05.028

Johnson, J. G., Klapper, G., & Sandberg, C. A. (1985). Devonian eustatic fluctuations in Euramerica. *Geological Society Of America Bulletin*, *96*(5), 567–587. https://doi.org/10.1130/0016-7606(1985)96<567

Kendall, B., Dahl, T. W., & Anbar, A. D. (2017). Good Golly, Why Moly? The stable isotope geochemistry of molybdenum. *Reviews in Mineralogy and Geochemistry*, *82*(1), 683–732. https://doi.org/10.2138/rmg.2017.82.16

Kendall, B., Wang, J., Zheng, W., Romaniello, S. J., Over, D. J., Bennett, Y., Xing, L., Kunert, A., Boyes, C., & Liu, J. (2020). Inverse correlation between the molybdenum and uranium isotope compositions of Upper Devonian black shales caused by changes in local depositional conditions rather than global ocean redox variations. *Geochimica et Cosmochimica Acta*, *287*, 141–164. https://doi.org/10.1016/j.gca.2020.01.026

Kerl, C. F., Lohmayer, R., Bura-Nakić, E., Vance, D., & Planer-Friedrich, B. (2017). Experimental Confirmation of Isotope Fractionation in Thiomolybdates Using Ion Chromatographic Separation and Detection by Multicollector ICPMS. *Analytical Chemistry*, *89*(5), 3123–3129. https://doi.org/10.1021/acs.analchem.6b04898

King, E. K., Perakis, S. S., & Pett-Ridge, J. C. (2018). Molybdenum isotope fractionation during

adsorption to organic matter. *Geochimica et Cosmochimica Acta*, *222*, 584–598. https://doi.org/10.1016/j.gca.2017.11.014

King, E. K., & Pett-Ridge, J. C. (2018). Reassessing the dissolved molybdenum isotopic composition of ocean inputs: The effect of chemical weathering and groundwater. *Geology*, *46*(11), 955–958. https://doi.org/10.1130/G45124.1

Klinkhammer, G. P., & Palmer, M. R. (1991). Uranium in the oceans: Where it goes and why. *Geochimica et Cosmochimica Acta*, *55*(7), 1799–1806. https://doi.org/10.1016/0016-7037(91)90024-Y

Lau, K. V, Romaniello, S. J., & Zhang, F. (2019). The uranium isotope paleoredox proxy. In *Cambridge Elements: Geochemical Tracers in Earth System Science*. Cambridge University Press.

Lenstra, W. K., Séguret, M. J. M., Behrends, T., Groeneveld, R. K., Hermans, M., Witbaard, R., & Slomp, C. P. (2020). Controls on the shuttling of manganese over the northwestern Black Sea shelf and its fate in the euxinic deep basin. *Geochimica et Cosmochimica Acta*, *273*, 177–204. https://doi.org/10.1016/j.gca.2020.01.031

Li, Q., Zhu, B., & Li, J. (2020). A comparative study on the micro-surface characteristics at black shale initial oxidation stage. *Scientific Reports*, *10*(1), 1–9. https://doi.org/10.1038/s41598-020-67268-z

Li, Z., Cole, D. B., Newby, S. M., Owens, J. D., Kendall, B., & Reinhard, C. T. (2021). New constraints on mid-Proterozoic ocean redox from stable thallium isotope systematics of black shales. *Geochimica et Cosmochimica Acta*, *315*, 185–206. https://doi.org/10.1016/j.gca.2021.09.006

Little, S. H., Vance, D., Lyons, T. W., & McManus, J. (2015). Controls on trace metal authigenic enrichment in reducing sediments: Insights from modern oxygen-deficient settings. *American Journal of Science*, *315*(2), 77–119. https://doi.org/10.2475/02.2015.01

Liu, J., Cao, J., Yuan, W., Zhong, Q., Xiong, X., Ouyang, Q., Wei, X., Liu, Y., Wang, J., & Li, X. (2023). Thallium adsorption on three iron (hydr)oxides and Tl isotopic fractionation induced by adsorption on ferrihydrite. *Science of the Total Environment*, *871*(January), 161863. https://doi.org/10.1016/j.scitotenv.2023.161863

Liu, X., Li, A., Dong, J., Zhuang, G., Xu, F., & Wan, S. (2018). Nonevaporative origin for gypsum in mud sediments from the East China Sea shelf. *Marine Chemistry*, *205*(August), 90–97. https://doi.org/10.1016/j.marchem.2018.08.009

Lovley, D. R., Phillips, E. J. P., Gorby, Y. A., & Landa, E. R. (1991). Microbial reduction of uranium. *Nature*, *350*(6317), 413–416. http://pubs.er.usgs.gov/publication/70016631

Lu, M., Lu, Y. H., Ikejiri, T., Hogancamp, N., Sun, Y., Wu, Q., Carroll, R., Çemen, I., & Pashin, J. (2019). Geochemical Evidence of First Forestation in the Southernmost Euramerica from Upper Devonian (Famennian) Black Shales. *Scientific Reports*, *9*(1), 1–15. https://doi.org/10.1038/s41598-019-43993-y

Lu, X., Dahl, T. W., Zheng, W., Wang, S., & Kendall, B. (2020). Estimating ancient seawater isotope compositions and global ocean redox conditions by coupling the molybdenum and uranium isotope systems of euxinic organic-rich mudrocks. *Geochimica et Cosmochimica Acta*, *290*, 76–103. https://doi.org/10.1016/j.gca.2020.08.032

Martin, L. A., Wissocq, A., Benedetti, M. F., & Latrille, C. (2018). Thallium (Tl) sorption onto illite and smectite: Implications for Tl mobility in the environment. *Geochimica et Cosmochimica Acta*, *230*, 1–16. https://doi.org/10.1016/j.gca.2018.03.016

Matthews, A. D., & Riley, J. P. (1970). The occurrence of thallium in sea water and marine sediments. *Chemical Geology*, *6*(C), 149–152. https://doi.org/10.1016/0009-2541(70)90013-6

Maynard, J. B. (1981). Carbon isotopes as indicators of dispersal patterns in Devonian-Mississippian shales of the Appalachian Basin. *Geology*, *9*(6), 262–265. https://doi.org/10.1130/0091-7613(1981)9<262:CIAIOD>2.0.CO;2

McManus, J., Berelson, W. M., Klinkhammer, G. P., Hammond, D. E., & Holm, C. (2005). Authigenic uranium: Relationship to oxygen penetration depth and organic carbon rain. *Geochimica et Cosmochimica Acta*, *69*(1), 95–108. https://doi.org/10.1016/j.gca.2004.06.023

Miller, C. A., Peucker-Ehrenbrink, B., Walker, B. D., & Marcantonio, F. (2011). Re-assessing the surface cycling of molybdenum and rhenium. *Geochimica et Cosmochimica Acta*, *75*(22), 7146–7179. https://doi.org/10.1016/j.gca.2011.09.005

Morford, J. L., & Emerson, S. R. (1999). The geochemistry of redox sensitive trace metals in sediments. *Geochimica et Cosmochimica Acta*, *63*(11–12), 1735–1750. https://doi.org/10.1016/S0016-7037(99)00126-X

Morford, J. L., Emerson, S. R., Breckel, E. J., & Kim, S. H. (2005). Diagenesis of oxyanions (V, U, Re, and Mo) in pore waters and sediments from a continental margin. *Geochimica et Cosmochimica Acta*, *69*(21), 5021–5032. https://doi.org/10.1016/j.gca.2005.05.015

Morford, J. L., Martin, W. R., & Carney, C. M. (2009). Uranium diagenesis in sediments underlying bottom waters with high oxygen content. *Geochimica et Cosmochimica Acta*, *73*(10), 2920–2937. https://doi.org/10.1016/j.gca.2009.02.014

Morford, J. L., Martin, W. R., François, R., & Carney, C. M. (2009). A model for uranium, rhenium, and molybdenum diagenesis in marine sediments based on results from coastal locations. *Geochimica et Cosmochimica Acta*, *73*(10), 2938–2960. https://doi.org/10.1016/j.gca.2009.02.029

Nägler, T. F., Anbar, A. D., Archer, C., Goldberg, T., Gordon, G. W., Greber, N. D., Siebert, C., Sohrin, Y., & Vance, D. (2014). Proposal for an International Molybdenum Isotope Measurement Standard and Data Representation. *Geostandards and Geoanalytical Research*, *38*(2), 149–151. https://doi.org/10.1111/j.1751-908X.2013.00275.x

Nägler, T. F., Neubert, N., Böttcher, M. E., Dellwig, O., & Schnetger, B. (2011). Molybdenum isotope fractionation in pelagic euxinia: Evidence from the modern Black and Baltic Seas. *Chemical Geology*, *289*(1–2), 1–11. https://doi.org/10.1016/j.chemgeo.2011.07.001

Nameroff, T. J., & Balistrieri, L. S. (2002). Suboxic trace metal geochemisrty in the tropical North Pacific. *Geochimica et Cosmochimica Acta*, *66*(7), 1139–1158.

Neretin, L. N., Pohl, C., Jost, G., Leipe, T., & Pollehne, F. (2003). Manganese cycling in the Gotland Deep, Baltic Sea. *Marine Chemistry*, *82*(3–4), 125–143. https://doi.org/10.1016/S0304-4203(03)00048-3

Neubert, N., Nägler, T. F., & Böttcher, M. E. (2008). Sulfidity controls molybdenum isotope fractionation into euxinic sediments: Evidence from the modern Black Sea. *Geology*, *36*(10), 775–778. https://doi.org/10.1130/G24959A.1

Newby, S. M., Owens, J. D., Schoepfer, S. D., & Algeo, T. J. (2021). Transient ocean oxygenation at end-Permian mass extinction onset shown by thallium isotopes. *Nature Geoscience*, *14*(9), 678–683. https://doi.org/10.1038/s41561-021-00802-4

Nielsen, S. G., Goff, M., Hesselbo, S. P., Jenkyns, H. C., LaRowe, D. E., & Lee, C. T. A. (2011). Thallium isotopes in early diagenetic pyrite - A paleoredox proxy? *Geochimica et Cosmochimica Acta*, *75*(21), 6690–6704. https://doi.org/10.1016/j.gca.2011.07.047

Nielsen, S. G., Mar-Gerrison, S., Gannoun, A., LaRowe, D. E., Klemm, V., Halliday, A. N., Burton, K. W., & Hein, J. R. (2009). Thallium isotope evidence for a permanent increase in marine organic carbon export in the early Eocene. *Earth and Planetary Science Letters*, *278*(3–4), 297–307. https://doi.org/10.1016/j.epsl.2008.12.010

Nielsen, S. G., & Rehkämper, M. (2011). Thallium Isotopes and Their Application to Problems in Earth and Environmental Science. In M. Baskaran (Ed.), *Handbook of Environmental Isotope Geochemistry, Advances in Isotope Geochemistry* (pp. 247–269). Springer-Verlag.

https://doi.org/10.1007/978-3-642-10637-8

Nielsen, S. G., Rehkämper, M., Baker, J., & Halliday, A. N. (2004). The precise and accurate determination of thallium isotope compositions and concentrations for water samples by MC-ICPMS. *Chemical Geology*, *204*(1–2), 109–124. https://doi.org/10.1016/j.chemgeo.2003.11.006

Nielsen, S. G., Rehkämper, M., Porcelli, D., Andersson, P., Halliday, A. N., Swarzenski, P. W., Latkoczy, C., & Günther, D. (2005). Thallium isotope composition of the upper continental crust and rivers - An investigation of the continental sources of dissolved marine thallium. *Geochimica et Cosmochimica Acta*, *69*(8), 2007–2019. https://doi.org/10.1016/j.gca.2004.10.025

Nielsen, S. G., Rehkämper, M., & Prytulak, J. (2017). Investigation and Application of Thallium Isotope Fractionation. *Reviews in Mineralogy and Geochemistry*, *82*, 759–798.

Nielsen, S. G., Wasylenki, L. E., Rehkämper, M., Peacock, C. L., Xue, Z., & Moon, E. M. (2013). Towards an understanding of thallium isotope fractionation during adsorption to manganese oxides. *Geochimica et Cosmochimica Acta*, *117*, 252–265. https://doi.org/10.1016/j.gca.2013.05.004

Noordmann, J., Weyer, S., Montoya-Pino, C., Dellwig, O., Neubert, N., Eckert, S., Paetzel, M., & Böttcher, M. E. (2015). Uranium and molybdenum isotope systematics in modern euxinic basins: Case studies from the central Baltic Sea and the Kyllaren fjord (Norway). *Chemical Geology*, *396*, 182–195. https://doi.org/10.1016/j.chemgeo.2014.12.012

Obermajer, M., Fowler, M. G., Goodarzi, F., & Snowdon, L. R. (1997). Organic petrology and organic geochemistry of Devonian black shales in southwestern Ontario, Canada. *Organic Geochemistry*, *26*(3–4), 229–246.

Ostrander, C. M., Nielsen, S. G., Gadol, H. J., Villarroel, L., Wankel, S. D., Horner, T. J., Blusztajn, J., & Hansel, C. M. (2023). Thallium isotope cycling between waters, particles, and sediments across a redox gradient. *Geochimica et Cosmochimica Acta*, *348*, 397–409. https://doi.org/10.1016/j.gca.2023.03.028

Ostrander, C. M., Nielsen, S. G., Owens, J. D., Kendall, B., Gordon, G. W., Romaniello, S. J., & Anbar, A. D. (2019). Fully oxygenated water columns over continental shelves before the Great Oxidation Event. *Nature Geoscience*, *12*(3), 186–191. https://doi.org/10.1038/s41561-019-0309-7

Ostrander, C. M., Owens, J. D., & Nielsen, S. G. (2017). Constraining the rate of oceanic deoxygenation leading up to a Cretaceous Oceanic Anoxic Event (OAE-2: ~94 Ma). *Science Advances*, *3*(8), 1–5. https://doi.org/10.1126/sciadv.1701020

Ostrander, C. M., Owens, J. D., Nielsen, S. G., Lyons, T. W., Shu, Y., Chen, X., Sperling, E. A., Jiang,

G., Johnston, D. T., Sahoo, S. K., & Anbar, A. D. (2020). Thallium isotope ratios in shales from South China and northwestern Canada suggest widespread O2 accumulation in marine bottom waters was an uncommon occurrence during the Ediacaran Period. *Chemical Geology*, *557*(August), 119856. https://doi.org/10.1016/j.chemgeo.2020.119856

Over, D. J. (2002). The Frasnian/Famennian Boundary in central and eastern United States. *Palaeogeography, Palaeoclimatology, Palaeoecology*, *181*(1–3), 153–169. https://doi.org/10.1016/S0031-0182(01)00477-1

Owens, J. D. (2019). Application of thallium isotopes: Tracking marine oxygenation through manganese oxide burial. In *Cambridge Elements: Geochemical Tracers in Earth System Science*. Cambridge University Press. https://doi.org/10.1017/9781108688697

Owens, J. D., Nielsen, S. G., Horner, T. J., Ostrander, C. M., & Peterson, L. C. (2017). Thallium-isotopic compositions of euxinic sediments as a proxy for global manganese-oxide burial. *Geochimica et Cosmochimica Acta*, *213*, 291–307. https://doi.org/10.1016/j.gca.2017.06.041

Peacock, C. L., & Moon, E. M. (2012). Oxidative scavenging of thallium by birnessite: Explanation for thallium enrichment and stable isotope fractionation in marine ferromanganese precipitates. *Geochimica et Cosmochimica Acta*, *84*, 297–313. https://doi.org/10.1016/j.gca.2012.01.036

Pearce, C. R., Cohen, A. S., Coe, A. L., & Burton, K. W. (2008). Molybdenum isotope evidence for global ocean anoxia coupled with perturbations to the carbon cycle during the early Jurassic. *Geology*, *36*(3), 231–234. https://doi.org/10.1130/G24446A.1

Percival, L. M. E., Davies, J. H. F. L., Schaltegger, U., De Vleeschouwer, D., Da Silva, A. C., & Föllmi, K. B. (2018). Precisely dating the Frasnian – Famennian boundary: implications for the cause of the Late Devonian mass extinction. *Nature*, *8*(9578), 1–10. https://doi.org/10.1038/s41598-018-27847-7

Poulson, R. L., Siebert, C., McManus, J., & Berelson, W. M. (2006). Authigenic molybdenum isotope signatures in marine sediments. *Geology*, *34*(8), 617–620. https://doi.org/10.1130/G22485.1

Racki, G. (2005). Toward understanding Late Devonian global events: few answers, many questions. In D. J. Over, J. R. Morrow, & P. B. Wignall (Eds.), *Developments in Palaeontology and Stratigraphy* (Vol. 20, Issue C, pp. 5–36). Elsevier B.V. https://doi.org/10.1016/S0920-5446(05)80002-0

Rehkämper, M., Frank, M., Hein, J. R., Porcelli, D., Halliday, A. N., Ingri, J., & Liebetrau, V. (2002). Thallium isotope variations in seawater and hydrogenetic, diagenetic, and hydrothermal ferromanganese deposits. *Earth and Planetary Science Letters*, *197*(1–2), 65–81.

https://doi.org/10.1016/S0012-821X(02)00462-4

Rehkämper, M., & Halliday, A. N. (1999). The precise measurement of Tl isotopic compositions by MC-ICPMS: Application to the analysis of geological materials and meteorites. *Geochimica et Cosmochimica Acta*, *63*(6), 935–944. https://doi.org/10.1016/S0016-7037(98)00312-3

Rehkämper, M., & Nielsen, S. G. (2004). The mass balance of dissolved thallium in the oceans. *Marine Chemistry*, *85*(3–4), 125–139. https://doi.org/10.1016/j.marchem.2003.09.006

Rimmer, S. M., Thompson, J. A., Goodnight, S. A., & Robl, T. L. (2004). Multiple controls on the preservation of organic matter in Devonian–Mississippian marine black shales: geochemical and petrographic evidence. *Palaeogeography, Palaeoclimatology, Palaeoecology*, *215*(1–2), 125–154. https://doi.org/10.1016/j.palaeo.2004.09.001

Rolison, J. M., Stirling, C. H., Middag, R., & Rijkenberg, M. J. A. (2017). Uranium stable isotope fractionation in the Black Sea: Modern calibration of the 238U/235U paleo-redox proxy. *Geochimica et Cosmochimica Acta*, *203*, 69–88. https://doi.org/10.1016/j.gca.2016.12.014

Rudnick, R. L., & Gao, S. (2013). Composition of the Continental Crust. In *Treatise on Geochemistry: Second Edition* (2nd ed., Vol. 4, pp. 1–51). Elsevier Ltd. https://doi.org/10.1016/B978-0-08-095975-7.00301-6

Russell, D. J. (1993). Stratigraphy of the Kettle Point Formation (Upper Devonian of southwestern Ontario, Canada) - implications for depositional setting and resource potential. In *US Geological Survey Bulletin* (Vol. 1909, pp. E1–E11).

Schauble, E. A. (2006). Equilibrium uranium isotope fractionation by nuclear volume and mass-dependent processes. *AGU Fall Meeting Abstracts*, 570.

Schauble, E. A. (2007). Role of nuclear volume in driving equilibrium stable isotope fractionation of mercury, thallium, and other very heavy elements. *Geochimica et Cosmochimica Acta*, *71*(9), 2170–2189. https://doi.org/10.1016/j.gca.2007.02.004

Schieber, J. (2011). Marcasite in black shales - A mineral proxy for oxygenated bottom waters and intermittent oxidation of carbonaceous muds. *Journal of Sedimentary Research*, *81*(7), 447–458. https://doi.org/10.2110/jsr.2011.41

Scholz, F., Baum, M., Siebert, C., Eroglu, S., Dale, A. W., Naumann, M., & Sommer, S. (2018). Sedimentary molybdenum cycling in the aftermath of seawater inflow to the intermittently euxinic Gotland Deep, Central Baltic Sea. *Chemical Geology*, *491*(February), 27–38. https://doi.org/10.1016/j.chemgeo.2018.04.031

Scholz, F., McManus, J., & Sommer, S. (2013). The manganese and iron shuttle in a modern euxinic basin and implications for molybdenum cycling at euxinic ocean margins. *Chemical Geology*, *355*, 56–68. https://doi.org/10.1016/j.chemgeo.2013.07.006

Scholz, F., Siebert, C., Dale, A. W., & Frank, M. (2017). Intense molybdenum accumulation in sediments underneath a nitrogenous water column and implications for the reconstruction of paleo-redox conditions based on molybdenum isotopes. *Geochimica et Cosmochimica Acta*, *213*, 400–417. https://doi.org/10.1016/j.gca.2017.06.048

Scotese, C. R. (2021). An atlas of phanerozoic paleogeographic maps: The seas come in and the seas go out. *Annual Review of Earth and Planetary Sciences*, *49*, 679–728. https://doi.org/10.1146/annurev-earth-081320-064052

Scott, C., & Lyons, T. W. (2012). Contrasting molybdenum cycling and isotopic properties in euxinic versus non-euxinic sediments and sedimentary rocks: Refining the paleoproxies. *Chemical Geology*, *324–325*, 19–27. https://doi.org/10.1016/j.chemgeo.2012.05.012

Scott, C., Lyons, T. W., Bekker, A., Shen, Y., Poulton, S. W., Chu, X., & Anbar, A. D. (2008). Tracing the stepwise oxygenation of the Proterozoic ocean. *Nature*, *452*(7186), 456–459. https://doi.org/10.1038/nature06811

Siebert, C., Nägler, T. F., von Blanckenburg, F., & Kramers, J. D. (2003). Molybdenum isotope records as a potential new proxy for paleoceanography. *Earth and Planetary Science Letters*, *211*(1–2), 159–171. https://doi.org/10.1016/S0012-821X(03)00189-4

Sloss, L. L. (1963). Sequences in the Cratonic Interior of North America. *Geological Society Of America Bulletin*, *74*(2), 93–114. https://doi.org/10.1130/0016-7606(1963)74[93:SITCIO]2.0.CO;2

Song, Y., Gilleaudeau, G. J., Lyons, T. J., Jeffrey Over, D., Lyons, T. W., Anbar, A. D., & Xie, S. (2021). Biomarker Evidence of Algal-Microbial Community Changes Linked to Redox and Salinity Variation, Upper Devonian Chattanooga Shale (Tennessee, USA). *Bulletin of the Geological Society of America*, *133*(1), 409–424. https://doi.org/10.1130/B35543.1

Stylo, M., Neubert, N., Wang, Y., Monga, N., Romaniello, S. J., & Weyer, S. (2015). Uranium isotopes fingerprint biotic reduction. *Proceedings of the National Academy of Sciences of the United States of America*, *112*(18), 5619–5624. https://doi.org/10.1073/pnas.1421841112

Them, T. R., Gill, B. C., Caruthers, A. H., Gerhardt, A. M., Gröcke, D. R., Lyons, T. W., Marroquín, S. M., Nielsen, S. G., João, P. T. A., & Owens, J. D. (2018). Thallium isotopes reveal protracted anoxia during the Toarcian (Early Jurassic) associated with volcanism, carbon burial, and mass

extinction. *Proceedings of the National Academy of Sciences of the United States of America*, *115*(26), 6596–6601. https://doi.org/10.1073/pnas.1803478115

Tissot, F. L. H., Dauphas, N., Reinhard, C. T., Lyons, T. W., Asael, D., & Rouxel, O. (2013). Mo and U Geochemistry and Isotopes. In V. A. Melezhik, A. R. Prave, A. E. Fallick, E. J. Hanski, A. Lepland, L. R. Kump, & H. Strauss (Eds.), *Reading the Archive of Earth's Oxygenation* (Vol. 3, pp. 1500–1506). Springer-Verlag. https://doi.org/10.1007/978-3-642-29670-3

Tossell, J. A. (2005). Calculating the partitioning of the isotopes of Mo between oxidic and sulfidic species in aqueous solution. *Geochimica et Cosmochimica Acta*, *69*(12), 2981–2993. https://doi.org/10.1016/j.gca.2005.01.016

Tribovillard, N., Algeo, T. J., Baudin, F., & Riboulleau, A. (2012). Analysis of marine environmental conditions based on molybdenum-uranium covariation-Applications to Mesozoic paleoceanography. *Chemical Geology*, *324–325*, 46–58. https://doi.org/10.1016/j.chemgeo.2011.09.009

Tribovillard, N., Algeo, T. J., Lyons, T. W., & Riboulleau, A. (2006). Trace metals as paleoredox and paleoproductivity proxies: An update. *Chemical Geology*, *232*(1–2), 12–32. https://doi.org/10.1016/j.chemgeo.2006.02.012

Tribovillard, N., Riboulleau, A., Lyons, T. W., & Baudin, F. (2004). Enhanced trapping of molybdenum by sulfurized marine organic matter of marine origin in Mesozoic limestones and shales. *Chemical Geology*, *213*(4), 385–401. https://doi.org/10.1016/j.chemgeo.2004.08.011

Tuite, M. L., Williford, K. H., & Macko, S. A. (2019). From greenhouse to icehouse: Nitrogen biogeochemistry of an epeiric sea in the context of the oxygenation of the Late Devonian atmosphere/ocean system. *Palaeogeography, Palaeoclimatology, Palaeoecology*, *531*(February 2018), 1–13. https://doi.org/10.1016/j.palaeo.2019.05.026

Vorlicek, T. P., Kahn, M. D., Kasuya, Y., & Helz, G. R. (2004). Capture of molybdenum in pyrite-forming sediments: Role of ligand-induced reduction by polysulfides. *Geochimica et Cosmochimica Acta*, *68*(3), 547–556. https://doi.org/10.1016/S0016-7037(00)00444-7

Waite, T. D., Davis, J. A., Payne, T. E., Waychunas, G. A., & Xu, N. (1994). Uranium(VI) adsorption to ferrihydrite: Application of a surface complexation. *Geochimica et Cosmochimica Acta*, *58*(24), 5465–5478.

Wang, J. (2016). *Uranium and Molybdenum Isotope Constraints on Ocean Redox Conditions During Deposition of the Upper Devonian Kettle Point Formation, Ontario*. University of Waterloo.

Wang, Y., Lu, W., Costa, K. M., & Nielsen, S. G. (2022). Beyond anoxia: Exploring sedimentary thallium isotopes in paleo-redox reconstructions from a new core top collection. *Geochimica et Cosmochimica Acta*, *333*, 347–361. https://doi.org/10.1016/j.gca.2022.07.022

Wasylenki, L. E., Rolfe, B. A., Weeks, C. L., Spiro, T. G., & Anbar, A. D. (2008). Experimental investigation of the effects of temperature and ionic strength on Mo isotope fractionation during adsorption to manganese oxides. *Geochimica et Cosmochimica Acta*, *72*(24), 5997–6005. https://doi.org/10.1016/j.gca.2008.08.027

Wasylenki, L. E., Weeks, C. L., Bargar, J. R., Spiro, T. G., Hein, J. R., & Anbar, A. D. (2011). The molecular mechanism of Mo isotope fractionation during adsorption to birnessite. *Geochimica et Cosmochimica Acta*, *75*(17), 5019–5031. https://doi.org/10.1016/j.gca.2011.06.020

Watanabe, Y., & Takahashi, Y. (2015). An Experimental Study of Stabilization of Trivalent Thallium by Natural Organic Matter. *Chemistry Letters*, *44*(10), 1356–1358. https://doi.org/10.1246/cl.150551

Wei, W., & Algeo, T. J. (2020). Elemental proxies for paleosalinity analysis of ancient shales and mudrocks. *Geochimica et Cosmochimica Acta*, *287*, 341–366. https://doi.org/10.1016/j.gca.2019.06.034

Weyer, S., Anbar, A. D., Gerdes, A., Gordon, G. W., Algeo, T. J., & Boyle, E. A. (2008). Natural fractionation of 238U/235U. *Geochimica et Cosmochimica Acta*, *72*(2), 345–359. https://doi.org/10.1016/j.gca.2007.11.012

White, D. A., Elrick, M., Romaniello, S. J., & Zhang, F. (2018). Global seawater redox trends during the Late Devonian mass extinction detected using U isotopes of marine limestones. *Earth and Planetary Science Letters*, *503*, 68–77. https://doi.org/10.1016/j.epsl.2018.09.020

White, M. (2013). Unconventional Isotopes and Approaches. In *Isotope Geochemistry* (pp. 327–384).

Wick, S., Baeyens, B., Marques Fernandes, M., Göttlicher, J., Fischer, M., Pfenninger, N., Plötze, M., & Voegelin, A. (2020). Thallium sorption and speciation in soils: Role of micaceous clay minerals and manganese oxides. *Geochimica et Cosmochimica Acta*, *288*, 83–100. https://doi.org/10.1016/j.gca.2020.07.037

Wick, S., Baeyens, B., Marques Fernandes, M., & Voegelin, A. (2018). Thallium Adsorption onto Illite. *Environmental Science and Technology*, *52*(2), 571–580. https://doi.org/10.1021/acs.est.7b04485

Wick, S., Peña, J., & Voegelin, A. (2019). Thallium Sorption onto Manganese Oxides. *Environmental Science and Technology*, *53*, 13168−13178. https://doi.org/10.1021/acs.est.9b04454

Zheng, Y., Anderson, R. F., Van Geen, A., & Fleisher, M. Q. (2002a). Preservation of particulate non-

lithogenic uranium in marine sediments. *Geochimica et Cosmochimica Acta*, *66*(17), 3085–3092. https://doi.org/10.1016/S0016-7037(01)00632-9

Zheng, Y., Anderson, R. F., Van Geen, A., & Fleisher, M. Q. (2002b). Remobilization of authigenic uranium in marine sediments by bioturbation. *Geochimica et Cosmochimica Acta*, *66*(10), 1759–1772. https://doi.org/10.1016/s0016-7037(01)00886-9

Zheng, Y., Anderson, R. F., Van Geen, A., & Kuwabara, J. (2000). Authigenic molybdenum formation in marine sediments: A link to pore water sulfide in the Santa Barbara Basin. *Geochimica et Cosmochimica Acta*, *64*(24), 4165–4178. https://doi.org/10.1016/S0016-7037(00)00495-6

Appendix A: Leached Major and Trace Element Contents

Unit	Sample	Depth	Tl	Mo	U	Re	V	Al	Fe	K	Mg	Mn	Na	P
		m	µg/g	µg/g	µg/g	ng/g	µg/g	wt%	wt%	wt%	wt%	µg/g	wt%	µg/g
4	KPZ-1	28.0	6.8	249.8	29.7	187.9	150.7	0.73	2.1	0.3	0.4	172	0.1	0.10
	KPZ-2	28.7	9.0	332.4	36.1	214.4	214.0	0.75	2.7	0.3	0.5	212	0.1	0.10
	KPZ-3	29.4	7.8	334.2	43.0	258	266.2	0.74	2.1	0.3	0.3	84	0.1	0.10
	KPZ-4	30.6	5.7	217.8	35.2	221.5	173.3	0.72	4.6	0.3	0.3	74	0.2	0.09
	KPZ-5	31.4	9.2	168.8	28.5	230.4	192.9	0.72	2.9	0.3	0.3	86	0.2	0.08
	KPZ-6	32.9	3.7	36.5	7.8	153.8	122.3	0.82	2.2	0.4	0.4	122	0.2	0.06
	KPZ-7	34.4	5.9	100.2	19.3	256.8	246.9	0.71	1.6	0.3	0.3	81	0.2	0.06
	KPW6	36.0	8.1	69.7	17.2	158.9	172.2	0.78	2.3	0.4	0.2	77	0.2	0.06
	KPW4	37.5	7.6	115.2	20.2	150.4	108.8	0.75	2.2	0.3	0.2	80	0.2	0.09
	KPW5	39.5	14.3	161.8	22.1	331.3	137.0	0.64	2.9	0.3	0.3	89	0.2	0.09
	KPW3	41.2	7.0	75.0	14.3	124.6	110.6	0.80	2.0	0.3	0.2	82	0.2	0.06
	KPW2	42.9	4.9	46.6	8.5	84.7	87.9	0.90	2.3	0.4	0.2	78	0.2	0.05
	KPW1	44.1	3.7	37.8	5.7	73.9	76.3	0.82	2.4	0.4	0.2	81	0.2	0.04
	KPR2	46.4	4.2	65.4	10.5	103.9	146.5	0.85	1.9	0.4	0.3	101	0.2	0.05
	KPR6	48.6	5.0	85.2	18.5	121.0	104.3	0.74	1.9	0.3	0.2	78	0.2	0.07
	KPR8	51.4	4.2	69.8	15.2	117.9	154.6	0.73	1.5	0.3	0.2	131	0.2	0.06
	KPR11	53.5	4.3	85.7	20.4	97.7	132.5	0.91	1.8	0.4	0.3	86	0.2	0.06
	KPR14	56.8	3.2	66.6	16.7	72.8	73.3	0.79	1.6	0.4	0.3	87	0.2	0.06
	KPR17	58.8	4.3	112.6	28.6	65.5	42.8	0.94	2.4	0.4	0.3	105	0.2	0.09
	KPP11	61.6	3.2	73.3	18.0	60.7	34.3	0.85	2.1	0.4	0.3	122	0.2	0.07
3	KPP4	73.9	2.7	62.1	15.2	43.0	34.0	1.01	2.0	0.4	0.4	145	0.2	0.08
	KPP3	76.6	1.7	31.4	3.4	26.6	22.9	0.99	2.6	0.4	0.3	95	0.2	0.04
	KP20	87.7	2.3	48.2	9.9	27.0	21.7	1.04	2.6	0.5	0.4	147	0.2	0.05
2	KP18	92.0	2.4	46.2	11.3	33.0	20.4	1.12	3.1	0.7	0.5	233	0.3	0.07
	KP15	98.1	2.1	41.2	9.6	31.5	17.0	0.70	2.2	0.3	0.2	98	0.2	0.06
	KP12	105.1	1.3	77.5	13.1	28.9	10.3	0.43	2.9	0.3	0.2	95	0.2	0.05
	KP9	108.3	0.72	51.8	8.9	18.0	9.8	0.44	2.9	0.3	0.2	88	0.2	0.05
	KP8	110.1	1.0	61.1	11.2	27.1	11.4	0.50	3.1	0.3	0.2	75	0.2	0.07
	KP7	114.2	1.1	48.7	7.0	10.4	9.4	0.42	2.7	0.3	0.2	99	0.2	0.05
	KP6	118.2	1.8	96.2	21.4	34.3	19.9	0.55	4.1	0.2	0.2	112	0.1	0.10
1	KP5	120.2	3.6	100.0	17.5	120.2	27.5	0.67	4.5	0.3	0.3	134	0.1	0.15
	KP4	123.0	1.6	42.6	18.2	29.6	24.9	0.85	5.1	0.3	0.4	178	0.1	0.09
	KP3	126.1	3.5	100.3	15.6	100.4	23.6	0.97	3.4	0.3	0.3	119	0.1	0.09
	KP2	128.6	1.4	79.7	13.5	47.9	13.5	0.67	3.2	0.3	0.3	130	0.1	0.08
	KP11	130.9	1.4	87.5	10.9	36.8	15.4	0.81	3.4	0.3	0.4	144	0.2	0.07
	KP1	135.3	4.3	100.7	22.4	175.9	71.4	0.68	2.6	0.2	0.3	95	0.1	0.15

Appendix B: Tl - Mo - U Isotope Ratios

Unit	Sample	Depth	ε205Tl			δ98Mo*			δ238U*		
		m	ε units	2SD	n	‰	2SD	n	‰	2SD	n
4	KPZ-1	28.0	-6.3	0.4	2	0.82	0.11	3	0.60	0.08	3
	KPZ-2	28.7	-6.1	0.5	4	0.98	0.11	3	0.44	0.08	3
	KPZ-3	29.4	-6.7	0.2	2	0.95	0.11	3	0.49	0.08	3
	KPZ-4	30.6	-6.0	0.1	4	0.88	0.11	3	0.44	0.08	3
	KPZ-5	31.4	-6.3	0.3	3	0.95	0.11	3	0.42	0.10	3
	KPZ-6	32.9	-6.5	0.1	2	0.77	0.11	3	0.28	0.08	3
	KPZ-7	34.4	-6.3	0.2	2	0.71	0.11	3	0.60	0.08	3
	KPW6	36.0	-6.3	0.2	2	0.68	0.11	3	0.52	0.08	3
	KPW4	37.5	-5.9	0.4	2	0.76	0.11	3	0.46	0.08	3
	KPW5	39.5	-7.2	0.6	2	0.78	0.11	3	0.44	0.08	3
	KPW3	41.2	-5.7	0.0	2	0.69	0.11	3	0.51	0.08	3
	KPW2	42.9	-5.5	0.2	2	0.72	0.11	3	0.45	0.08	3
	KPW1	44.1	-5.5	0.5	3	0.69	0.11	3	0.49	0.08	3
	KPR2	46.4	-5.7	0.1	2	0.55	0.11	3	0.46	0.14	3
	KPR6	48.6	-5.4	0.3	2	0.88	0.11	3	0.41	0.08	3
	KPR8	51.4	-5.4	0.5	2	0.77	0.11	3	0.41	0.11	3
	KPR11	53.5	-6.1	0.2	2	0.79	0.11	3	0.37	0.10	3
	KPR14	56.8	-4.9	0.1	2	0.87	0.11	3	0.25	0.08	3
	KPR17	58.8	-3.8	0.4	2	1.3	0.11	3	0.15	0.08	3
	KPP11	61.6	-3.9	0.3	3	1.3	0.11	3	0.16	0.11	3
3	KPP4	73.9	-4.5	0.0	2	1.1	0.11	3	0.26	0.08	3
	KPP3	76.6	-3.6	0.1	2	0.78	0.11	3	0.22	0.08	3
	KP20	87.7	-2.7	0.3	4	1.1	0.11	3	0.09	0.08	3
2	KP18	92.0	-2.7	0,17	3	1.2	0.11	3	-0.02	0.08	3
	KP15	98.1	-2.1	0.5	4	0.97	0.11	3	0.06	0.08	3
	KP12	105.1	-2.0	0.7	2	1.3	0.11	3	-0.05	0.10	3
	KP9	108.3	-3.3	0.4	2	1.7	0.11	3	-0.10	0.08	3
	KP8	110.1	-3.1	0.5	4	1.5	0.11	3	-0.12	0.11	3
	KP7	114.2	-3.2	0.2	2	1.6	0.11	3	-0.13	0.08	3
	KP6	118.2	-3.0	0.2	3	1.7	0.1	3	-0.24	0.08	3
1	KP5	120.2	-2.2	0.4	2	1.3	0.11	3	-0.01	0.08	2
	KP4	123.0	-3.2	0.1	3	2.0	0.11	3	-0.29	0.08	3
	KP3	126.1	-2.2	0.2	2	1.2	0.11	3	0.00	0.08	3
	KP2	128.6	-2.4	0.3	3	1.7	0.11	3	-0.09	0.08	2
	KP11	130.9	-2.5	0.3	3	2.0	0.11	3	-0.08	0.08	3
	KP1	135.3	-4.7	0.3	3	0.98	0.11	3	0.31	0.08	3

*Published in Kendall et al. (2020)

Appendix C: Bulk Major and Trace Element Contents

Unit	Sample	Depth	Tl		Mo*		U*		Re		V*		Al*	Ba*		Fe*	K	Mg*	Mn		Na	P	Sr*	Ba*	Sr/Ba*	B*	Ga*	B/Ga*	TS*	TOC*	TS/TOC*	S_{pyrite}	$\delta^{13}C$*
		m	µg/g	EF	µg/g	EF	µg/g	EF	ng/g	EF	µg/g	EF	wt%	µg/g	EF	wt%	wt%	wt%	µg/g	EF	wt%	µg/g	µg/g	µg/g		µg/g	µg/g		wt%	wt%		wt%	‰
4	KPZ-1	28.0	9.3	9.5	358	300	43	15	226	1055	1198	11	8.8	215	0.32	3.6	3.0	0.4	227	0.27	0.076	0.10	126	215	0.58	104	20	5.2	1.7	13	0.13	1.4	-29.7
	KPZ-2	28.7	12	13	459	409	49	18	255	1263	1479	15	8.3	86	0.14	4.2	3.0	0.5	276	0.35	0.12	0.10	94	86	1.1	107	20	5.4	2.2	12	0.18	1.7	-29.7
	KPZ-3	29.4	10	12	473	463	57	23	279	1514	1912	21	7.6	239	0.41	3.3	2.9	0.3	130	0.18	0.14	0.10	114	239	0.48	106	18	6.1	1.8	16	0.12	1.5	-29.7
	KPZ-4	30.6	7.6	9.4	302	307	46	19	44	250	1327	15	7.3	120	0.21	5.6	2.8	0.3	109	0.16	0.16	0.089	64	120	0.53	103	18	5.7	5.1	12	0.42	4.1	-29.9
	KPZ-5	31.4	13	14	243	217	41	15	59	295	1715	17	8.3	371	0.59	4.1	3.2	0.3	120	0.15	0.18	0.083	74	371	0.20	104	18	5.8	2.8	10	0.28	2.3	-29.6
	KPZ-6	32.9	5.0	5.6	59	53	15	5.7	190	958	945	9.7	8.2	394	0.63	3.5	3.4	0.4	163	0.21	0.19	0.063	67	394	0.17	123	19	6.5	1.7	8.8	0.19	1.3	-29.7
	KPZ-7	34.4	7.3	9.4	168	176	31	13	288	1680	1778	21	7.1	393	0.73	2.9	3.0	0.3	119	0.18	0.17	0.062	61	393	0.15	103	16	6.3	1.4	11	0.13	1.2	-29.8
	KPW6	36.0	9.5	11	101	98	27	11	97	524	1204	13	7.6	413	0.71	3.3	3.0	0.2	105	0.14	0.20	0.055	64	413	0.16	99	17	5.8	2.2	11	0.20	1.8	-29.8
	KPW4	37.5	9.8	11	167	147	32	11	135	657	897	9.0	8.4	491	0.76	3.4	3.1	0.2	116	0.14	0.20	0.086	78	491	0.16	110	19	5.6	3.4	8.8	0.39	1.7	-29.7
	KPW5	39.5	17	20	236	226	35	14	330	1755	1164	13	7.8	213	0.36	4.2	3.1	0.3	123	0.17	0.20	0.094	72	213	0.34	101	19	5.4	1.9	7.8	0.24	2.7	-29.9
	KPW3	41.2	8.8	8.8	119	97	26	8.7	99	449	872	8.0	9.1	502	0.72	3.5	3.4	0.2	125	0.14	0.18	0.061	69	502	0.14	109	21	5.2	1.8	6.9	0.26	1.5	-29.7
	KPW2	42.9	7.3	7.1	71	56	17	5.6	14	62	684	6.1	9.3	407	0.57	3.5	3.5	0.2	120	0.13	0.20	0.049	80	407	0.20	113	24	4.8	1.9	4.9	0.39	1.2	-29.7
	KPW1	44.1	5.2	4.8	61	46	13	4.1	11	48	682	5.9	9.8	323	0.43	3.6	3.5	0.2	114	0.12	0.21	0.042	79	323	0.24	128	24	5.4	2.0	4.1	0.48	1.3	-29.5
	KPR2	46.4	5.7	5.9	102	88	19	6.5	130	617	1071	10	8.6	439	0.66	3.0	3.3	0.3	138	0.17	0.20	0.049	74	439	0.17	118	21	5.7	1.5	6.4	0.23	1.2	-29.6
	KPR6	48.6	5.6	6.8	135	135	28	11	135	745	790	8.9	7.4	429	0.75	3.0	2.9	0.2	121	0.17	0.18	0.069	68	429	0.16	107	17	6.5	1.2	7.9	0.15	1.4	-29.5
	KPR8	51.4	4.6	5.7	111	113	25	10	141	792	1097	13	7.3	347	0.62	2.7	3.0	0.2	175	0.25	0.19	0.065	66	347	0.19	106	16	6.6	1.2	8.2	0.15	0.81	-29.3
	KPR11	53.5	4.1	5.2	124	126	31	13	98	553	761	8.8	7.3	488	0.88	2.8	3.1	0.3	128	0.19	0.18	0.063	64	488	0.13	125	19	6.7	1.4	8.5	0.16	1.2	-29.4
	KPR14	56.8	4.5	5.4	103	102	26	10	72	397	532	6.0	7.5	377	0.66	2.7	3.1	0.3	122	0.17	0.19	0.065	64	377	0.17	87	18	4.9	1.2	7.3	0.16	1.0	-29.1
	KPR17	58.8	5.3	5.8	158	142	37	13	73	365	314	3.2	8.3	402	0.64	3.5	3.4	0.3	145	0.18	0.20	0.088	68	402	0.17	118	20	5.8	1.9	8.5	0.22	1.7	-29.7
	KPP11	61.6	3.2	3.6	108	99	27	10	57	289	288	3.0	8.1	401	0.65	3.2	3.3	0.3	159	0.21	0.20	0.073	71	401	0.18	128	20	6.5	1.6	7.0	0.23	1.3	-29.8
3	KPP4	73.9	2.4	2.7	93	85	25	9.3	53	267	255	2.6	8.1	402	0.65	3.1	3.4	0.4	189	0.25	0.21	0.077	66	402	0.16	133	20	6.8	1.3	6.4	0.20	0.89	-30.1
	KPP3	76.6	2.9	2.8	48	37	9.3	2.9	8	32	238	2.1	9.6	162	0.22	3.8	3.8	0.3	149	0.16	0.20	0.043	81	162	0.50	151	26	5.9	2.0	3.1	0.64	1.1	-29.7
	KP20	87.7	3.3	3.6	75	67	18	6.6	39	194	181	1.8	8.3	344	0.54	3.8	3.7	0.4	191	0.24	0.21	0.046	80	344	0.23	119	20	6.1	1.9	5.8	0.33	1.4	-29.8
2	KP18	92.0	3.1	3.4	66	60	19	7.0	36	183	164	1.7	8.1	103	0.17	4.0	3.5	0.5	195	0.25	0.30	0.067	89	103	0.86	132	20	6.6	2.2	4.5	0.49	1.4	-30.1
	KP15	98.1	2.6	3.5	60	66	17	7.6	40	242	159	2.0	6.7	251	0.49	3.1	3.1	0.2	134	0.21	0.18	0.056	67	251	0.27	127	17	7.3	2.0	5.7	0.35	1.5	-30.0
	KP12	105.1	2.1	3.1	108	129	22	11	17	111	128	1.7	6.2	102	0.21	3.9	2.8	0.2	123	0.21	0.18	0.051	62	102	0.61	98	15	6.4	3.5	7.7	0.46	2.6	-30.1
	KP9	108.3	1.2	2.0	70	95	16	8.8	5	34	101	1.6	5.5	163	0.39	3.8	2.7	0.2	102	0.20	0.16	0.050	64	163	0.39	95	13	7.3	3.3	5.0	0.66	2.3	-29.8
	KP8	110.1	1.6	2.2	84	98	20	9.6	6	37	119	1.6	6.3	97	0.20	4.2	3.1	0.2	136	0.23	0.18	0.074	80	97	0.82	105	16	6.6	3.6	7.1	0.51	2.6	-29.9
	KP7	114.2	1.6	3.1	65	101	14	8.8	3	29	89	1.6	4.8	120	0.33	3.4	2.4	0.2	143	0.32	0.15	0.049	61	120	0.51	87	11	7.8	3.0	5.5	0.54	1.8	-30.0
	KP6	118.2	1.9	3.5	125	192	30	18	41	347	113	2.0	4.8	140	0.38	4.6	2.5	0.2	283	0.62	0.14	0.10	64	140	0.46	105	12	8.9	4.2	9.3	0.45	3.0	-30.5
1	KP5	120.2	4.4	6.2	133	156	27	13	57	370	167	2.2	6.3	178	0.37	5.0	3.2	0.3	175	0.29	0.12	0.15	83	178	0.47	111	16	6.9	4.8	9.9	0.48	4.0	-30.5
	KP4	123.0	2.1	2.8	59	65	26	12	30	183	139	1.8	6.7	60	0.12	6.2	3.0	0.4	205	0.32	0.11	0.095	79	60	1.32	129	17	7.7	6.0	12	0.49	5.0	-30.1
	KP3	126.1	4.8	6.1	134	138	27	11	47	267	163	1.9	7.2	100	0.18	4.0	3.3	0.3	164	0.24	0.13	0.091	86	100	0.87	124	19	6.5	2.9	8.2	0.35		-30.4
	KP2	128.6	2.6	3.5	115	125	26	11	23	138	125	1.5	6.8	91	0.18	4.2	3.2	0.3	164	0.25	0.11	0.084	68	91	0.75	114	16	7.1	3.2	13	0.24	2.8	-29.3
	KP11	130.9	2.0	2.4	111	111	20	8.3	16	91	136	1.5	7.4	265	0.47	4.0	3.7	0.4	168	0.24	0.16	0.075	72	265	0.27	134	18	7.6	3.0	7.2	0.42	2.4	-30.5
	KP1	135.3	5.9	7.2	152	153	38	15	157	883	548	6.3	7.3	147	0.26	3.5	3.4	0.3	126	0.18	0.12	0.15	78	147	0.53	172	20	8.8	2.3	14	0.16	2.4	-30.6

*Published in Kendall et al. (2020)